Nonlinear Dynamics of Water and Energy Balance in Land–Atmosphere Interaction

by

Kaye Lorraine Brubaker

B.A., Eastern Mennonite College (1979)
B.S.Civ.Eng., University of Maryland College Park (1989)
S.M., Massachusetts Institute of Technology (1991)

Submitted to the Department of Civil and Environmental Engineering
in partial fulfillment of the requirements for the degree of

Doctor of Philosophy

at the

MASSACHUSETTS INSTITUTE OF TECHNOLOGY

February 1995

Author .....
Department of Civil and Environmental Engineering
November 22, 1994

Certified by .....
Dara Entekhabi
Assistant Professor
Thesis Supervisor

Accepted by .....
Joseph M. Sussman
Chairman, Departmental Committee on Graduate Studies

Nonlinear Dynamics of Water and Energy Balance in Land–Atmosphere Interaction

by

Kaye Lorraine Brubaker

Submitted to the Department of Civil and Environmental Engineering
on November 22, 1994, in partial fulfillment of the
requirements for the degree of
Doctor of Philosophy

Abstract

The energy and moisture states in the soil and near–surface atmosphere evolve due to fluxes that are themselves a function of these states. The resultant nonlinear dynamical system has modes of variability and statistical signatures that depend on the full coupling of all components of heat and moisture balance.

A conceptual land–atmosphere model — consisting of a 1–D (in the vertical), 4–state balance for a soil layer and a turbulently–mixed atmospheric boundary layer — is subjected to stochastic forcing. The statistics of the moisture and energy states are computed; the covariability structure evolves through the state-dependent turbulent and radiative fluxes in the land–atmosphere system and is not prescribed *a priori*. The mathematical construct is exploited to explore several land–atmosphere interaction processes and to identify and quantify their influence on regional hydroclimate. Because the soil moisture and temperature are negatively correlated (dry-warm or cool-moist), physical mechanisms that tend to restore each state individually (soil-moisture control of evaporation and temperature dependence of saturation specific humidity) act as anomaly-enhancing (positive) feedback mechanisms for the other state. Dry anomalies are found to persist longer than moist anomalies, when evaporation efficiency is formulated to switch between soil and atmospheric control. *Two–way* interaction between the land and atmosphere is seen to be critical in establishing the memory and covariability of the moisture and temperature states of the soil.

Although usually triggered by large-scale circulation anomalies (decreased precipitation), dry soil anomalies may persist and intensify due to local land–atmosphere interactions. These interactions may, in turn, form feedback mechanisms that reinforce the large-scale anomaly. Thus, the explorations with the 1–D model are relevant to the persistence of hydrologic anomalies on both the local and the larger scale.

Thesis Supervisor: Dara Entekhabi
Title: Assistant Professor

Acknowledgments

The nonlinear dynamical partnership of student and professor continually evolves in response to its linked internal states and external perturbations. I am deeply grateful to my advisor, Dara Entekhabi, for his patience (and even his impatience, when necessary!) in helping me to find my way into the "feasible region" of producing this thesis. By his example and in conversation, Dara has taught me about scholarship, organization, and love of learning; and I believe it's safe to say we have both learned a great deal about interaction and feedbacks.

I am grateful to the National Science Foundation for its support through a Graduate Fellowship and Grant EAR–9296059.

I thank the members of my thesis committee — Rafael Bras, Peter Eagleson, Ignacio Rodriguez–Iturbe, and Richard Rosen — for their combination of rigor, wisdom, and caring; for their contagious enthusiasm about hydrology, climate, and stochastic modeling; for their friendly faces in the audience at AGU; and for risking New England weather and hotel fire scares to attend my committee meetings.

Many others have contributed to this endeavor. Richard McCuen, who first suggested graduate study at MIT, has generously and tirelessly provided encouragement and advice. Michael Celia, Dennis McLaughlin, and my student colleagues-to-be introduced me to the joy of life at the 'Tute (in the Lab and on the softball field) during my Summer Undergraduate Research Fellowship at MIT in 1988. Andrea Rinaldo gave me words of encouragement just when I needed them most.

I extend my heartfelt appreciation to my many communities who have provided support, both personal and technical ...

— The faculty, staff and students of Parsons Lab, especially Patricia Dixon (the heart and soul of Course I), for a pleasant setting in which to learn and grow;

— The Entekhabi/Eagleson Research Group (Eli Ateljevich, Gavin Gong, Kevin Johnson, Rene Kim, Marybeth Long, Rob Martello, Hajime Nakamura, Guido Salvucci, Russell Scott, Jennifer Wynn; "may [the] tribe increase!") for finding energy (if not always unity!) in diversity, and for being a fun, inspiring team;

— My "Grad Group" (Britt Holmen, Trine Jensen, Jenny Lee, Glenn Moglen, Lisa Moore,) for interdisciplinary friendship, support, and technology transfer;

— The Athena on-line consultant (olc) service, especially wchuang@tigana.mit.edu, for service above and beyond the call of duty;

— The Mennonite Congregation of Boston, the MennoLink electronic mailing list, the misc.kids newsgroup, R. Balser, T. Laage, and A. Van Niel, for helping me maintain equilibrium in the coupled mind/body/spirit system;

— My family — Brubakers, Conrads, Korineks, Swartzes and Calvert — for their love and understanding; Ursula Mangoubi and her family for their loving care of Simon and their friendship;

... And most of all, my husband David Conrad (restoring force *par excellence*) without whom this would never have been possible, and our son Simon (diffusion personified), who has made the last two years a little more complicated, but a *lot* more wonderful.

A portion of this material is based upon work supported by a National Science Foundation Graduate Fellowship. Any opinions, findings, conclusions or recommendations expressed herein are those of the author and do not reflect the views of the National Science Foundation.

To the memory of my mother,
Emma Shetler Brubaker (1926–1991),
my teacher at the beginning
and at the end.

Contents

List of Figures

List of Tables

Chapter 1

Introduction

A particular feature of continental climates is that hydrologic anomalies, whether moist or dry, tend to persist and intensify. This behavior is due to a complex set of interactions among the atmosphere, oceans, and continents, on both the regional and global scales (McNab and Karl 1989, Oglesby and Erickson 1989, Diaz 1983). Understanding these interactions and the time scales on which they operate has great practical consequences, including the development of predictive measures for drought or flood risk, and the onset and termination of anomalous conditions.

As the world faces the challenges of burgeoning population and global climate change, the socioeconomic and environmental consequences of extreme events, such as droughts, compellingly motivate investigation into the physical causes and statistical properties of these extreme events. Droughts are characterized by persistence and intensification, often with sudden transitions into or out of anomalously dry conditions (Diaz 1983). In most cases, the historical record is not long enough to develop a reliable drought climatology for a given region. Furthermore, in the face of possible large-scale climate change, it is desirable to gain a physical understanding of drought dynamics and a physical basis for drought forecasting, since past records cannot provide information on drought probability in a changed climate.

Various techniques of time-series modeling — such as Markov chain (e.g., Şen 1990) and theory of runs (e.g., Moyé et al. 1988) — have been applied in hopes of making useful climate forecasts. Such statistical models require strong assumptions concerning the underlying probability distribution and serial dependence of climatic variables; a model that is free of such assumptions would be preferable. The statistical signature of droughts results from complex interactions and feedbacks in the climate system; therefore, a statistical-dynamical approach should be more fruitful than a purely statistical analysis. Such an approach is based on a mathematical model that

captures the essential interaction and feedback mechanisms in the land-atmosphere system.

The land surface is the interface between the traditional domain of hydrologists and that of meteorologists. Each domain is a complex, nonlinear system; in the past, each group has tended to treat the other's domain as the fixed boundary conditions or the external forcing to its own. In reality, because the land and atmosphere interact, the system (from either point of view) alters its own boundary conditions or forcing. The study of the fully-coupled land-atmosphere system is fairly recent; Nicholson (1988) gives an interdisciplinary review, and Entekhabi (1994) describes advances since 1989. This introductory Chapter presents the issues of land–atmosphere interaction and gives a context for this thesis within the broad range of recent investigations. The remainder of the thesis describes an abstract, conceptual model that has been developed to study the coupled exchanges of water and energy at the land surface, and to investigate their role in regional-scale climatic variability.

1.1 Land–Atmosphere Interaction

The land and the atmosphere are linked by exchanges of mass, energy, and momentum. The moisture and temperature states of the land are major factors in regulating these exchanges, particularly the coupled transfers of energy and water mass.

With respect to the exchange of water mass, soil moisture controls the partitioning of precipitation into infiltration and runoff. The soil serves as a reservoir for the storage of liquid water and the slow release of water vapor into the atmosphere. Water that evaporates from the land may condense and fall again as precipitation into the same land region, constituting an internal recycling mechanism (Brubaker et al. 1993, Entekhabi et al. 1992, Rodriguez-Iturbe et al. 1991a,b). As for the energy exchange, when soil water is available, excess energy can be dissipated by latent heat flux (evaporation). When the soil is dry, the energy budget must be balanced through the thermal radiation and sensible heat fluxes, which are less efficient mechanisms, in the sense that they require elevated temperatures to provide an equivalent expenditure of energy. Thus, the heat and moisture state of the soil controls the partitioning of incident energy into outgoing longwave radiation and turbulent fluxes. The soil moisture and temperature determine the Bowen ratio (the ratio of sensible to latent heat flux). Moister soil has a lower surface albedo (resulting in greater absorption of solar radiation) and a higher heat capacity (allowing a smaller change in temperature for a given amount of absorbed energy), thus greater thermal inertia.

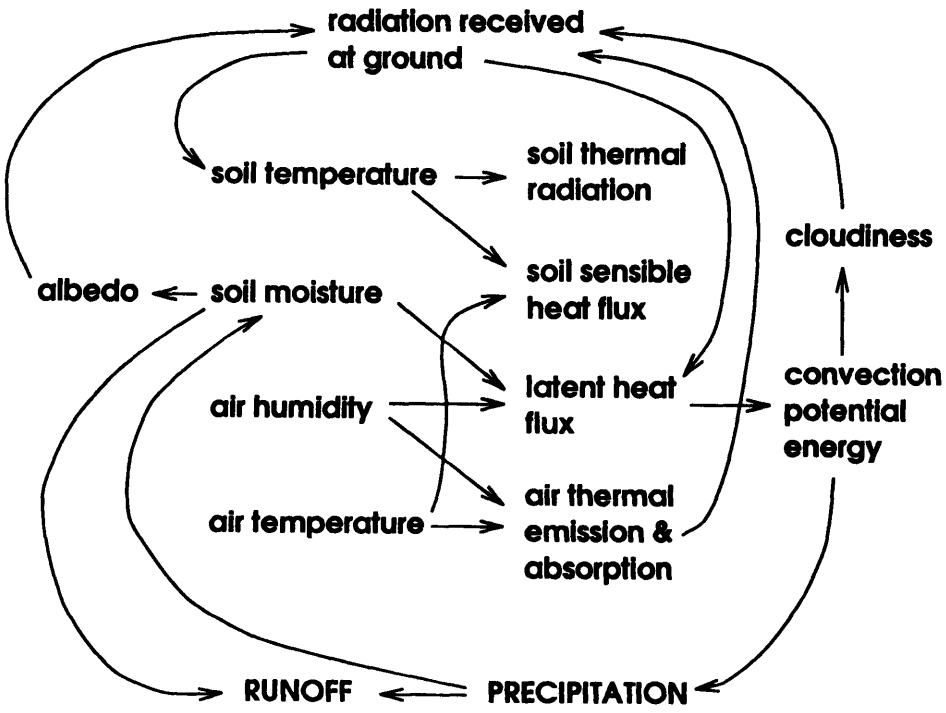

Figure 1-1: Conceptual diagram of the pathways through which soil temperature, soil moisture, near-surface air humidity, and near-surface air temperature mutually influence one another.

The heat and moisture states of the land and the atmosphere are intertwined, and water — with its high heat capacity and latent heat of phase change — is the major actor. Figure 1-1 is a conceptualization of the interconnections between these system states. The fluxes of water and energy from the land surface alter the water vapor and temperature profiles in the atmosphere, with consequences for atmospheric downward and upward longwave radiation. Clouds, formed by the condensation of atmospheric water vapor, reflect shortwave radiation and act, in a significant way, as gray-body emittors in the longwave. These combined factors affect the net radiation received at the land surface. The inputs of water vapor and sensible heat at the bottom of the air column provide energy for convection, enhancing the formation of clouds and precipitation.

1.1.1 Anomalies and feedbacks

Numerous feedback mechanisms are inherent in this coupled system. A positive feedback occurs when the system responds to a perturbation in such a way that the perturbation is amplified. In a negative feedback, the system responds by damping

or counteracting the perturbation.

The initiation or termination of a drought condition may depend on large-scale (global or hemispheric) or remote causes, such as persistent circulation patterns or teleconnections to sea-surface temperature anomalies (Namias 1983, McNab and Karl 1989). However, local positive feedbacks in the land-atmosphere system are believed to contribute to the observed persistence and intensification of droughts. The precipitation recycling mechanism is a positive feedback, in that rainfall moistens the soil and provides more water for evaporation, which in turn enhances the supply of water mass for precipitation. The atmospheric demand for evaporation (potential evaporation) depends on the temperature and humidity of the near-surface air and is thus dependent on the evaporation that has already occurred within the region (Bouchet 1963). An increase in albedo due to drying of the soil or removal of vegetation contributes to a net radiative heat loss, which enhances sinking motion and further inhibits precipitation, leading to further drying (Charney 1975). Synoptic observations over the United States (Namias 1988) indicate that large-scale soil moisture deficit may inhibit precipitation because the elevated surface temperature deepens the adiabatically-mixed air layer and intensifies the mid-continental high-pressure ridge.

1.2 Review of the Literature

As in all scientific endeavors, research in land–atmosphere interaction advances through simultaneous field observation, laboratory experiments, and analysis. Observations enlighten theory, which in turn, provides speculation and hypotheses that must be tested by observation. The diverse spatial scales of the Earth's hydrologic cycle and climate system provide a challenge for observation. How do point processes — which may or may not be well understood in themselves — integrate to large-scale responses, what large-scale parameters are important, and how might they be estimated? Recent large-scale field experiments such as HAPEX[1] in France and Niger, and FIFE[2] in the United States constitute intensive multi-scale observational efforts to address such questions. The development of technology for remote sensing of the Earth's surface and atmosphere, together with new tools to interpret remotely-sensed data, provides a wealth of new observations. In conjunction with the data-collecting effort, theory and analysis must continue to pose useful questions to organize and interpret

[1] Hydrologic Atmospheric Pilot Experiment

[2] First ISLSCP (International Satellite Land Surface Climatology Project) Field Experiment

the data.

To place this thesis in context, the following overview focuses on modeling studies of the climatic effects of the coupled water and energy exchanges between the soil and the near–surface atmosphere, or planetary boundary layer (PBL). Because research in this area is heavily dependent upon experiments with numerical models — themselves undergoing development — the distinction between theory and laboratory experiment becomes blurred; the results of a modeling study may tell us something about the Earth or about the need to improve the model, usually both. Indeed, with numerical models that incorporate observations through 4-D data assimilation (see, e.g., National Research Council 1991), it becomes difficult to distinguish modeling from observation. Therefore, the categories mentioned here lie along something of a continuous spectrum between pure observation and pure theory.

1.2.1 Modeling studies

Investigations in this topic are mostly based on the use of numerical models of the atmosphere that integrate the atmospheric primitive equations (equations of state, conservation of energy, mass, and momentum) and parameterize the physics associated with subgrid processes (hydrology, radiation, convection, etc.) on three-dimensional global or regional domains. The atmospheric models may be considered to be adequate numerical laboratories for larger-scale processes, conditional on the reliability of their representation of physical processes.

General Circulation Models

Studies with General Circulation Models (GCMs) show that the presence of an interactive soil moisture reservoir adds memory to the near-surface atmosphere (Delworth and Manabe 1988, 1989). Shukla and Mintz (1982) and Yeh et al. (1984) demonstrate the important role of land-surface evaporation in the global climate. One of the earliest such studies was Charney et al. (1977), which lent support to Charney's (1975) hypothesis on Sahel drought. According to that hypothesis, an increase in albedo due to drying of the soil or removal of vegetation contributes to a net radiative heat loss, which enhances sinking motion and further inhibits precipitation, leading to further drying. Walker and Rowntree (1977), Rind (1982), Rowntree and Bolton (1983), Oglesby and Erickson (1989), and Serafini (1990) describe experiments with several different GCMs, focusing on various aspects of continental climates. Recently, Meehl (1994) has used a GCM to investigate the role of land–atmosphere feedbacks in the

Indian monsoon.

In general, in these experiments, dry surface moisture anomalies tend to persist for longer periods than moist surface anomalies; this effect is more pronounced if the anomaly is initially present at the onset of the summer season. These investigations demonstrate the presence of dynamical feedbacks in the mutual interaction of soil moisture and large-scale atmospheric processes; these feedbacks contribute to climatic persistence. The model studies generally suggest that this effect is stronger for droughts and dry anomalies.

Mesoscale models

Detailed 3-D models on the mesoscale are numerical laboratories for the study of processes on scales that cannot be explicitly represented in the global models. Land-atmosphere interaction experiments with mesoscale models have tended to focus on the effect of surface heterogeneities on convection and cyclogenesis. Several numerical studies of the evolution of the dry line over the southern Great Plains (Sun and Ogura 1979, Lanicci et al. 1987, Chang and Wetzel 1991, Fast and McCorcle 1991) indicate that gradients in surface moisture availability lead to a significantly altered pre-storm atmospheric environment.

In the absence of significant synoptic wind, variations in surface properties — such as soil moisture — drive spatial variability in the energy fluxes, inducing a local thermally-direct circulation which in turn affects the net vertical transport of mass, energy, and momentum for the region as a whole. Mesoscale models have successfully replicated such sea-breeze and land-breeze phenomena; Segal and Arritt (1992) provide a summary and bibliography.

One-dimensional PBL models

Lower-dimensional models provide insight by allowing specific processes to be isolated from the large, complex system. Sasamori (1970), Zdunkowski et al. (1975), and Siebert et al. (1992) use fine-grid numerical models of the coupled soil and atmosphere column to demonstrate the critical role of the soil moisture state in partitioning the incoming energy to latent and sensible heat fluxes. The partitioning of the available energy into sensible and latent heat in turn affects the PBL forcing of the ground and turbulent transfer efficiency at the surface. The 1-D model of Camillo et al. (1983) explicitly accounts for the feedback mechanisms between the land–surface energy and moisture balances, in order to estimate regional evapotranspiration. Raddatz (1993)

includes a vegetation cover to study the sensitivity of the PBL to transpiration and heat and moisture diffusion in the soil column. Ek and Cuenca (1994) demonstrate the significant impact of variation in soil–texture parameters on the surface fluxes and boundary–layer development, particularly for dry to moderate soil moisture conditions.

1.2.2 Simple models

Reduced mathematical models simplify the system to a small number of equations, in which the relationship between land-atmosphere parameters and solutions is more transparent than in the numerical models, with their many equations in as many unknowns. These approaches trade detailed physical realism for analytic tractability and insight. The chief role of these simplified models is to focus on clearly identifying and quantifying the physical processes that constitute two-way land–atmosphere interaction and develop into feedback mechanisms. The model introduced in this thesis is designed to meet these same requirements.

Examples of previous such attempts at simplified modeling have focused exclusively either on the water or on the energy balance at the surface. Otterman (1990) develops ordinary differential equations in two variables (air and ground temperature) for the surface-effected warming of the planetary boundary layer; the solution incorporates two-way thermal exchange and demonstrates the role of land-surface radiative properties in the surface-to-PBL heat transfer efficiency. Entekhabi et al. (1992) use a univariate stochastic differential equation to derive probability density functions of soil moisture, incorporating the water-mass feedback mechanism of precipitation recycling. The model described in this thesis is a four-variable system of stochastic differential equations, including both energy and water-mass feedback processes.

1.2.3 Regional evaporation and energy advection

Evaporation — the expenditure of energy to effect the phase change of water from its liquid to its more mobile vapor phase — couples the energy and water mass exchanges at the land-atmosphere interface. Brutsaert (1988) discusses the history of scientific understanding of evaporation, and current approaches to modeling this critical process. Many of these approaches (the combination equation, Penman–Monteith, Priestley–Taylor) can be considered one-way interactions, in the sense that they describe the atmosphere acting on, but not responding to, the moisture state of the soil. Efforts to incorporate the two-way interaction include the Bouchet-Morton

complementary relationship (Bouchet 1963, Morton 1976) (accounting for the energy made available when evaporation is not occurring at the potential rate) and its further development in Brutsaert and Stricker's (1979) advection-aridity approach, as well as studies of fetch length and boundary-layer formation. De Bruin (1983) and McNaughton (1976) use simple budget expressions for the planetary boundary layer (PBL) to estimate the influence of surface evaporation control on energy advection and enhanced evaporative demand. Betts et al. (1994) show that enhanced surface evaporation into the PBL also increases the diurnal cycle in available energy for convection, which in turn affects the cloudiness and precipitation over the region.

1.2.4 Precipitation-temperature relationships

A number of statistical studies show that the observational record reflects the influence of land–atmosphere interaction on climate variability. van den Dool (1984) shows that the persistence in monthly mean air temperature (MMAT) is strongly influenced by the hydrothermal inertia of the land surface. Huang and van den Dool (1993) further demonstrate that in inner continental regions, positive anomalies in MMAT are preceded by strong negative anomalies in monthly mean precipitation (MMP). The highest (negative) lagged cross-correlation is evident in interior continental United States and the lag period is one month (or less). Zhao and Khalil (1993) analyze extended climatological records and confirm the strong MMAT-MMP negative correlation over the interior continent, especially in summer. Kemp et al. (1994) search for temporal discontinuities and dissimilarity in recovery from different sign anomalies in the same records. They show that drought periods are characterized by variability characteristics that are not evident in the record when conditions are near normal. The influence of feedback mechanisms are thus important to the study of climate variability.

1.3 Goals and Overview

The major hypothesis guiding this work is that the nonlinearity and inherent feedbacks in the coupling of water and energy in the two-way interaction between the soil and the near-surface atmosphere are significant factors in the statistical behavior of hydroclimatic anomalies. For example, can these linkages explain why dry anomalies are more likely to persist and intensify than moist anomalies? Stationary probability distributions do not provide information about the temporal behavior of excursions

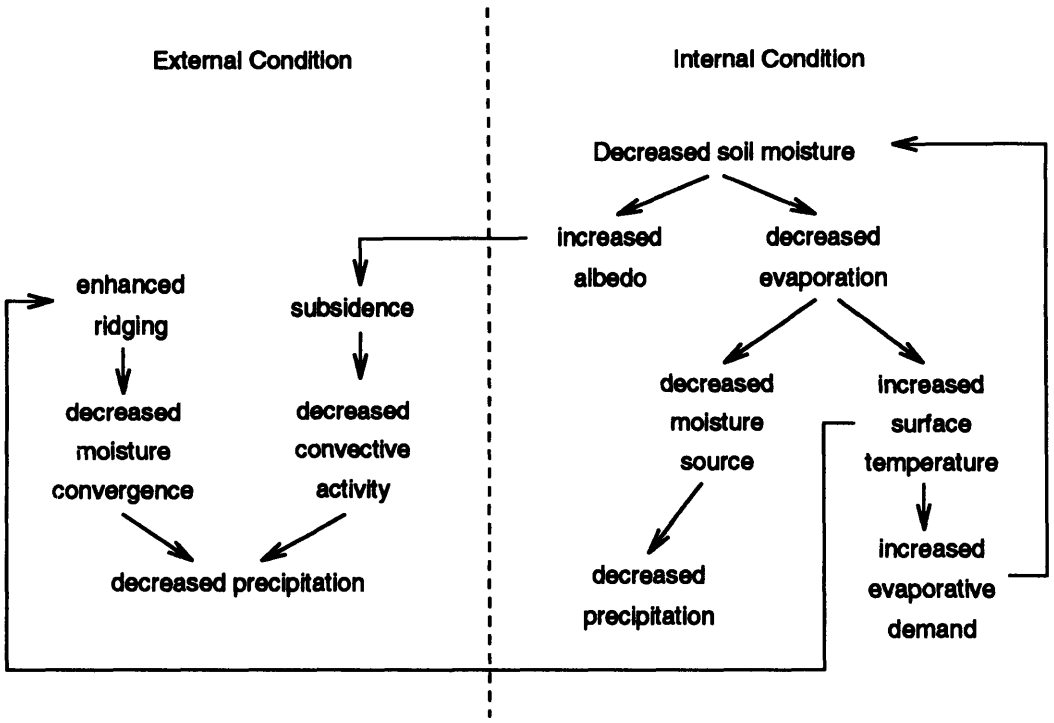

Figure 1-2: Summary of external dynamic processes affecting precipitation (left) and internal feedbacks involving soil moisture (right). After Meehl (1994).

from the mean. The decorrelation time scale in an auto-regressive model (such as applied by Delworth and Manabe 1988, 1989) is a linear measure of persistence, and does not distinguish between the characteristics of transition from normal to dry or moist conditions, and the recovery of normal conditions from anomalies of opposite sign. A physically–based stochastic model is used here to provide quantitative measures for the strength of pathways hitherto only qualitatively presented, as in Figure 1-1.

Figure 1-2 distinguishes between internal (or local) and external (or large-scale) conditions that can contribute climatic feedback. This figure uses a negative precipitation anomaly as an example; similar diagrams could be constructed for every process linking the land and the atmosphere through exchanges of mass and energy. In each case, local (internal) versus large-scale (external) factors may be distinguished. As the arrows connecting the two columns indicate, the local and external conditions affect one another. The model discussed herein pertains to the right-hand side of diagrams such as Figure 1-2. The local feedbacks are isolated by treating the large-scale forcing as random perturbations, essentially severing the right-to-left arrows.

The limitations of numerical models of the atmosphere are due to the fact that the

investigation of land-atmosphere interaction and its role in modulating the variability of climate requires integration periods on the order of decades so that reliable low-frequency statistical features associated with the long memory of the land component are established. Such multi-decadal simulations are computationally burdensome and cannot be routinely and repeatedly performed. Furthermore, there are numerous other interactions and transients in the numerical atmospheric models which make it difficult to isolate the partial effect of components. The model presented herein is part of a class of models that may be used in parallel with numerical atmospheric models to investigate the role of land-atmosphere interaction and temporal variability. Some of the details (and major processes) that are neglected in the model discussed here are implicitly part of atmospheric models; nonetheless some simulations and analyses may be performed with the analytical or stochastic construct here that are not feasible with the atmospheric models. Depending on the objective of the analysis, the trade-off between these two classes of land-atmosphere interaction models may be used to define an optimal multi-level and multi-scale investigative approach.

Chapter 2 describes the formulation of the land-atmosphere problem in terms of a system of four coupled ordinary differential equations and explores the system's equilibrium behavior and sensitivity. In Chapter 3, randomness is added to the model forcing and the properties of the response are described. Chapter 4 explores the temporal characteristics of the system's recovery from anomalous states, and Chapter 5 is a quantitative analysis of the physical sources of positive and negative feedbacks in the coupled water–energy system. Finally, in Chapter 6, the work is summarized and its implications and future extensions are discussed.

Chapter 2

Analytical Formulation

2.1 Introduction

The goal of the modeling exercise described in this Chapter is to obtain a description of the land-atmosphere system that can be subjected to available analytical techniques. To that end, the modeling philosophy is to substantially simplify the system, while maintaining the interactions as realistically as possible.

The relative simplicity of the present formulation will shed light on feedback (both hydrologic and meteorologic) causes and effects. Extension of the model to include random forcing (Chapter 3) is made in the form of the multivariate Îto equation, a system of stochastic ordinary differential equations. The formulation allows the computation of joint probability density functions for the state variables and conditional statistics relevant to the termination or amelioration of anomalous conditions. These statistical measures may be derived for various values of external or internal parameters using analytical methods. In addition to its analytic tractability, the model's computational simplicity allows the creation of long time series in simulation mode, from which serial cross-dependence may be derived.

2.2 Slab Model

The model represents the area-averaged surface hydrothermodynamic balance for an inner-continental region of characteristic length L and the region's interaction with the near-surface portion of the overlying atmosphere. This lumped model treats the soil layer and the near-surface atmosphere as reservoirs with storage capacities for heat and water. The transfers between the reservoirs are regulated by four states:

depth-averaged relative soil saturation (or soil moisture, s), soil temperature (T_g), air-slab specific humidity (q_m) and air-slab potential temperature (θ_m).

The horizontal extent of the region (L) is conceptually equivalent to the length scale over which generally homogeneous heat and moisture conditions are present, and over which advective and radiative effects can equilibrate. In mid-continental regions without marked orography, such an area may cover up to 10^4 to 10^5 km^2.

The soil layer is assigned an active depth and a porosity. The capacity of the soil to absorb incident water is modeled as dependent on the depth-averaged relative soil saturation; this approximation neglects the instantaneous dynamics of infiltration and exfiltration, but is appropriate for longer climatic time scales.

The atmospheric reservoir is treated as a developed, vertically-mixed turbulent boundary layer with height h, on the order of 1 km. We refer to this layer as the "air slab." In this idealized mixed layer, specific humidity and potential temperature, defined as

$$\theta = T \left(\frac{p_{ref}}{p} \right)^{(R_d/C_p)} , \tag{2.1}$$

are, by definition, invariant with height. Here, T is the thermodynamic temperature, p the pressure, p_{ref} a reference pressure, and R_d and C_{pa} the dry-air gas constant and specific heat under constant pressure. Customarily, p_{ref} is taken as 1000 mb. Potential temperature is, by definition, conserved under adiabatic pressure change; it is therefore the appropriate conserved temperature quantity in a well-mixed, unsaturated layer, as opposed to actual temperature, which does change with height. Specific humidity [g H_2O per kg air] is also conserved under adiabatic mixing. The model assumes a gradient in both humidity and potential temperature in the surface sublayer, defined as the first few to tens of meters above the land surface. The turbulent fluxes of sensible and latent heat into the mixed–layer require a surface–to–mixed–layer gradient; however, the turbulent flux parameterization used in this model (described in Section 2.2.4) does not require the specification or assumption of temperature or humidity profiles within the surface sublayer.

The model profiles of potential temperature and specific humidity are shown schematically on the right in Figures 2-1 and 2-2, respectively.

Figure 2-1 illustrates the model energy balance. The two energy states are air-slab potential temperature (θ_m) and ground temperature (T_g). The fluxes are treated as follows (beginning on the left of the figure) : A fraction of the solar (shortwave) radiation at the top of the atmosphere (RS_e) is reflected by clouds; of what arrives at the land surface (RS), a fraction is reflected according to the albedo (α), and the

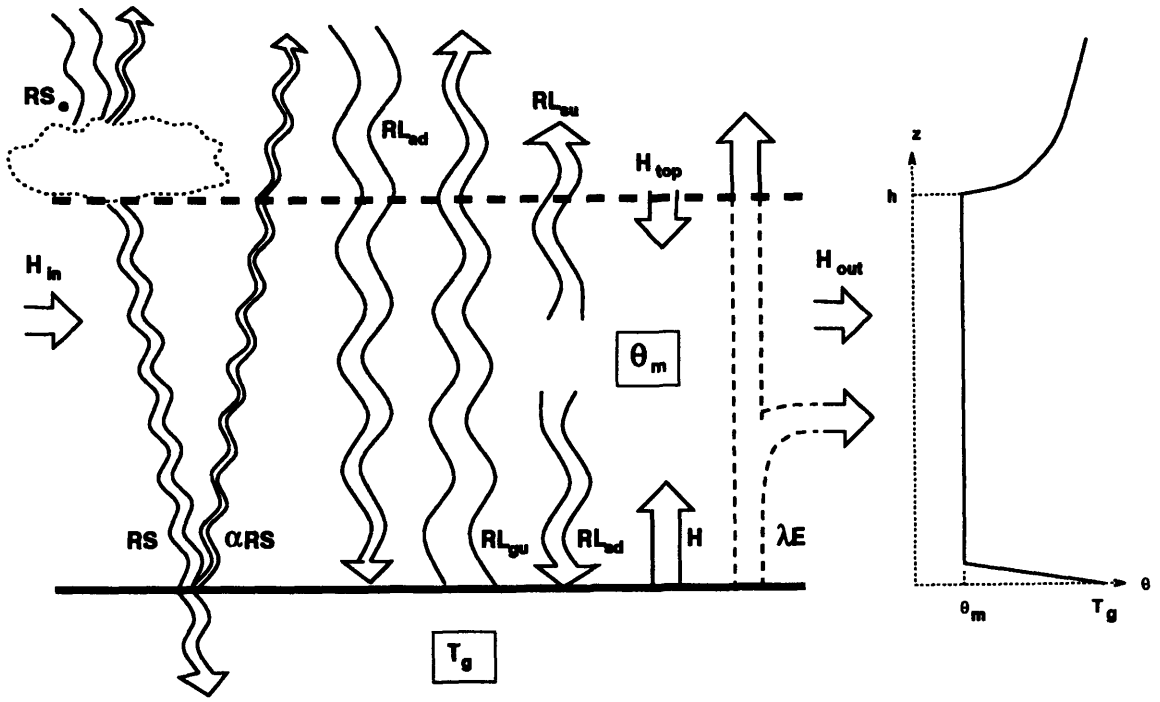

Figure 2-1: The slab model energy budget. The states and fluxes are shown on the left, and the assumed potential temperature profile on the right.

remainder is absorbed in the ground reservoir. Thermal radiation from the overlying atmosphere (RL_{ad}) is partially absorbed in the air slab, according to the slab emissivity/absorptivity (ϵ_{col}, a function of air-slab thickness and humidity), and the remainder reaches the land surface. The air slab itself radiates in the longwave, both upward (RL_{su}) and downward (RL_{sd}); and the ground supplies an upward longwave flux (RL_{gu}), a portion of which is absorbed in the air slab, according to ϵ_{col}. The surface turbulent fluxes of latent (λE) and sensible (H) heat are taken as positive when directed upward from the ground to the air, and the turbulent entrainment at the top of the slab (H_{top}) is taken as positive when directed upward out of the slab. Consistent with the assumption of adiabatic mixing in the shallow air slab, condensation is assumed to occur above the turbulently-mixed boundary layer; therefore, the latent heat of condensation does not contribute to the model's air-slab energy balance (as indicated by the dashed lines for λE in Figure 2-1). The lateral advection of sensible heat is indicated by H_{in} and H_{out}.

The water mass balance is illustrated in Figure 2-2. The water mass states are slab specific humidity (q_m) and relative soil saturation (s). Precipitation (P) is formed from the combined contributions of laterally advected water vapor (Q_{in}) and evaporation from the ground (E). A fraction of precipitation becomes runoff (R) and leaves

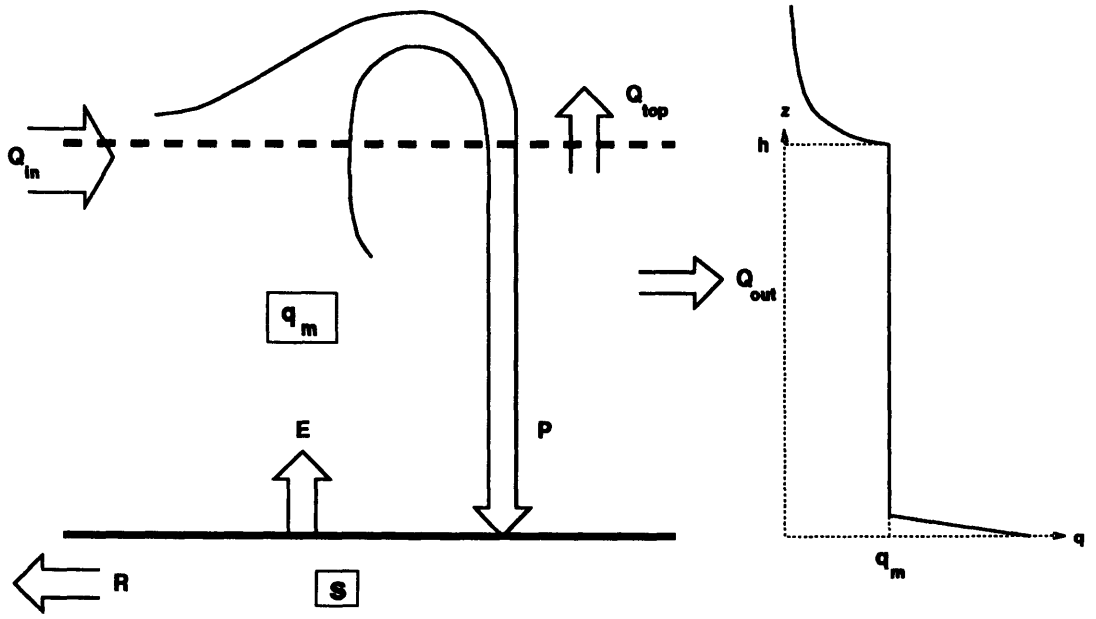

Figure 2-2: The slab model water budget. The states and fluxes are shown on the left, and the assumed specific humidity profile on the right.

the system, and the remainder is added to the ground reservoir. Water vapor is lost from the air slab by lateral outflow across the fixed boundaries of the region (Q_{out}). The entrainment of dry air across the top of the mixed layer is indicated by Q_{top} (positive upwards, indicating that the effect of this entrainment is to dry the slab).

2.2.1 Coupled energy and water balance equations

Using the symbols introduced in Figures 2-1 and 2-2 and Appendix A, Brubaker and Entekhabi (1994) write the heat and water budgets for the air slab and the soil layer. The result is a set of four differential equations for the time evolution of the energy and water state variables:

$$\frac{ds}{dt} = \frac{1}{\rho_w n Z_h}[P - R - E] \tag{2.2}$$

$$\frac{dq_m}{dt} = \frac{1}{(p_s - p_h)/g}[Q_{\text{in}} - Q_{\text{out}} + Q_{\text{top}} + E - P] \tag{2.3}$$

$$\frac{dT_g}{dt} = \frac{1}{Z_t C_{\text{soil}}}[RS(1-\alpha) + RL_{\text{ad}}(1-\epsilon_{\text{col}}) + RL_{\text{sd}} - RL_{\text{gu}} - H - \lambda E] \tag{2.4}$$

$$\frac{d\theta_m}{dt} = \frac{1}{C_{\text{pa}}(p_s - p_h)/g}[(RL_{\text{ad}} + RL_{\text{gu}})\epsilon_{\text{col}} - RL_{\text{sd}} - RL_{\text{su}} + H_{\text{in}} - H_{\text{out}} + H + H_{\text{top}}] \; . \tag{2.5}$$

The functional forms and parameterizations of the terms in (2.2) through (2.5) are discussed in Sections 2.2.2–2.2.6.

Equations (2.2) to (2.5) express the interlocking nature of soil and near-surface atmospheric water and energy states. The soil water mass and energy budget equations (2.2) and (2.4) share the term E; evaporation is both an output of water mass and an expenditure of the energy of phase change; in addition, the dependence of the soil volumetric heat capacity (C_{soil}) on s links these two equations. The air-slab water mass and energy equations (2.3) and (2.5) are coupled by the humidity dependence of the longwave fluxes RL_{sd} and RL_{su} and of the column emissivity (ϵ_{col}). The soil and air-slab heat states T_{g} and θ_{m} are linked by the turbulent sensible heat flux (H) and the radiative exchanges between the air slab and the soil (RL_{gu} and RL_{sd}), appearing with opposite signs in (2.4) and (2.5). For the soil and air-slab water mass states, the coupling is the difference $P-E$, the net vertical transfer of water mass from the air to the soil, which appears with opposite sign in (2.2) and (2.3). Atmospheric moisture (2.3) affects ground temperature (2.4) via the humidity dependence of the longwave fluxes.

The denominators in (2.2) through (2.5) represent the storage capacities of the respective heat and water reservoirs in the slab model. The product $\rho_{\text{w}} n Z_{\text{h}}$ in (2.2) is the active soil pore volume in terms of water mass per unit area; ρ_{w} is the liquid water density, n is the soil porosity, and Z_{h} the hydrologically active soil depth. In (2.4), $Z_{\text{t}} C_{\text{soil}}$ is the soil layer bulk heat capacity, equal to active soil volume per unit area (or thermally active depth, Z_{t}) multiplying the volumetric soil heat capacity. The term $(p_{\text{h}} - p_{\text{s}})/g$ in (2.3) and (2.5) is the air slab mass per unit area, where p_{h} is the pressure at h, the top of the air slab, and p_{s} is the surface pressure. The mixed–layer depth variables h, p_{h}, and p_{s}, are invariant in this model; p_{s} is set to 1000 mb [equal to p_{ref} in equation (2.1)]. In (2.5) the column mass multiplies the air specific heat at constant pressure (C_{pa}) to give the air-slab bulk heat capacity.

The effect of the entrainment of warm, dry air due to the growth of the boundary layer depth is represented by the fluxes $Q_{\text{top}} = \rho \frac{dh}{dt} \Delta q$ and $H_{\text{top}} = \rho C_{\text{pa}} \frac{dh}{dt} \Delta\theta$ in equations (2.3) and (2.5), where Δq and $\Delta\theta$ are the difference between, respectively, the specific humidity and potential temperature of the mixed layer and the drier air directly above the height of the mixed layer.

2.2.2 Radiative fluxes

The shortwave solar radiation reaching the ground (RS) is modeled as

$$RS = RS_e\,(B_1 + B_2 N_s) \tag{2.6}$$

where RS_e is the shortwave flux density at the top of the atmosphere, and the term in parentheses is a correction for cloud, in which N_s is sunshine duration (the ratio of actual to total possible hours of sunshine) and B_1 and B_2 are empirical constants. We use averaged values of the constants given for several midwestern U.S. cities in Brutsaert (1982, p. 132). We estimate N_s as a function of near-surface relative humidity, as discussed below [equations (2.17)-(2.18)]. RS_e is computed as a function of latitude and day of the year (and time of day, if the diurnal cycle is included):

$$RS_e = S\left(\frac{d_m}{d}\right)^2 \cos\theta_0 \tag{2.7}$$

where S is the solar constant (1353 W m^{-}2), d_m/d the ratio of mean to instantaneous earth-sun distance (here assumed equal to one), and θ_0 the solar zenith angle. For daily values of insolation, integration of (2.7) gives

$$RS_e = \frac{S}{\pi}\left(\frac{d_m}{d}\right)^2 (H_o \sin\lambda_o \sin\delta + \cos\lambda_o \cos\delta \sin H_o) \tag{2.8}$$

where λ_o is latitude, δ the solar inclination angle, and H_o the half-day hour angle (Liou 1980).

A fraction of RS is reflected by the land surface according to the surface albedo (α), which we model as a function of soil moisture as follows:

$$\alpha = 0.17 - 0.085s\,, \tag{2.9}$$

similar to Idso et al. (1975). The soil becomes lighter in color and more reflective as it dries.

The upwelling ground thermal flux (RL_{gu}) is computed according to the Stefan-Boltzmann law; soil emissivity is generally very near unity, so we set it equal to one; Thus,

$$RL_{gu} = \sigma T_g^4 \tag{2.10}$$

To compute the atmospheric thermal fluxes (RL_{da}, RL_{sd}, and RLsu), we use a broad-

band, plane-parallel slab emissivity formulation, following Brutsaert (1975), adjusted to suit this model's assumed temperature and moisture profiles; the derivations appear as Appendix B. The clear-sky downwelling longwave flux density from the air column above the mixed–layer air slab is:

$$RL_{\text{adc}} = \epsilon_{\text{effective}}\, \sigma T_{\text{h}}^4 \tag{2.11}$$

where $\epsilon_{\text{effective}}$ is an effective emissivity for the overlying atmosphere (see Appendix B) and T_{h} is the absolute temperature at height h, i.e.,

$$T_{\text{h}} = \theta_{\text{m}} \left(\frac{p_{\text{h}}}{p_{\text{s}}} \right)^{R_{\text{d}}/C_{\text{pa}}} . \tag{2.12}$$

The expressions for the clear-sky longwave fluxes downward at the bottom, and upward at the top, due to radiation within the air slab itself may be given in terms of slab potential temperature by virtue of its defined relationship to actual temperature in the mixed layer. Thus,

$$RL_{\text{suc}} = \sigma \theta_{\text{m}}^4 \epsilon^{\uparrow}(q_{\text{m}}) \tag{2.13}$$

$$RL_{\text{sdc}} = \sigma \theta_{\text{m}}^4 \epsilon^{\downarrow}(q_{\text{m}}) \tag{2.14}$$

where $\epsilon^{\uparrow}$ and $\epsilon^{\downarrow}$, the effective longwave emissivities of the mixed-layer air column, are functions of q_{m} and take into account the profile of actual temperature (T) in the mixed layer (see Appendix B). Because T decreases with height and the effect of humidity on the absorption path length is weighted by the square-root of pressure, $\epsilon^{\downarrow}$ is greater than $\epsilon^{\uparrow}$. These terms are defined and derived in Appendix B. The longwave radiation fluxes in (2.10) and (2.11) are attenuated by partial absorption in the mixed layer air column, assuming absorptivity equal to emissivity (Kirchoff's law for a black-body), and taking the column emissivity (see Appendix B) to be

$$\epsilon_{\text{col}} = 0.75 a^{1/7} \tag{2.15}$$

where a is the scaled amount of (mainly water vapor) mass in the air column between p_{h} and p_{s}. The mixed layer air column absorbs the impinging longwave energy according to $\epsilon_{\text{col}}(RL_{\text{da}} + RL_{\text{gu}})$, and the amount $(1 - \epsilon_{\text{col}})RL_{\text{da}}$ reaches the ground, where it is fully absorbed.

Clouds are efficient gray-body emittors; their effect is modeled by an empirical

correction multiplying the clear-sky longwave fluxes,

$$K = 1 + 0.17N_c^2 \tag{2.16}$$

(TVA 1972) where N_c is cloudiness (the fraction of sky covered by cloud). Due to observational bias in climate records, cloudiness and sunshine duration sum to about 120 percent — rather than the expected 100 percent — on a seasonal basis (Angell 1990). Because the empirical cloud corrections in (2.16) and (2.6) are derived from those biased records, we use

$$N_s + N_c = 1.2 \tag{2.17}$$

to obtain the value of N_s required in (2.6).

Cloudiness, N_c, is parameterized as a function of relative humidity in the mixed-layer,

$$N_c = 1.0 - 0.8\exp(-RH_{\text{surf}}) \, . \tag{2.18}$$

Equation (2.18) is developed specifically for this model, to determine cloudiness as a function of the model states; its applicability to other uses is not implied. The cloudiness term N_c ranges between 0.2 (when RH_{surf} is 0) and 0.71 (when RH_{surf} is 1.0); thus the allowed range of sunshine duration N_s is from 0.49 to 1. In (2.18) RH_{surf} is the relative humidity of the mixed-layer air just above the surface sublayer where the actual temperature may be assumed approximately equal to θ_m,

$$RH_{\text{surf}} = \frac{q_m}{q^*(\theta_m, p_s)} \tag{2.19}$$

where saturation specific humidity $q^*(T,p)$ is computed from the integrated Clausius-Clapeyron relation,

$$q^*(T,p) \approx \frac{\epsilon_0 e_{s0}}{p} \exp\left[-\frac{\lambda}{R_v}\left(\frac{1}{T_0} - \frac{1}{T}\right)\right] \, . \tag{2.20}$$

where R_v is the gas constant for water vapor, ϵ_0 the psychrometric constant (0.622), and ϵ_{s0} and T_0 reference values ($\epsilon_{s0} = 6.11$ mb at $T_0 = 273.15K$). Equation (2.20) neglects the temperature dependence of the latent heat of vaporization (λ); the range of λ is small over the temperature range of the model. Brutsaert (1982) gives more detailed expressions for saturation specific humidity.

2.2.3 Advection and precipitation

The lateral advection of atmospheric water vapor is modeled as follows,

$$Q_{\text{in}} = \frac{(p_{\text{s}} - p_{\text{h}})/g}{L} U_z q_{\text{in}} \tag{2.21}$$

$$Q_{\text{out}} = \frac{(p_{\text{s}} - p_{\text{h}})/g}{L} U_z q_{\text{m}} \tag{2.22}$$

where Q_{in} is the horizontal flux of water vapor into the region, and Q_{out} the horizontal flux of water vapor out of the region, both vertically integrated from the surface to the top of the air slab. These quantities are treated as an air mass flow multiplying an effective specific humidity for the inflow (q_{in}) and multiplying the region's mixed-layer specific humidity (q_{m}) for the outflow. The latter treatment assumes that air leaving the region possesses the humidity characteristic of the region. The air mass flow per unit area is the product of column mass between p_{s} and p_{h}, and low-level wind speed, divided by the length of the region in the direction of the air flow.

Similar to the lateral advection of moisture, there may be lateral advection of sensible heat from surrounding regions. To include such fluxes [H_{in} and H_{out} in equation (2.5)], equations similar to equations (2.21) and (2.22) may be included, with the difference that q_{in} is replaced by $C_{\text{pa}}\theta_{\text{in}}$ and q_{m} by $C_{\text{pa}}\theta_{\text{m}}$. Under conditions of strong and persistent temperature gradients, the advection of sensible heat is important. In our model, over spatial scale L, the large fluxes of energy are principally in the vertical (large radiative exchange between the soil, air slab, and free atmosphere). Lateral advection of sensible heat may be easily incorporated using an additional parameter θ_{in}. Here, to isolate the local water–energy coupling, we neglect this source of heating or cooling.

Precipitation is the most important forcing to the soil water balance and is the most difficult to parameterize in this lumped model. We apply a formulation similar to the Kuo (1965) scheme used in numerical atmospheric models. Here, the moisture entering the mixed layer is partitioned between moistening the air and condensing out as precipitation, according to a moistening parameter, b. This parameter dictates what fraction of the entering water vapor goes to moistening the air-slab; the remaining fraction becomes precipitation,

$$P = (1 - b)(Q_{\text{in}} + E)\,. \tag{2.23}$$

The partitioning of precipitation into infiltration and runoff (R) is treated as a

function of soil moisture, with the runoff ratio expressed as

$$\frac{R}{P} = \varepsilon s^r \tag{2.24}$$

(Entekhabi et al. 1992, Rodriguez-Iturbe et al. 1992). Equation (2.24) expresses the fact that moist soils generally partition a larger fraction of the precipitation into infiltration-excess and partial-area runoff losses. Rather than an event-based surface runoff function, this expression comprises the longer-term total runoff, incorporating percolation and baseflow (as in Eagleson 1978) .

2.2.4 Surface turbulent fluxes

Turbulent mixing across the gradient of temperature and humidity in the surface sublayer results in fluxes of latent and sensible heat into the mixed layer. We apply Stull's (1994) parameterization for mixed convection, which was developed specifically for mixed-layer models and estimates surface fluxes based on surface and mixed-layer values of moisture and temperature. By this scheme, the sensible heat flux is

$$H = C_{\mathrm{HE}} \left(T_{\mathrm{g}} - \theta_{\mathrm{m}}\right) \rho C_{\mathrm{pa}}, \tag{2.25}$$

and the potential evaporation (that which would occur if the soil were saturated, all else being equal) is

$$E_{\mathrm{p}} = C_{\mathrm{HE}} \left[q^*(T_{\mathrm{g}}, p_{\mathrm{s}}) - q_{\mathrm{m}}\right], \tag{2.26}$$

where C_{HE} is the transfer coefficient for the turbulent fluxes. Stull (1994) gives

$$C_{\mathrm{HE}} = (0.001 U_z + 0.00025 w_{\mathrm{B}}) \ . \tag{2.27}$$

In (2.27), w_{B} is a buoyancy velocity scale, given by

$$w_{\mathrm{B}} = \left[\frac{g}{\theta_v} h \Delta\theta_v\right]^{1/2} , \tag{2.28}$$

where θ_v is the virtual potential temperature in the mixed-layer, and $\Delta\theta_v$ is the virtual potential temperature difference between the skin (surface) and mixed-layer. In the model, humidity in the mixed layer tends to be very low, with the result that $\theta_v \approx \theta_{\mathrm{m}}$. For $\Delta\theta_v$, we use $\theta_{\mathrm{m}} - T_{\mathrm{g}}$, which neglects the small buoyancy contribution of humidity differences.

The term containing U_z in equation (2.27) accounts for forced convection due to

wind shear. The term containing w_B accounts for buoyancy-driven free convection. The constants multiplying the velocities are values estimated by Stull (1994) for summer in Oklahoma. Saturation specific humidity at the soil-air interface, $q^*(T_g, p)$ is computed from equation (2.20).

Actual evaporation is a fraction of the potential value, controlled by the evaporation efficiency (β), that is,

$$E = \beta E_p \tag{2.29}$$

where β is modeled as a function of soil moisture,

$$\beta = s^c \,. \tag{2.30}$$

Mahfouf and Noilhan (1991) compare a number of formulations of β. Actual evaporation equals the potential value when the soil is at or near saturation. In most formulations, the evaporation efficiency (or moisture availability factor) β decreases to zero as the soil dries. Equation (2.30) is a general expression of this relationship. The formulation of β is examined in further detail in Chapter 4 where transitions from soil-controlled to energy-limited evaporation regimes are considered.

2.2.5 Air-slab thickness and slab-top air entrainment

In nature, the atmospheric mixed-layer height (h) is not constant. The mixed layer grows during the day as surface heating generates turbulent mixing, which entrains the overlying air. The layer shrinks or may even vanish at night, in the absence of solar radiation. Furthermore, h varies from day to day and from season to season, due to variability in the mechanisms producing turbulent mixing.

In the interest of model simplicity and analytic tractability, we have decided against fully modeling the diurnal evolution of mixed-layer depth in our climatic model (2.2) – (2.5). Instead, the entrainment of warm, dry air from above during the mixed layer's growth and decay is parameterized. The diurnal details of boundary layer height and the momentum budget are important in pollution transport studies, for example, but this study is concerned with the longer time scales of the region's heat and moisture states. Otterman (1990) also assumes a fixed h in a linear model of land-atmosphere thermal interaction. The model's fixed h is a major assumption; we now discuss its implications.

As an illustration of the mixed layer's behavior in nature, Figure 2-3 shows the diurnal course of potential temperature profiles during the development of the mixed

layer for a June day at the FIFE site in Kansas. The first sounding, at 0607 (Central Standard Time), shows a stable profile with $d\theta/dz$ greater than zero at all heights. By 0820, the surface has warmed enough that the near-surface profile is unstable ($d\theta/dz < 0$); convection has begun and warmer air is being entrained from above. By 0938, a layer with nearly uniform θ extends to 500 m. As sensible heat flux from the surface and turbulent motion at the top of the mixed layer continue to bring warm air into the mixed layer, it increases its potential temperature to 28°C at 1713. Due to entrainment of the overlying air, the mixed-layer has grown in depth to more than 1500 m in this time. In the last frame of Figure 2-3, the highly stable capping inversion is clearly visible, and the disappearance of the near-surface unstable layer is noted. By 0557 of the following day (the dashed line in the first frame of the figure), the profile has returned to its stable starting point, in the absence of surface heating and turbulent mixing.

To compute the diurnal evolution of h fully requires consideration of turbulent kinetic energy, including both free and forced turbulence production (Tennekes and Driedonks 1981). Mixed-layer growth models have shown good skill at predicting mixed-layer height over the daylight hours and with appropriate initial conditions and forcing terms (Steyn 1990, Novak 1991, Culf 1992, Driedonks 1982). Some work has been done on modeling the nocturnal collapse of the mixed layer (Binkowski 1983). Because the processes controlling dh/dt at night are different from those controlling it during the day, a discontinuous function would be required.

We assume that the model h is, in an averaged sense, an effective value for longer than daily time scales, but the model equations must account for the roles played by variability in h. First, h appears in the denominators in (2.3) and (2.5) through the value of p_h, controlling the bulk heat and water storage capacities of the air slab. Second, the longwave atmospheric fluxes and emissivity/absorptivity are computed as functions of slab thickness. Neglecting variability in h may create the result that the soil is artificially insulated by a blanket of air. When the layer is too thick (thin), its rate of change of humidity and temperature will be slower (faster) than it should, because a given energy input is assumed to be mixed into too large (small) an air mass. We note that, although in reality the buoyantly-mixed layer collapses at night, a residual layer may remain (Stull 1988), possessing the characteristics of the layer before its collapse. The air near the ground cools and a stable profile develops with high potential temperature remaining in the elevation range of the former mixed layer. If this is the case, then the fixed h assumption is not as drastic for radiative calculations as it would be for momentum and pollutant transport modeling.

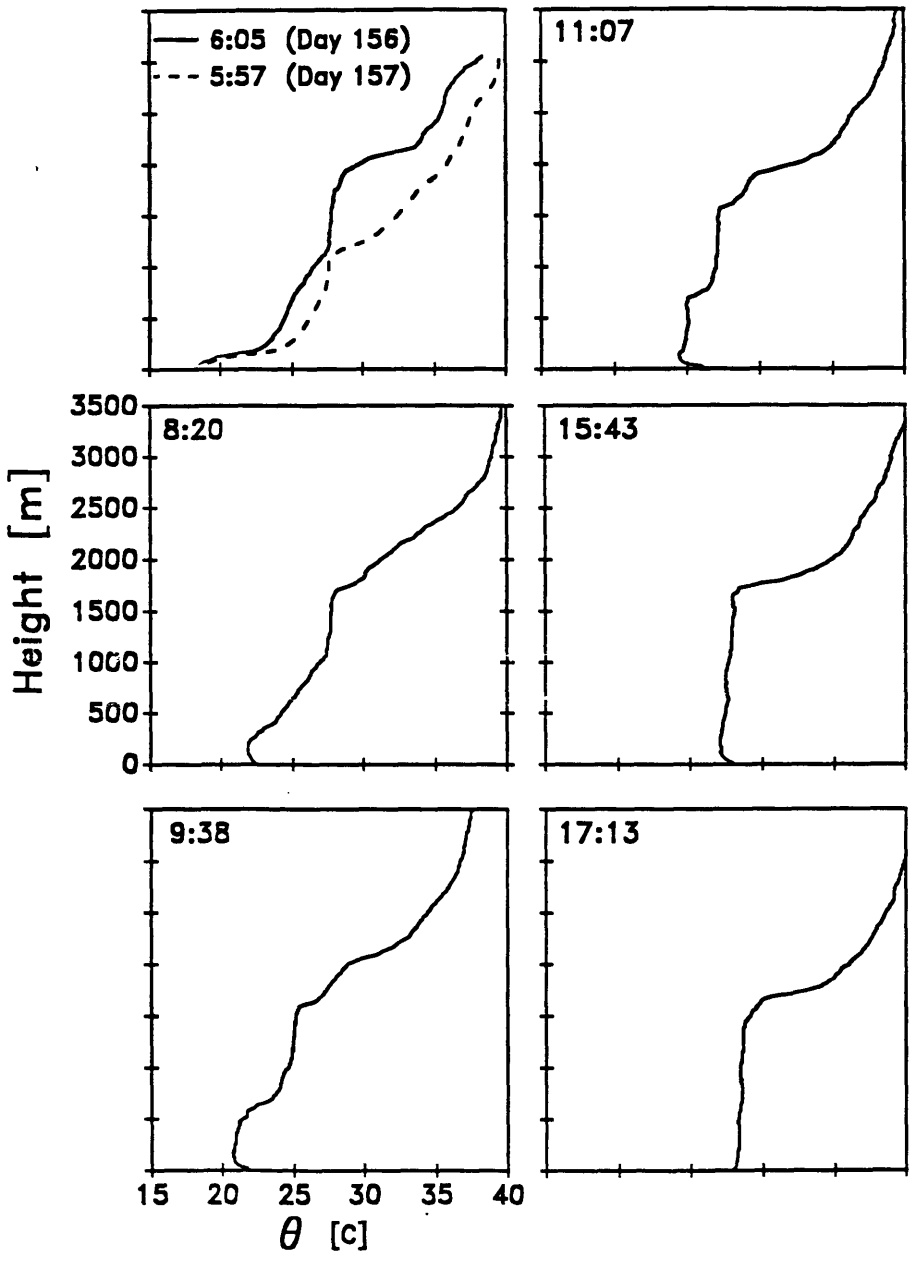

Figure 2-3: The development of the convectively-mixed layer, as shown by the profiles of potential temperature during a June day in FIFE. Times are given in Central Standard Time.

Additionally, air motion at night generates mixing by forced convection, sustaining a thin mixed layer. The expressions for the turbulent fluxes, which assume exchanges of heat and moisture between the surface and the entire thickness of the air slab, are less correct for a nighttime profile than for the daytime. In general, the turbulent surface fluxes are quite small at night and do not contribute strongly to daily average values.

Finally, the turbulent sensible heat flux at the slab top for a developing mixed layer under standard potential-temperature profile assumptions (Tennekes 1973, Driedonks 1981) is given by

$$\overline{\theta' w'}_{\mathrm{h}} = \Delta\theta \frac{dh}{dt} \tag{2.31}$$

where $\overline{\theta' w'}_{\mathrm{h}}$ is the correlation between potential temperature and vertical air motion at height h, $\Delta\theta$ the jump in potential temperature at the base of the inversion that caps the mixed layer, and dh/dt the instantaneous rate of mixed-layer growth. A frequent assumption in the mixed-layer literature (e.g., Tennekes 1973) states that the inversion–base sensible heat entrainment is proportional to the surface sensible heat flux,

$$H_{\mathrm{top}} = -A_{\mathrm{top}} H \,. \tag{2.32}$$

The entrainment of dry air due to the growth of the boundary layer is also represented in equation (2.3) and can be treated similarly to the entrainment of potential temperature. In this version of the model, we neglect the equivalent effects on air-slab specific humidity but note that the entrainment of potential temperature simultaneously decreases the relative humidity of the mixed air layer as well as warming it. By using (2.32), we include the effect of mixed-layer growth on sensible heat entrainment, while avoiding the introduction of additional differential equations in h and $\Delta\theta$, and the jump in humidity at the capping inversion.

2.2.6 Soil heat capacity

The volumetric heat capacity of the soil is expressed as a mass-weighted average of the heat capacities of the soil components including the soil water,

$$C_{\mathrm{soil}} = (1.94 v_{\mathrm{min}} + 2.50 v_{\mathrm{org}} + 4.19 s\, n)\, 10^6 \quad [\mathrm{J\ m^{-3}\ K^{-1}}] \tag{2.33}$$

where v_{min} and v_{org} are, respectively, the volume fractions of mineral soil and organic matter, and the constants are the product of density and specific heat for each

component (Brutsaert 1978, p. 146).

2.3 Equilibrium Behavior and Sensitivity to Parameters

2.3.1 Climatic equilibrium

The four model equations (2.2) – (2.5) are solved for equilibrium, i.e., $ds/dt = 0$, $dq_m/dt = 0$, $dT_g/dt = 0$, $d\theta_m/dt = 0$. For the *climatic equilibrium* solutions, the solar forcing is at perpetual summer solstice, using the daily insolation rate with no diurnal cycle. The model parameters consist of climatic forcing terms (wind speed U_z and incoming humidity q_{in}) and a set of internal regional properties (soil type, reservoir volumes). Values of the internal parameters were selected as appropriate to a mid-latitude continental interior. These parameters were not used to tune the model output; rather, the values listed in Table 2.1 were selected and estimated independently from the literature. The moisture partitioning parameter, b, is set to 0.3, consistent with other schemes of this type reported in the literature (Kuo 1965, Arakawa and Chen 1986). As a test of model sensitivity to the climatic forcing parameters, the equilibrium solution was obtained for a range of values of the large–scale (external) parameters q_{in} and U_z. In all cases, the numerical technique obtained the same solution vector from disparate initial guesses; this is evidence — although not rigorous proof — that the solutions are unique. The default-parameter climatic equilibrium solution is denoted by $\hat{x}$ and tabulated in Table 2.2.

The turbulent heat fluxes couple the soil and atmospheric heat and moisture states, and they work to reduce gradients in these states at the boundary. The wind-speed controls the efficiency of this coupling through the turbulent transfer coefficient in (2.27). As a test of the model, Figure 2-4 shows the difference in the soil-air temperature as the wind-speed is changed over a range. The land-atmosphere coupling is increased (temperature gradient at boundary reduced) when forced convection is efficient at high wind-speeds. With reduction of the wind-speed, as evident in Figure 2-4, both the soil and air-slab temperatures rise and the temperature difference increases slightly, as the heat forcing is dissipated by alternate mechanisms, namely thermal radiation and buoyant (free) convection.

With increasing advective moisture supply (q_{in}), the equilibrium precipitation and soil saturation increase (Figure 2-5). Evaporation, after increasing nearly linearly

Table 2.1: Default Parameter Values in the Equilibrium Experiments

Symbol	Definition	Units	Value
h	height of mixed layer (air slab)	[m]	1000
p_s	surface pressure	[mb]	1000
p_h	pressure at slab top	[mb]	880
A_{top}	entrainment parameter (Eq. 2.32)	[ ]	0.2
b	moistening parameter (Eq. 2.23)	[ ]	0.3
Z_h	hydrologically active soil depth	[m]	0.2 (climatic) 0.15 (diurnal-cycle)
Z_t	thermally active soil depth	[m]	0.4 (climatic) 0.15 (diurnal-cycle)
n	soil porosity	[ ]	0.25
v_{min}	mineral volume fraction of soil	[ ]	0.5
v_{org}	organic volume fraction of soil	[ ]	0.25
c	exponent in evaporation efficiency (Eq. 2.30)	[ ]	1.0
ε	coefficient in runoff ratio (Eq. 2.24)	[ ]	1.0
r	exponent in runoff ratio (Eq. 2.24)	[ ]	2.0
U_z	mixed-layer wind speed	[m s^{-1}]	4.0
L	length scale of region	[km]	500
q_{in}	effective humidity of incoming air	[g kg^{-1}]	8.0

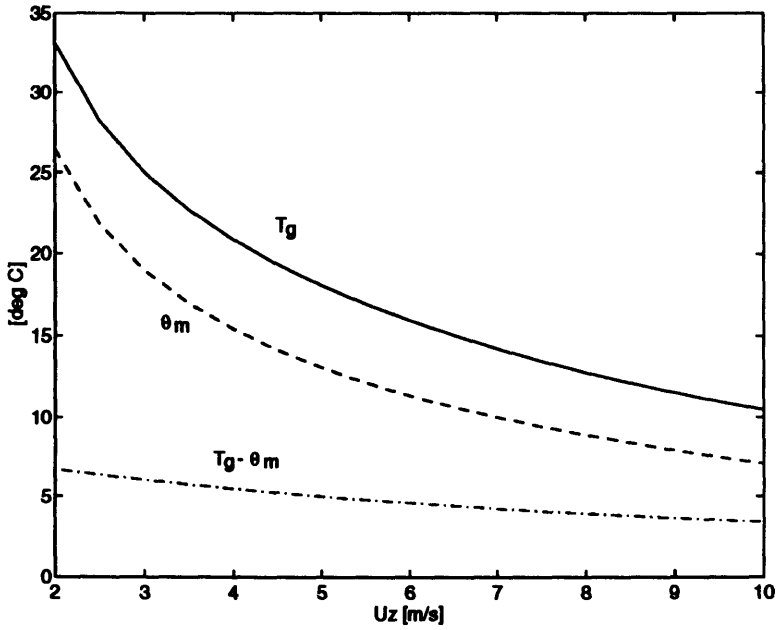

Figure 2-4: Soil-layer temperature, air-slab potential temperature and the temperature difference, in the climatic equilibrium solutions, as functions of the near-surface wind speed, U_z.

in the low range of q_{in}, attains a nearly constant value of about 5.5 mm day^{-1}. This asymptotic value reflects the fact that actual evaporation is the product of potential evaporation and soil saturation [equation (2.29)]. Potential evaporation (the dotted curve in Figure 2-5), a nonlinear function of soil temperature, is high when the system is dry (and warm), decreasing as the equilibrium solution becomes moister (and cooler). This decreasing E_p function multiplies the increasing s, resulting in the nearly constant E.

Sensitivity tests were also conducted on b; the results are similar to the sensitivity to q_{in}, in the reverse sense: increasing b partitions more incoming moisture to the air slab and less to the soil layer. Thus, P and s decrease, and E_p increases with increasing b; E is nearly constant for b less than about 0.40.

2.3.2 Equilibrium with diurnal cycle

The model is designed to apply to short-term climate time scales (weeks to months). However, the realism of the characterization is tested by examining the model response to a diurnal cycle in the solar forcing. For these tests, the interactive soil depths (Z_t and Z_h) are set to 0.15 m, representing appropriate penetration depth for waves of heat and moisture over the course of a day. Otherwise, the parameters are assigned

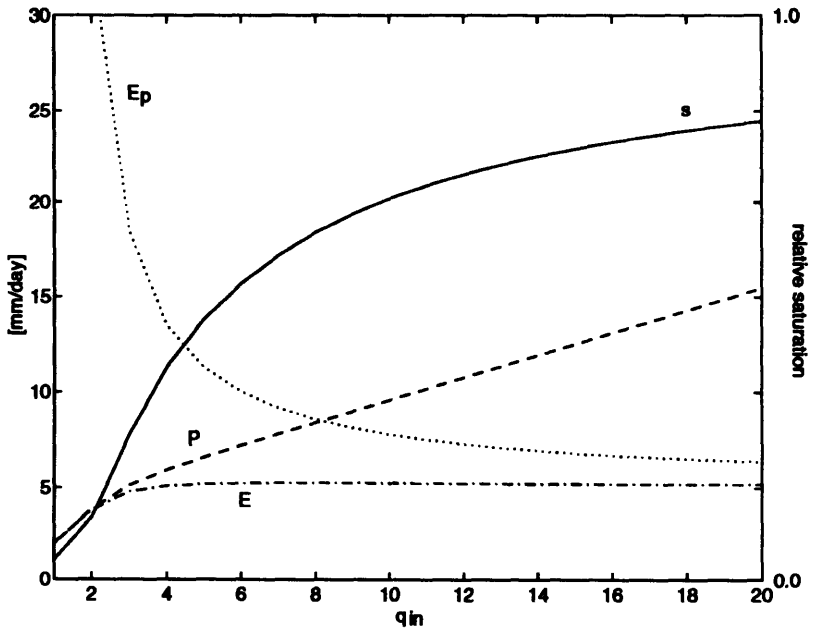

Figure 2-5: The water mass fluxes and soil saturation in the climatic equilibrium solutions, as functions of the effective incoming specific humidity, q_{in}.

the same values as in the climatic equilibrium solutions (Table 2.1); the model was not calibrated to match any particular data set. The *diurnal-cycle* equilibrium is defined as the solution $\mathbf{x}(t)$ such that $\mathbf{x}(t) = \mathbf{x}(t - 24 \text{ hours})$, that is, a periodic diurnal cycle in the model states. The diurnal-cycle solution mean values and ranges are tabulated in Table 2.2, denoted by angled and square brackets, respectively. The expected value of a nonlinear function of $x(t)$ is, in general, not equal to the nonlinear function evaluated at the expected value of x. The nonlinearity of the model is most apparent in the temperature variables: $\langle T_{\text{g}} \rangle$ and $\langle \theta_{\text{m}} \rangle$ are somewhat cooler than $\widehat{T_{\text{g}}}$ and $\widehat{\theta_{\text{m}}}$.

The equilibrium diurnal cycles in the temperature variables and the turbulent fluxes are shown in Figure 2-6. T_{g} has a diurnal range of 10 degrees, taking its lowest value of 15.5°C at 0600 and peaking at 25.7°C at 1600. The model's four-hour lag between maximum solar radiation (at 1200) and maximum ground temperature (at 1600) is consistent with theory (Lettau 1951) and observation (e.g., Novak and Black 1985). The mixed-layer potential temperature (θ_{m}) has a smaller amplitude than T_{g}, about 2 degrees, and lags the ground temperature, reaching its minimum at 1100 and its maximum at about 2200. The latent and sensible heat fluxes peak at 1530. The heat flux into the ground (G) is positive (warming the ground) until 1600 when it reverses sign (cooling the ground). By definition, the model energy fluxes are

Table 2.2: Comparison of Climatic and Diurnal-Cycle Model Equilibrium Solutions

	Climatic Equilibrium	Diurnal-cycle Equilibrium	
	$\widehat{x}$	$\langle x \rangle$	$[\ x_{\min} \quad x_{\max}\ ]$
s [ ]	0.613	0.615	[0.610 0.621]
q_m [g kg^{-1}]	4.27	4.25	[4.12 4.37]
T_g [deg C]	20.9	20.3	[15.5 25.7]
θ_m [deg C]	15.4	15.1	[14.1 16.0]
P [mm day^{-1}]	8.42	8.38	[6.32 11.1]
E [mm day^{-1}]	5.26	5.21	[2.26 9.06]
E_p [mm day^{-1}]	8.58	8.46	[3.67 14.7]
H [W m^{-2}]	48.3	48.8	[3.81 109]
R_{net} [W m^{-2}]	198	198	[-81 610]

balanced, due to computing G as the closure in (2.4).

The model's T_g is averaged over a soil slab 0.15 m deep, and θ_m over a 1 km deep air slab; furthermore, the model results are for a diurnal cycle at equilibrium, i.e., there is no net change in storage over the course of a day. Therefore, direct comparisons with observations of the diurnal cycle of soil surface temperature or near-surface air temperature are difficult, because most observations do not describe slab-averaged values or equilibrium conditions. Computationally allowing the surface radiation to act on the entire layer rather than modeling the vertical diffusion of energy through the soil results in an earlier maximum and a less sinusoidal diurnal cycle, in comparison to observations (see, e.g., Novak and Black 1985).

In general, observational studies of the boundary layer focus on θ in the developing boundary layer during the day, not the averaged quantity with which the model θ_m should be compared. In Figure 2-7, we present data on the diurnal range of potential temperature at different heights in the atmosphere during nine clear days in the FIFE experiment (Days 152, 154, 155, 156, 192, 227, 228, 229 and 232, spanning early June through mid-August). These days were selected from the full set of clear days because radiosonde data were available covering the hours 0600 to 1800 CST, corresponding to about one hour after sunrise through two hours before sunset; these sampling times should capture the minimum and maximum θ in the lowest kilometer of the atmosphere. For each sounding, we averaged the potential temperature over layers of 100 m thickness; the diurnal θ range for each 100 m layer equals the difference

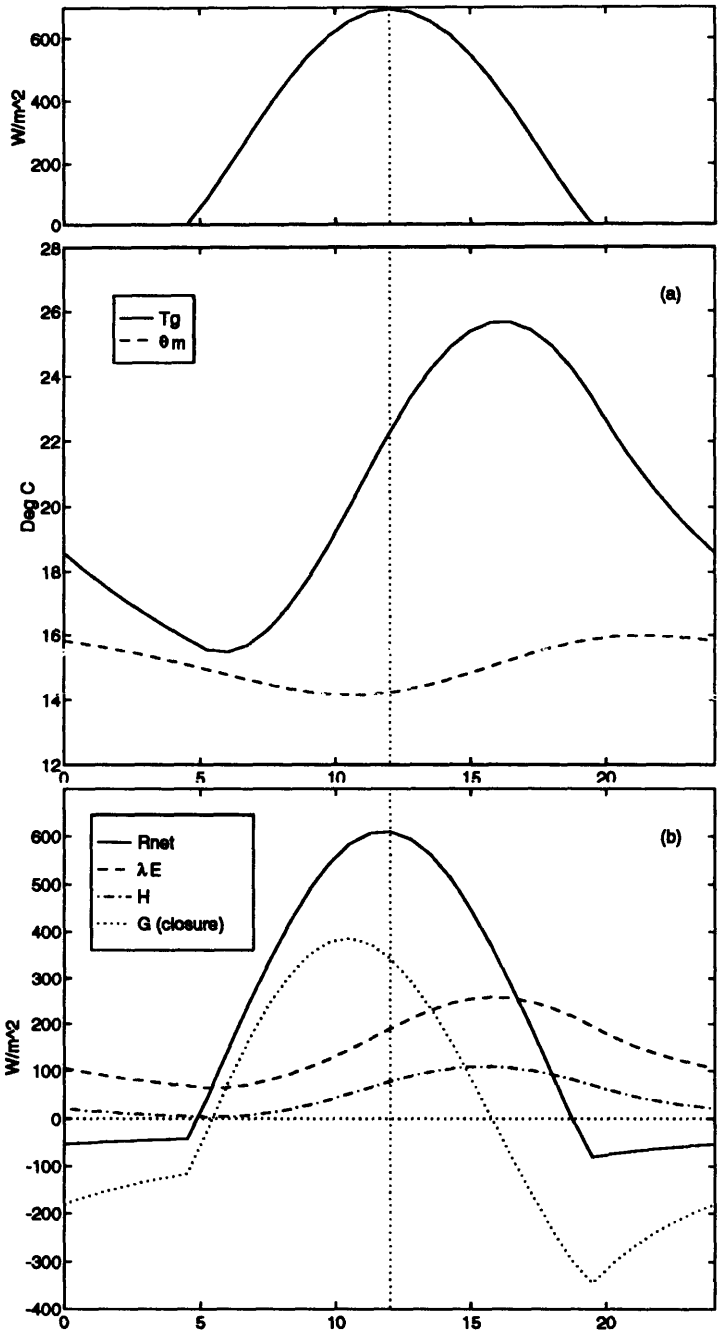

Figure 2-6: The diurnal cycles of soil temperature and slab potential temperature (a), and components of the surface energy budget (b) in the diurnal-cycle equilibrium solution; the prescribed solar forcing is shown at the top of the figure.

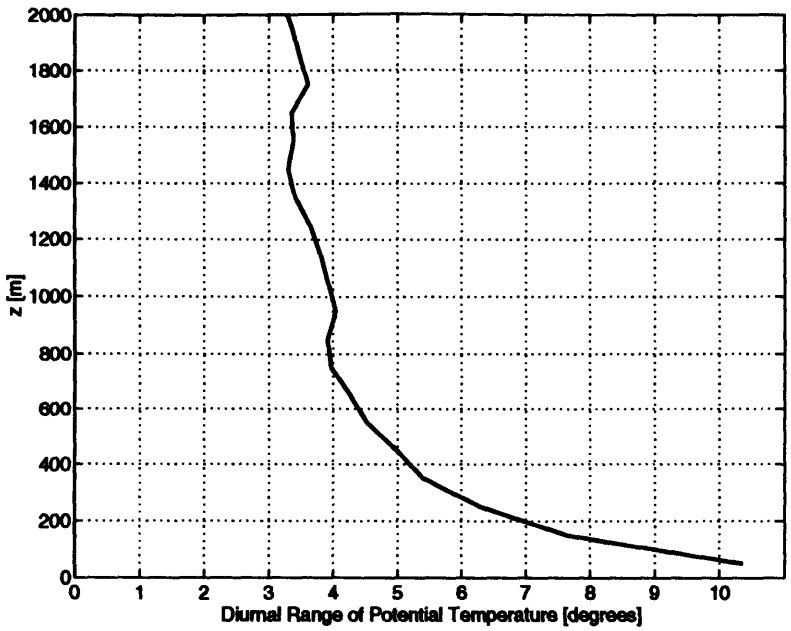

Figure 2-7: Profile of the diurnal range of atmospheric potential temperature during nine clear days of FIFE IFCs 1, 2, and 3.

between the maximum and the minimum values of the layer-averaged θ. Figure 2-7 gives the mean diurnal range for the nine days analyzed; between 500 and 1500 m the daily range is about 4 degrees. The model diurnal range is lower than this composite mean value but is of the correct order of magnitude, when compared to the 10–degree range of soil temperature.

An important test of the model is whether the net energy at the soil surface is partitioned correctly between the latent and sensible heat fluxes. We compare the model to several sets of observations, with the following *caveats*: First, as noted above, the model results represent a climatic equilibrium state (average moisture, temperature, precipitation, cloudiness, etc.), which is not necessarily represented by any one-day set of observations; second, the surface energy exchange is controlled by site-specific factors including roughness length and soil albedo, and time-varying factors including solar radiation, wind speed, and soil moisture. To address the first issue, we selected smooth observational daily cycles, indicating consistency in the forcing throughout the day. For the second issue, we selected data sets that are representative of bare soil or sparse vegetation, where the data were taken near the summer solstice at middle latitudes (for compatibility in the solar forcing), under fairly moist bare soil conditions. The model was not tuned or calibrated to fit any of these observations. The studies selected for comparison are: (1) The SAMER 2

Table 2.3: Comparison of Model and Observed Diurnal Cycle of Surface Fluxes

Site/Study	Peak Value [W m^{-2}] (R_n)	(Time of Peak) ([Solar Time]) (H)	(λE)	Bowen Ratio at Noon
HAPEX-MOBILHY [1]	600 (1100)	180 (1245)	480 (1115)	0.35
Agassiz, B.C.[2]	660 (1200)	100 (1200)	400 (1300)	0.28
Boardman, Ore[3]	[N/A]	200 (1400)	400 (1430)	0.53
FIFE IFC 1,2,3 [4]	530 (1200)	120 (1100)	340 (1200)	0.35
Model[5]	610 (1200)	109 (1530)	260 (1530)	0.41

(1) June 16, SAMER 2. Values estimated from Fig. 6a of Noilhan and Planton (1989), except Bowen ratio at Noon, which is mentioned in the text.

(2) May 30. Values estimated from Fig. 2a of Novak and Black (1985).

(3) June 14. Values estimated from Figs. 5 and 6 of Doran et al. (1992), "corn" data.

(4) Summer months. Composite of FIFE IFC 1,2, and 3 (includes clear, cloudy, and overcast days). Values estimated from Fig. 6 of Smith et al. (1992).

(5) June 21. Model equilibrium solution with diurnal cycle.

Numerical values for (1)–(4) are ± 10 W m^{-2} in the energy terms, $\pm$ 15 min in the times, due to inaccuracy in reading from printed figures. For compatibility, the time axes have been shifted to solar time for each location.

site of HAPEX-MOBILHY as reported in Noilhan and Planton (1989) (June 16, soya over loam, $z_0 = 0.02m$); (2) a site at Agassiz, British Columbia, as reported in Novak and Black (1985) (May 30, bare loam/silt-loam soil), and (3) a site near Boardman, Oregon, as reported in Doran et al. (1992) (irrigated corn field with sparse canopy). In addition, we compare the model diurnal cycles to composite data from the FIFE intensive field campaigns (IFCs) 1, 2, and 3, as calculated by Smith et al. (1992) . As a composite of clear, cloudy, and overcast days, these results are perhaps the best observational data for comparison with the steady-state model results.

In Table 2.3, we present the peak values and time of peak for H and λE, as well as the Bowen ratio ($H/\lambda E$) at noon for these studies and for the model equilibrium diurnal solution. The peak value and time of peak for net radiation (R_n) are included as well, as one check on the adequacy of comparison. The model is not in perfect

agreement with any of the observations, but there are considerable differences among the observations themselves. The model's noon Bowen ratio is close to those of all the selected observations, except Boardman, the highest of the observations. The model's peak H is higher and the peak λE lower than the observations. The model's peak λE and H occurs late, with respect to these data sets.

Another measure to test the model is the diurnal pattern of the partitioning between sensible- and latent-heat surface fluxes. Here we estimate the evaporative fraction, defined as $\lambda E/(R_{\text{net}} - G)$ and compare it with Verma et al.'s (1992; Figure 5) observations at FIFE. Figure 2-8a shows the model's daytime evaporative fraction. Comparison with Verma et al.'s (1992) observations in Figure 2-8b is favorable, both in magnitude and diurnal shape, indicating that the model is capable of representing the moist thermodynamic factors that go into the determination of partitioning available energy into latent and sensible heat fluxes.

2.4 Summary

The land-atmosphere system for a large region is represented by a system of four ordinary differential equations, suitable for analysis in the form of the multivariate Fokker-Planck equation, when randomness is added in future work. The major assumptions of the model are adiabatic mixing in the boundary layer, and a time-invariant atmospheric boundary layer height (although the contribution of warm, dry air entrainment at the boundary-layer top is included).

The equilibrium solutions of the four-variable model are appropriate for mid-latitude continental climates. This result is satisfying, given that the model temperatures are not tied to any boundary value that would force them to a solution (such as a fixed deep-ground temperature) but rather evolve to equilibrium by satisfying the physical linkages and interactions among water and energy states. The diurnal phase and amplitude of the states and fluxes are further indicators of the model's validity and robustness; in particular, the lag between ground and air temperature maxima indicates that the land-air energy fluxes are operating correctly. The energy flux comparisons to data are inexact; however, the model appears to do a reasonable job of partitioning net radiation into sensible and latent heat fluxes in appropriate proportions for bare-soil mid-latitude summer conditions and over the diurnal cycle. The equilibrium response to the external forcing parameters wind speed and incoming effective specific humidity indicate that variability in these parameters will force variability in the states, when random noise is added to the model.

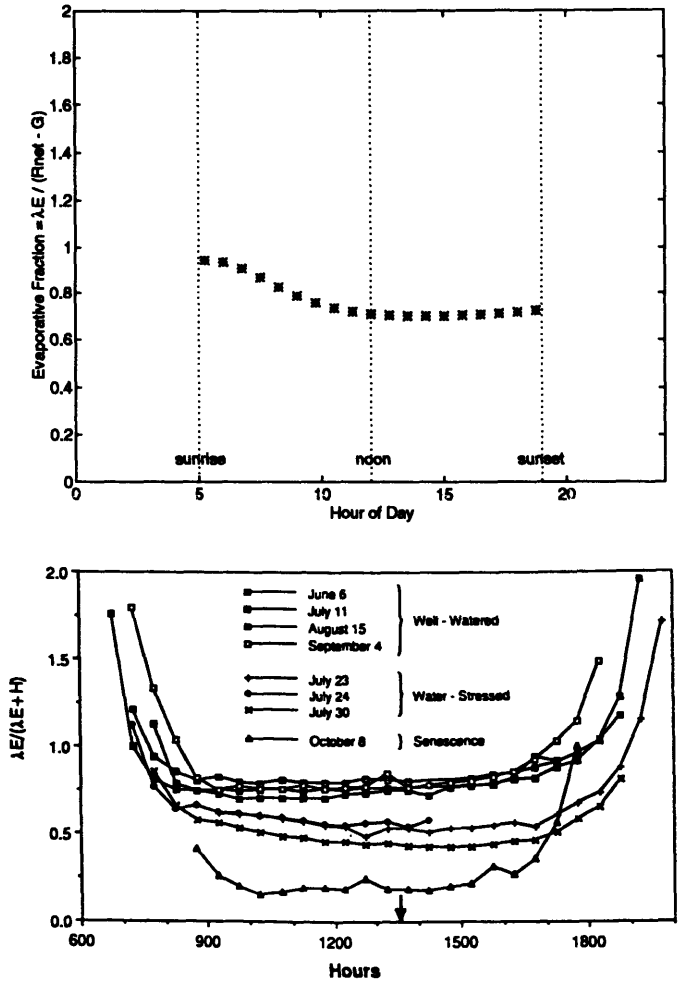

Figure 2-8: (a) Daytime Evaporative Fraction in the diurnal-cycle equilibrium solution. (b) Verma et al. (1992) observations of the diurnal cycle of evaporative fraction over water-stressed grasslands during the FIFE experiment.

Subsequent Chapters in this thesis explore the time scales of variability and co-variability in the model climate's response to a variable external forcing. This work will provide understanding of the role of water-energy coupling and land-atmosphere interaction in climatic variability and persistence.

Chapter 3

Stochastic Extension

3.1 Introduction

In this Chapter, feedback processes in land–atmosphere interaction are identified using the model of the soil and the turbulently–mixed near–surface atmosphere hydrothermal balance described in Chapter 2. The system of four ordinary differential equations is subjected to stochastic forcing, and the statistics of the heat and moisture states, as well as the fluxes that relate them, are computed. The closed-form mathematical construct of the model is exploited to systematically explore several land–atmosphere interaction processes and to specifically identify and quantify their influence on the statistical signature of the hydroclimatic regime.

The analysis of Chapter 2 is expanded to include the influence of noise on the system and to map the univariate and joint statistics of the states under random excitation. The source of noise is considered to be in the advection of air mass; the regional wind speed is taken to be composed of a mean component with additions of uncorrelated white-noise as perturbations around this mean value. The wind speed parameter is selected as the source of randomness because it is a key physical parameter, affecting both large–scale advection and local turbulence. This study is limited to the case of white-noise forcing in order to specifically isolate those interactions within the system that filter the noise and preferentially add gain to the lower frequencies of the output. Thus, the factors in the land–atmosphere system that add memory and covariability may be identified and isolated.

The noise in the wind speed affects the moisture advection and turbulent fluxes at the surface. These effects are routed through the system via the internal mathematical structure of the system, i.e., through the coupled fluxes and states. The

variability, covariability, and serial dependence that are evident in the output of the excited dynamical system are thus due to the internal interactions between the soil and atmosphere water and energy states. The fluxes (radiation, turbulent fluxes, precipitation) are thus consistent with one another and adhere to strict physical limitations and constraints.

The resulting covariance structure is due to land–atmosphere interaction and is not prescribed *a priori*. This is in contrast to other approaches to the stochastic simulation of hydrologic and climatic state variables in which the covariability structure is an input parameter of the model (for example, the simulation of heat and moisture states by multivariate autoregressive–moving average [ARMA] time series analysis requires the definition of the covariability structure at the very outset).

3.2 System of Stochastic Differential Equations

The model is forced by solar radiation at the top of the atmosphere and by near–surface wind–speed, which advects moisture from the neighboring regions and determines the magnitude of the transfer coefficient for the surface turbulent fluxes. In Entekhabi and Brubaker (1994), wind–speed is taken to be composed of a mean component plus (zero–mean, serially–independent, normally-distributed) perturbations with variance σ_u^2,

$$U_z = \overline{U} + \sigma_u dw_t \qquad dw_t = N(0,1) \text{ and } E\left[dw_t dw_v\right] = \delta(t-v) \tag{3.1}$$

where $E[\cdot]$ is the expectation operator and $\delta(\cdot)$ is the Dirac delta function. Here noise dw_t is the increment of a Wiener process. Because of the differential formulation of this stochastic equation, its integration in time (using techniques reported in Pardoux and Talay 1984) is independent of the numerical time step.

The functions that are affected by (3.1) are the regional moisture advection terms Q_{in} and Q_{out} as well as the turbulent heat fluxes λE and H. The moisture and heat advection terms are given by:

$$\begin{bmatrix} Q_{\text{in}} \\ Q_{\text{out}} \\ H_{\text{in}} \\ H_{\text{out}} \end{bmatrix} = \frac{(p_s - p_h)/g}{L} \begin{bmatrix} q_{\text{in}} \\ q_m \\ \theta_{\text{in}} \\ \theta_m \end{bmatrix} \left(\overline{U} + \sigma_u dw_t\right) \tag{3.2}$$

The surface turbulent fluxes are given (after Stull 1994) as

$$H = \left[C_1\left(\overline{U} + \sigma_u dw_t\right) + C_2 w_B\right](T_g - \theta_m) \tag{3.3}$$

$$\lambda E = \beta\left[C_1\left(\overline{U} + \sigma_u dw_t\right) + C_2 w_B\right](q^*(T_g) - q_m) \tag{3.4}$$

where w_B is a buoyancy velocity scale. The variables in (3.1) – (3.4) are defined in Chapter 2 and tabulated in Appendix A.

In this application, only vapor convergence (Q_{in} and Q_{out}) is required to maintain a regional hydrologic cycle. Sensible heat convergence due to lateral temperature gradients (H_{in} and H_{out}) is small, relative to the large radiative exchanges between the soil, boundary–layer air, and the atmospheric profile. This parameterized heat advection is not necessary — in contrast with the moisture convergence, which is needed to maintain a hydrologic cycle.

The unit noise term is represented for an increment of time as the differential of the Wiener process dw_t. After substitution of (3.2) – (3.4) in (2.2) – (2.5) together with this definition, the time evolution of the system is described by a continuous stochastic differential equation that may be compactly written as

$$d\mathbf{x}_t = \mathbf{G}(\mathbf{x}_t)dt + \mathbf{g}(\mathbf{x}_t)dw_t\,, \tag{3.5}$$

where the time-varying state vector $\mathbf{x}_t = [s\ q_m\ T_g\ \theta_m]$ has been defined.

In (3.5), the deterministic function $\mathbf{G}(\mathbf{x}_t)$ represents the *drift* in the state variables, due to the radiative and turbulent fluxes as well as the steady component of moisture advection in incremental time dt. The four components of the drift function are as follows:

$$\begin{aligned}
G_1 &= \frac{1}{\rho_w n Z_h}\Big\{(1-R)(1-b)\,M q_{in}\overline{U} + \\
&\qquad [(1-R)(1-b)-1]\,\beta\left(C_1\overline{U} + C_2 w_B\right)\rho\left[q^*(T_g,p_s) - q_m\right]\Big\} \\
G_2 &= \frac{1}{(p_s-p_h)/g}\Big\{b\left[M q_{in}\overline{U} + \beta\left(C_1\overline{U} + C_2 w_B\right)\rho\left[q^*(T_g,p_s) - q_m\right]\right] - M q_m \overline{U}\Big\} \\
G_3 &= \frac{1}{C_{soil} Z_t}\{RS(1-\alpha) + RL_{ad}(1-\epsilon_{col}) + RL_{sd} - RL_{gu} \\
&\qquad - \rho C_{pa}\left(C_1 U_z + C_2 w_B\right)(T_g - \theta_m) \\
&\qquad -\lambda\beta\left(C_1\overline{U} + C_2 w_B\right)\rho\left[q^*(T_g,p_s) - q_m\right]\Big\} \\
G_4 &= \frac{1}{C_{pa}(p_s-p_h)/g}\{(RL_{ad} + RL_{gu})\,\epsilon_{col} - RL_{su} - RL_{sd} \\
&\qquad + (1+A_{top})\rho C_{pa}\left(C_1 U_z + C_2 w_B\right)(T_g - \theta_m) \\
&\qquad + M C_{pa}\theta_{in}\overline{U} - M C_{pa}\theta_m\overline{U}\Big\}
\end{aligned} \tag{3.6}$$

The fluctuating part of wind–speed affects the system in proportion to the deter-

ministic function $\mathbf{g}(\mathbf{x_t})$. Because the wind speed is a physical parameter of the system, the influence of its random fluctuations on the system is modulated by the state of the system at the time of the event [see (3.1) – (3.4)] The functional dependence of this *diffusion* term on the state $(\mathbf{x_t})$ indicates complexity in land–atmosphere interaction and the presence of multiplicative stochastic forcing. The four components of the diffusion function are as follows:

$$
\begin{aligned}
g_1 &= \tfrac{1}{\rho_w n Z_h}\{(1-R)(1-b)Mq_{in}+ \\
&\qquad [(1-R)(1-b)-1]\beta C_1\rho[q^*(T_g,p_s)-q_m]\}\sigma_u \\
g_2 &= \tfrac{1}{(p_s-p_h)/g}\{b[Mq_{in}+\beta C_1\rho[q^*(T_g,p_s)-q_m]]-Mq_m\sigma_u\}\sigma_u \\
g_3 &= \tfrac{1}{C_{soil}Z_t}\{\rho C_{pa}C_1(T_g-\theta_m)-\lambda\beta C_1\rho[q^*(T_g,p_s)-q_m]\}\sigma_u \\
g_4 &= \tfrac{1}{C_{pa}(p_s-p_h)/g}\{(1+A_{top})\rho C_{pa}C_1(T_g-\theta_m)+MC_{pa}\theta_{in}-MC_{pa}\theta_m\}\sigma_u
\end{aligned}
\tag{3.7}
$$

Although the system is forced by serially–independent white noise, the output of the model is serially dependent with some statistical memory, due to the storage and interactions in the system. The random fluctuations in wind speed that drive the system are routed and distributed among components of the system through the state-dependent fluxes of energy and water mass. Any resulting temporal covariability among the model states results from the physical linkages that are implicit in the model and not from pre–assigning a correlation structure to the variables.

3.3 *Control* Solution of Stochastic Model

The system of stochastic differential equations is numerically integrated in time, using an Euler-type discretization (Pardoux and Talay 1984). The advantage of this scheme over the Mil'shtein (1974) algorithm used in Entekhabi et al. (1992) is that the fluxes and other derived states may be uniquely determined for incremental periods of time. In these integrations, the assumed adiabatic condition of non-saturation in the mixed–layer is monitored and found satisfied. The statistical moments and lagged auto- and cross-covariances for the basic states and derived states are estimated for analysis. The model parameters for the *Control* case are identical to those used in Chapter 2 for equilibrium conditions (see Table 3.1). The solutions described in this Chapter are forced by a constant, daily–average solar input, at perpetual summer solstice, without a diurnal cycle.

Table 3.1: Parameter Values in the Control Stochastic Experiment

Symbol	Definition	Units	Value
h	height of mixed layer (air slab)	[m]	1000
p_s	surface pressure	[mb]	1000
p_h	pressure at slab top	[mb]	880
A_{top}	entrainment parameter for sensible heat at slab top	[ ]	0.2
b	moistening parameter	[ ]	0.3
Z_h	hydrologically active soil depth	[m]	0.2
Z_t	thermally active soil depth	[m]	0.4
n	soil porosity	[ ]	0.25
c	exponent in evaporation efficiency	[ ]	1.0
ε	coefficient in runoff ratio	[ ]	1.0
r	exponent in runoff ratio	[ ]	2.0
U_z	mean mixed-layer wind-speed	[m s^{-1}]	4.0
σ_u	standard deviation of wind-speed	[m s^{-1}]	1.5
L	length scale of region	[km]	500
q_{in}	effective specific humidity of incoming air	(g H_2O) (kg air)$^{-1}$	8.0

3.3.1 Marginal probability distribution of the states

The stochastic differential equation (3.5) representing land–atmosphere interaction is integrated, and the long-term statistical behavior is determined by computing relevant measures. Comparison of the equilibrium state $\hat{\mathbf{x}}$ of the model resulting from $\mathbf{G}(\hat{\mathbf{x}}) = 0$ and the central tendency of the stochastic case or expectation $E[\mathbf{x}_t]$ is illuminating in that it illustrates whether the covariabilities of heat and moisture in the land and atmosphere contribute to the definition of regional climate. Table 3.2 lists the deterministic solution values from Chapter 2 alongside the mean of the simulated stochastic time-series in (3.5) for the basic model states as well as selected fluxes.

The stochastic forcing as conceptually represented in (3.1) and more precisely defined in (3.5) is gaussian and serially independent. The model states are stochastic processes with joint distributions characterizing their fluctuations. Partly due to the fact that the noise is multiplicative as evident by the diffusion function $\mathbf{g}(\cdot)$ in (3.5), the model state stochastic processes are not necessarily gaussian. Figure 3-1 shows the estimated frequency distributions of the simulated time-series for the model states; they are representations of the marginal distributions of the state vector $\mathbf{x}_t$. The

Table 3.2: Moments of State Variables and Turbulent Fluxes

	Equilibrium Solution	Stochastic Solution								
		Control ($\sigma_u = 1.5$)			Low-variance ($\sigma_u = 1.0$)			High-variance ($\sigma_u = 2.0$)		
	$\hat{x}$ [Units]	$\overline{x}$	σ_x	γ_x	$\overline{x}$	σ_x	γ_x	$\overline{x}$	σ_x	γ_x
s	0.613 [ ]	0.612	0.029	-0.28	0.612	0.019	-0.18	0.612	0.039	-0.40
q_m	4.27 [g/kg]	4.27	0.32	0.85	4.27	0.21	0.54	4.27	0.43	1.20
T_g	20.9 [deg C]	20.9	1.9	0.38	20.9	1.3	0.25	20.9	2.5	0.52
θ_m	15.4 [deg C]	15.5	1.2	0.25	15.5	0.8	0.15	15.5	1.6	0.34
P	8.42 [mm/day]	8.41	2.61	0.06	8.41	1.74	0.04	8.41	3.49	0.09
E	5.26 [mm/day]	5.26	1.44	1.49	5.26	0.95	0.31	5.26	1.96	0.71
E_p	8.58 [mm/day]	8.65	2.52	0.62	8.62	1.65	0.39	8.69	3.45	0.90
H	48.3 [W/m^2]	48.4	21.5	0.95	48.4	14.1	0.62	48.6	29.2	1.31
R_{net}	198 [W/m^2]	199	11	-0.62	198	7	-0.40	199	15	-0.85

relative soil saturation and atmospheric potential temperature are nearly gaussian in form; their mean, standard deviation, and skewness $(\overline{x}, \sigma_x, \gamma_x)$ are tabulated in Table 3.2. The atmospheric specific humidity and both temperature variables are positively skewed; the skewness coefficient for humidity is 0.85, which indicates a strong departure from the gaussian character of the input noise. The difference in magnitude of the range for the two temperature states may be partially explained by the difference in the heat capacity of the air-slab and soil reservoirs. The heat capacity of the one-kilometer air slab is about 1.2×10^6 J K^{-1} m^{-2}, and that of the soil layer varies depending on the soil moisture content, but lies around 0.9×10^6 J K^{-1} m^{-2} for the mean state of the control solution. The higher range for ground temperature is also partially due to the fact that the energy forcing is accomplished by the absorption of solar radiation at the surface; the air slab is then heated mostly by thermal radiation from the land surface.

3.3.2 Marginal probability distribution of the fluxes

The frequency distribution of the moisture and energy fluxes are determined by analyzing the time series of the integrated stochastic differential equation. These states are consistent in that they are linked by covarying state variables. The precipitation is nearly gaussian (Figure 3-2) because it largely responds directly to the noise input. The coefficient of skewness for this derived state is small, as indicated in Table 3.2.

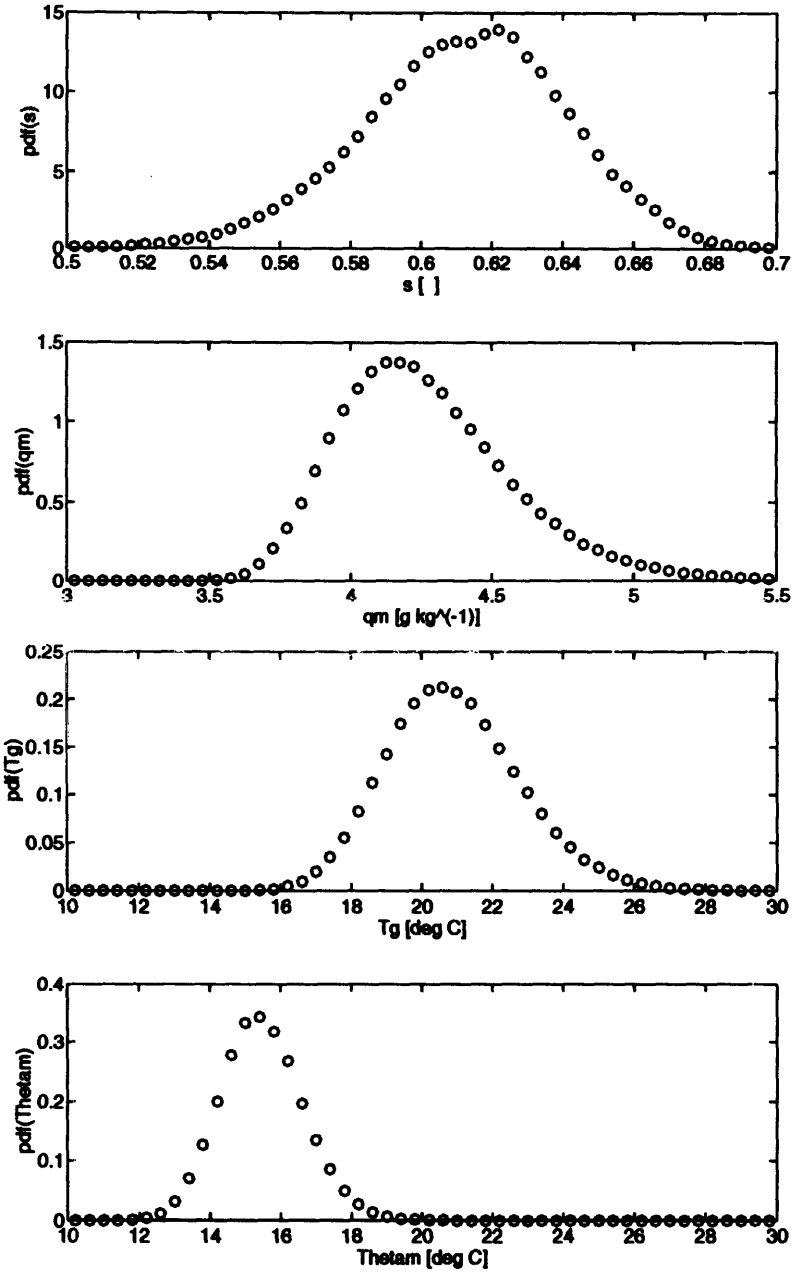

Figure 3-1: Probability density functions for the four state variables in the *Control* simulation: (a) relative soil saturation, (b) atmospheric specific humidity, (c) soil temperature, and (d) air potential temperature.

The land evaporation and potential evaporation in Figure 3-2 are highly skewed and have positive coefficients of skewness.

The sensible heat flux is sharply asymmetric as evident in Figure 3-2 (with skewness coefficient 0.95 as listed in Table 3.2). The sensible heat flux is the mechanism by which the ground temperature and the air temperature equilibrate at short timescales. Its magnitude is generally small because large imbalances are not allowed to persist, given this strong coupling tendency. At the same time, negative sensible heat fluxes are relatively less probable at perpetual summer solstice because the ground is heated by solar radiation, and any inversion in the temperature structure is soon destroyed by both free and forced convection. These two factors, a small mean and a tendency to limit sensible heat flux to be generally larger than zero, result in redistributing probability mass and creating a positive skew when the system is excited by random fluctuations.

The net radiation, on the other hand, is sharply skewed in the opposite direction, having a skewness coefficient of -0.62; Figure 3-2 clearly shows this characteristic. After solar radiation, the net radiation at the surface is mostly composed of outgoing terrestrial radiation, which is proprtional to the fourth power of ground temperature. When the net radiation is large or on the increase, the ground heats rapidly and the outgoing thermal flux from the surface becomes a more efficient cooling mechanism since the elevated temperature is raised to the fourth power. Large net radiation values are thus sharply constrained at the higher magnitude end; the statistical signature of this feedback is a redistribution of probability mass such that the skewness is large and negative.

The key role of the land surface in energy balance is the partitioning of available energy between the latent and sensible turbulent heat fluxes. A diagnostic measure of this partitioning is the Bowen ratio (Bo $= H/\lambda E$) which is physically related to the heat and moisture availability at the surface. Sensible heat is the relatively less efficient mechanism of dissipating heat from the surface; therefore, high Bowen ratios are associated with elevated temperatures. The sensible and latent heat flux values have a joint probability distribution that is consistent with heat and moisture availability at the surface. Due to the stochastic forcing and fluctuating values of temperature and moisture content at the surface, the Bowen ratio is a stochastic process in this model as well. Figure 3-3 shows the joint probability distribution of these fluxes for the *Control* simulation. Superposed on this figure are sloped lines of constant Bowen ratio. Consistent with the discussion above of the system's resistance to temperature inversions, very little probability mass lies in the region of negative

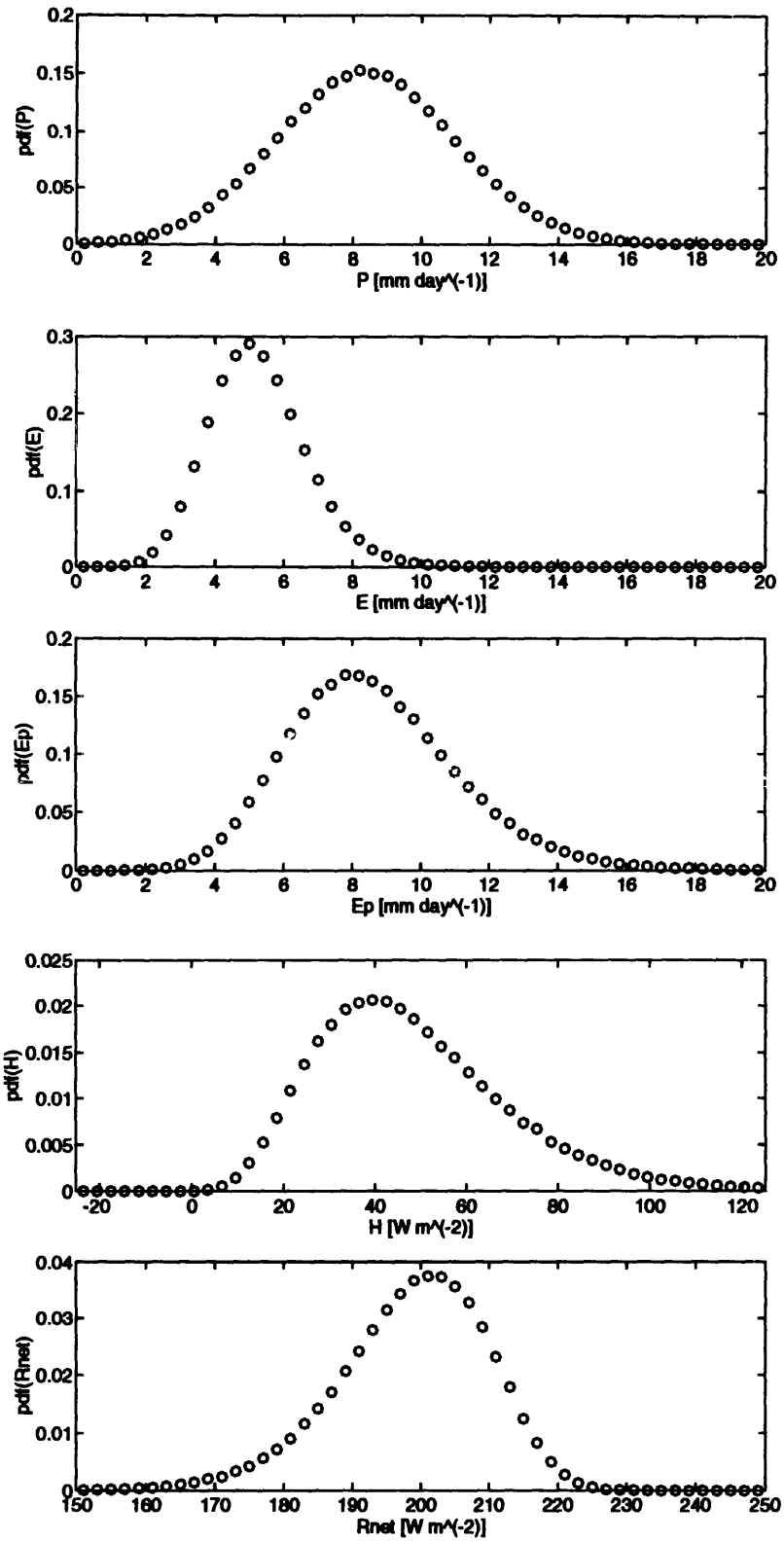

Figure 3-2: Probability density functions for fluxes in the *Control* simulation: (a) precipitation rate, (b) surface evaporation rate, (c) potential evaporation rate, (d) sensible heat flux, and (e) net radiation.

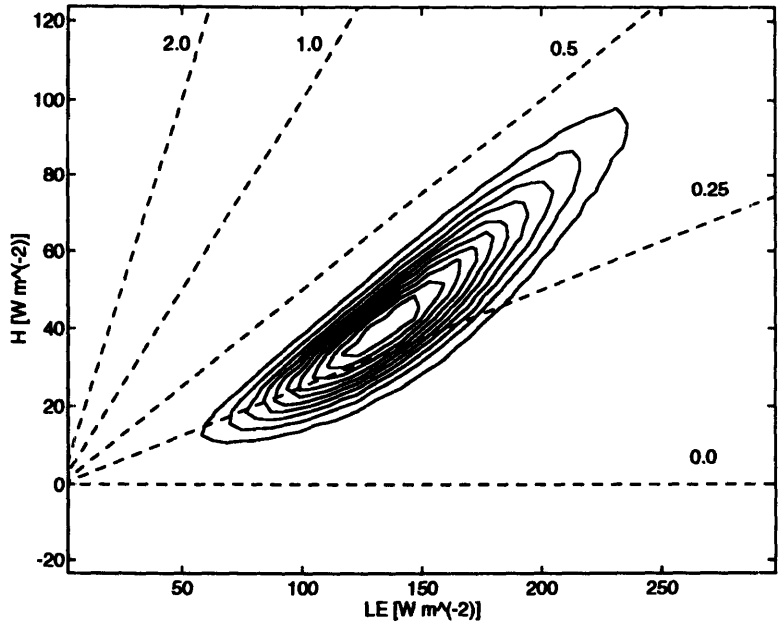

Figure 3-3: Joint probability density function for the surface fluxes of latent and sensible heat in the *Control* model simulation. Lines of constant Bowen ratio are superposed.

Bowen ratio.

The equilibrium Bowen ratio (for moist, homogeneous surfaces with minimal air vapor deficit — the lower limit to evaporation given an amount of available energy at the surface) is proportional to the inverse of the Clausius–Clapeyron relation or γ/Δ (Philip 1987). As the temperature is lowered, the equilibrium Bowen ratio grows rapidly; tabulated values of γ/Δ show a rapid rise for low temperatures (Eagleson 1970). To the equilibrium Bowen ratio we must add the effects of soil-controlled evaporation and departures from equilibrium assumptions. The rapid loss of probability mass along lines of increasing Bowen ratio in Figure 3-3 is consistent with this simple analysis.

The joint probability distribution of sensible and latent heat fluxes is integrated to derive the marginal distributions for the Bowen ratio and evaporative fraction EF, where

$$\mathrm{EF} = \frac{\lambda E}{R_{\mathrm{net}} - G} = \frac{1}{1 + \mathrm{Bo}} \tag{3.8}$$

There is considerable variability in the Bowen ratio and it has a negative skew (Figure 3-4). The evaporative fraction is more peaked due to its mathematical definition in (3.8) and has a positive skew. In this respect, where the Bowen ratio fails to upgrade its status from a diagnostic to a predictive measure due to its larger variability, the

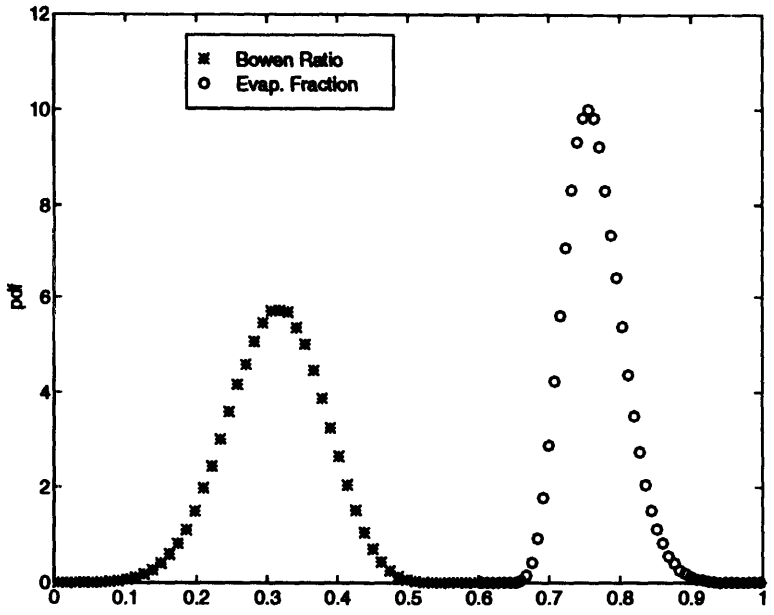

Figure 3-4: Probability density functions for evaporative fraction EF and Bowen ratio Bo in the *Control* model simulation.

evaporative fraction may be capable of limited use in predictive rather than diagnostic mode.

Table 3.2 also includes statistics summarizing the results of experiments in the sensitivity to σ_u, the variance of the random input. Due to the assumption that the random forcing has a gaussian marginal distribution, the variance parameter σ_u may only be increased to the level (with respect to the mean $\overline{U}$) such that negative wind-speeds are probabilistically very infrequent. This condition is satisfied for the sensitivity cases reported in Table 3.2. In the high variance case ($\sigma_u = 2.0$), the standard deviations of the states are increased generally in proportion to the increase in $\sigma_u(+33\%)$. In the low variance case ($\sigma_u = 1$), the standard deviations decrease in proportion to that of the noise. In both the low and high variance cases, the means are virtually unchanged. With respect to the noise forcing, the system appears nearly linear in its first two statistical moments.

However, a linear system would transform a gaussian input to gaussian outputs. The non-zero skewness of some model states arises from nonlinearity and feedbacks in the system. As the level of noise increases, the magnitude of the skewness increases, indicating that the noise is preferentially amplified in the high range of the positively-skewed variables and in the low range of the negatively-skewed variables. For example, skewness of 0.52 for T_g in the high variance case, compared to 0.38 in the control case, is indicative of different physical mechanisms for dissipating heat at different

temperatures. At high temperatures (encountered in the high variance case), the net thermal radiative loss from the soil and air slab system is inefficient in dissipating heat. This is due to the strong coupling of the ground and near-surface air temperatures. The system must achieve even higher temperatures to maintain energy balance. Such contrasts between the different mechanisms for dissipating the radiative forcing at the surface are more clearly identified by analyzing the temporal scales associated with each mechanisms in the context of the serial dependence in the model states.

3.3.3 Serial dependence in the model states

The discussion so far on the probability distribution of the model states and derived states does not address the serial dependence in the fluctuations of these variables. The auto-correlation statistic is used to explore the degree of dependence between a variable at a particular time and its evolved state some time (at lag τ) later. The stochastic model is forced with white-noise that is serially independent. Any serial dependence that may be evident in the model output is strictly due to the internal structure of the model. The most important source of gain in the model (gain defined in terms of a function that transfers fluctuations from one frequency to another in a preferential mode) is the thermal and moisture inertia associated with the size of the heat and water reservoirs at the land surface and in the air slab. The interactions in the model also contribute significantly and in a non-trivial manner to the gain as will be shown below.

Figures 3-5a to 3-5d represent the lagged auto-correlation functions estimated for the four model states. They are strictly a sum of exponential functions due to the Markovian nature of (3.5). To associate an approximate scalar time-scale with each process, we use the functional form of the single-exponential simple-Markovian auto-correlation function $\exp(-\tau/\tau^*)$ where τ^* is now an approximate (but conveniently scalar) measure of memory for the process. The value of the time-scale τ^* is estimated for each function by selecting the e-folding of the decorrelation with increasing lag. The relative soil saturation is characterized by τ^* of 9 days, and it is the most persistent of all model states (Figure 3-5a). The specific humidity in Figure 3-5b has a more rapid decorrelation ($\tau^* = 3$ days) since it is directly affected by the stochastic forcing through the advection term.

The two temperature variables exhibit decorrelation patterns that are indicative of strong influences of land-atmosphere interaction as will be discussed now. In Figure 3-5c, the ground temperature decorrelates very rapidly at first and then reduces its rate

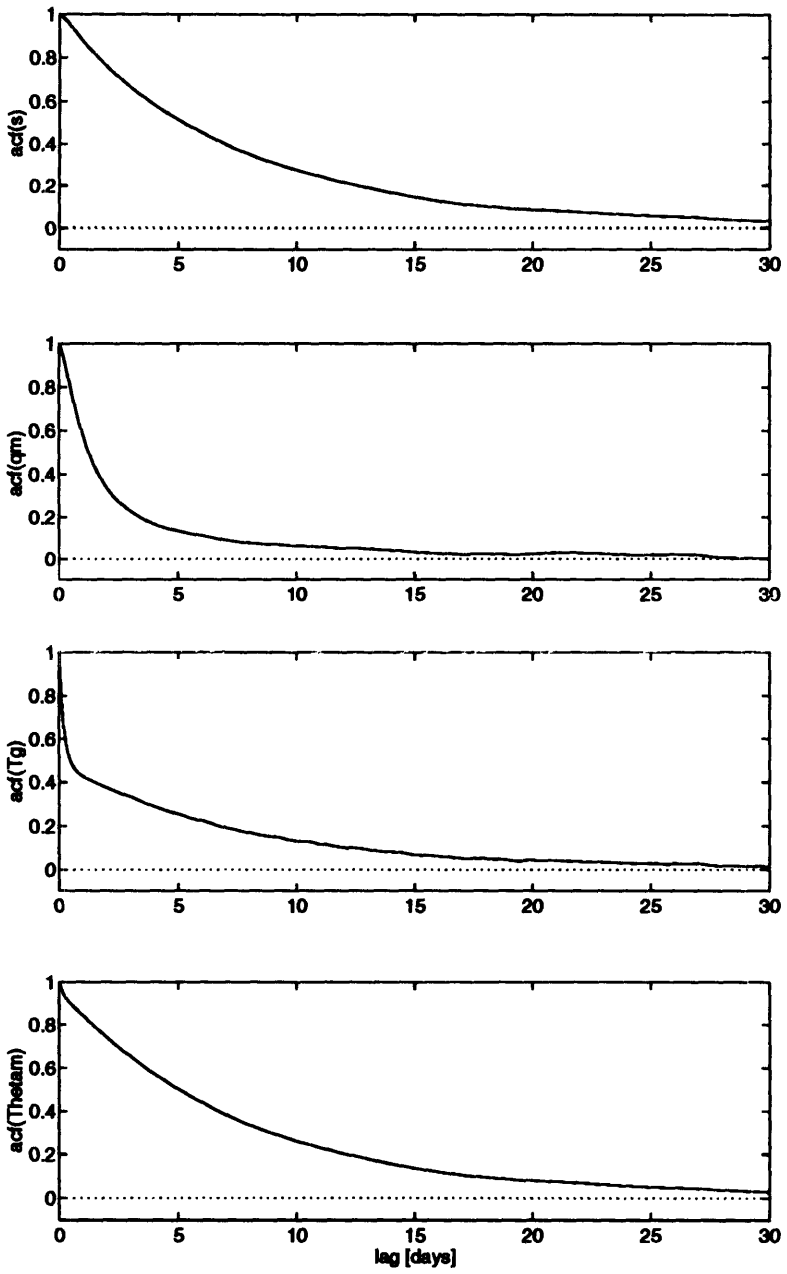

Figure 3-5: Autocorrelation functions for four state variables in the *Control* simulation: (a) relative soil saturation, (b) atmospheric specific humidity, (c) soil temperature, and (d) air potential temperature.

of decorrelation significantly (note the slope of the auto-correlation function near zero-lag). This phenomenon may be explained by considering an anomaly in wind-speed during the stochastic realization. The soil is generally forced by solar radiation, and it dissipates its heat through the turbulent fluxes and longwave radiation. If a warm ground temperature anomaly is established, the temperature difference between the ground and the mixed–layer is likely to be increased as well, enhancing the efficiency of the turbulent sensible heat flux — but only until that flux has worked to restore the nominal or equilibrium temperature *gradient*, not necessarily the equilibrium ground temperature. After that point, the dissipation of heat from the ground occurs mostly through thermal radiation (from the surface to the atmosphere above and from the mixed layer to space), which is a considerably less efficient mechanism with longer time-scales. The dissipation of heat by thermal radiation contains a positive feedback (back radiation from the overlying air) and it thus adds memory to the system. The turbulent heat flux mechanism initially and rapidly dissipates soil temperature anomalies (as evident in the rapid, initial decorrelation of temperature anomalies); nevertheless sensible heat flux is only an atmospheric coupling mechanism for the surface, and the dissipation of heat from the soil-atmosphere system ultimately occurs by thermal radiation which introduces memory and serial dependence in the process. This is evident by the slow decorrelation rates at the larger lags in Figure 3-5c and by $\tau^* = 6$ days for θ_m (Figure 3-5d). This behavior is further apparent in the upcoming discussion of lagged cross-covariances.

The derived states — that is, the fluxes — have small τ^* values; the precipitation, latent heat flux, and sensible heat flux are decorrelated rapidly. If the model were forced by colored noise for its large-scale forcing, some serial dependence would also become evident in these time-series. Delworth and Manabe (1988) find decay time scales on the order of one to two months for the soil moisture state in the Geophysical Fluid Dynamics Laboratory (GFDL) General Circulation Model (GCM). The e-folding found in that model ranges from 1.2 months in the tropics to 1.9 in the mid-latitudes and 2.5 in the polar regions. It should be noted that the total soil water storage capacity in the GFDL GCM is 15 centimeters whereas the model here uses 5 centimeters for the Control case. If we also use a 15 centimeter storage capacity, the model soil moisture serial dependence time-scale is increased to 19 days. The difference is simply due to the serial dependence of the random forcing. The precipitation time-series in the model here is essentially white noise. The GFDL GCM produces strong serial dependence in the precipitation time-series (Delworth and Manabe, 1988). The time-scale of the precipitation process adds to that of the

soil moisture. In fact Delworth and Manabe (1988) perform simple simulations with a dissipative soil moisture model that is forced by white noise precipitation. The time-scale associated with that model for the set of climate conditions roughly similar to those in this study is only 16 days. Wang et al. (1994) analyze a stochastic differential system similar to (3.5) that may be forced by colored-noise and whose properties may be analyzed using the Fokker-Planck equation.

3.3.4 Covariability structure

The stochastic differential equation representing heat and moisture balance for land and near-surface atmosphere with land-atmosphere interaction is forced by noise in its wind-speed fluctuations; any resulting covariability in model states or fluxes is due to the internal structure, feedbacks, and interactions. The degree of covariability and delayed cross-dependence is measured by estimating the lagged cross-covariance of the simulated time-series.

Figure 3-6a is the lagged cross-covariance function for the air specific humidity and potential temperature. For negative lags the specific humidity leads the temperature, and for positive lags the temperature leads humidity. These two states are positively correlated; higher specific humidity values increase the thermal radiative emissivity and absorptivity of the air-mass. The thermal radiative fluxes are affected, and the back-radiation to the surface is increased (the greenhouse effect). To dissipate the increased heating induced by a rise in humidity, the temperature must rise further so that the energy is lost by thermal radiation to space. The statistical signature of this feedback is positive correlation between humidity and temperature anomalies near the same time. The slower decorrelation with humidity leading potential temperature is due to the comparatively longer time–scales of thermal radiation, compared to the faster–response turbulent latent heat flux, which plays a greater role with potential temperature leading humidity: increased air temperature drives an increase in potential evaporation due to the enhanced air vapor deficit; however, the disequilibrium is quickly corrected by the responding increase in evaporation from the soil (if moisture is available).

The positive correlation between soil temperature and air potential temperature (Figure 3-6b) reflects the strong link between the two energy reservoirs. The land surface heats the mixed layer by sensible heat flux and outgoing thermal radiation, following solar heating of the surface. Energy is absorbed in the atmosphere, and an elevated temperature is the only way for the whole system to dissipate energy to space.

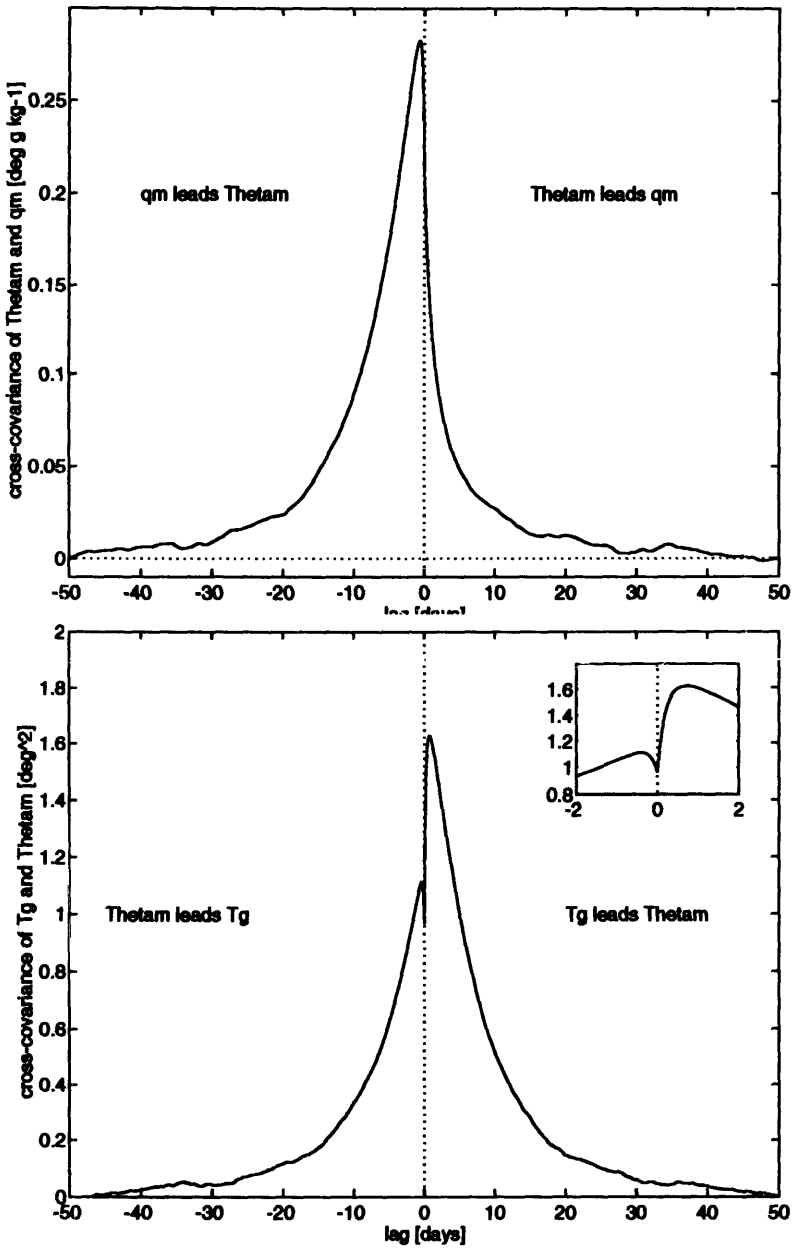

Figure 3-6: Lagged cross-covariances for pairs of state variables in the *Control* simulation: (a) between air specific humidity and potential temperature, and (b) between air potential temperature and soil temperature.

Due to the absorption of thermal radiation in the slab and elevated temperatures being the only effective way of dissipating energy from the system to space, the two land and air temperatures are strongly linked with positive correlation. Figure 3-6b shows the lagged cross-covariance of the two temperature state variables; as argued above, the correlation is generally positive and symmetric, indicative of the strong influence of the thermal radiation feedbacks between the two over a wide range of time scales. At the scale of the fast-response turbulent sensible heat flux, the negative correlation is evident in the sharp valley that is created by this latter mechanism around the origin (lag equal to zero). An anomalous sensible heat flux (due to a wind–speed perturbation) may bring soil temperature below a nominal value, and perturb air temperature above a nominal value. Such opposite-sign anomalies take away from the positive correlation near zero lag; as shown in the inset, the fast–response turbulent heat flux rapidly restores the system from such disequilibrium, returning to high positive correlation in less than one day. On the other hand, the thermal radiation that affects (and couples) both temperatures acts on a longer time-scale, and it is argued that it will induce overall positive correlation between the two variables. In the inset it is also apparent that the maximum correlation between the ground and air temperatures occurs with a lag of nearly 1 day with the ground temperature leading. This is consistent with the results of Chapter 2, where investigations into the role of the diurnal cycle indicate that the land-atmosphere system is forced by solar heating of the surface and the air temperature heating is mostly through the sensible heat flux and absorption of terrestrial outgoing thermal radiation following this surface heating.

3.4 The Role of Feedbacks in Land–Atmosphere Interaction

The lagged cross-covariance between ground temperature and relative soil saturation for the *Control* experiment is plotted in Figure 3-7a. The instantaneous and lagged dependence between the two variables is negative since dry soil anomalies are associated with greater partitioning of the available energy into sensible (rather than latent) heat flux. This turbulent heat flux mechanism is relatively less efficient, the ground temperature rises, and a temperature anomaly of the opposite sign ensues. A similar argument may be made for a positive soil moisture anomaly which instantaneously leads to greater partitioning to latent heat flux (lower Bowen ratio) and an

efficient cooling of the surface. The long memory associated with the soil moisture state (see Figure 3-5a) insures that the influence persists and the soil moisture leading soil temperature decorrelates slowly with lag. Figure 3-7a also shows that the soil temperature leading moisture content is also persistent at large lags due to the influence of the soil temperature on evaporation through the potential evaporation. The saturation vapor pressure at the surface increases sharply with increasing temperature; the enhanced gradient in the near-surface vapor pressure induces elevated potential evaporation rates and enhancement of negative soil moisture anomalies due to the drying.

We now exploit the simple mathematical structure of the model to perform some experiments that will allow us to quantify the effects of feedbacks and land-atmosphere interactions on the statistical signatures of climate variability. In Figure 3-7a, the soil temperature and moisture lagged cross-dependence are presented for the case in which the land-atmosphere coupling in the model is reduced to a one-way interaction in that the feedback mechanisms are severed. This is achieved by evaluating the drift and diffusion coefficients $G(\cdot)$ and $g(\cdot)$ at the mean state of the atmosphere as obtained from the *Control* simulation. The surface still receives the same mean radiative forcing from the atmosphere, but the surface fluxes are not allowed to alter the state of the atmosphere. This is essentially the case of *No–Feedback*.

In Figure 3-7a, it is evident that without land–atmosphere feedback, the covariability between soil temperature and soil moisture is considerably reduced. [In this experiment, the suppression of land–atmosphere feedback is simply represented by the use of the constant stationary mean mixed–layer potential temperature ($\overline{\theta_{\mathrm{m}}}$) instead of $\theta_{\mathrm{m}}(t)$; a very similar result is obtained when $\overline{q_{\mathrm{m}}}$ is used for $q_{\mathrm{m}}(t)$ in addition.] Covariability between soil temperature and soil moisture is critically dependent on the atmospheric energy–balance feedback. When it is not required to respond to changing air temperature, the fast–restoring sensible heat flux can instantaneously dissipate soil temperature anomalies. In addition, in this *No–Feedback* case, downwelling thermal radiation cannot add memory to ground temperature anomalies. Through the effect on potential evaporation, the loss of memory in ground temperature contributes a loss of memory in soil moisture as well; the two-way positive feedback between moisture and temperature anomalies is suppressed. In the *No-Feedback* case (Figure 3-7a), the covariance with s leading is reduced more than with T_{g} leading; the sensible heat flux can instantly dissipate T_{g} anomalies, so that the water balance's influence on T_{g} through $\beta(s)$ and the slowly varying s is not so effective (this is further illustrated by fixing β in an additional simulation at the end of this Section). On the other hand, s

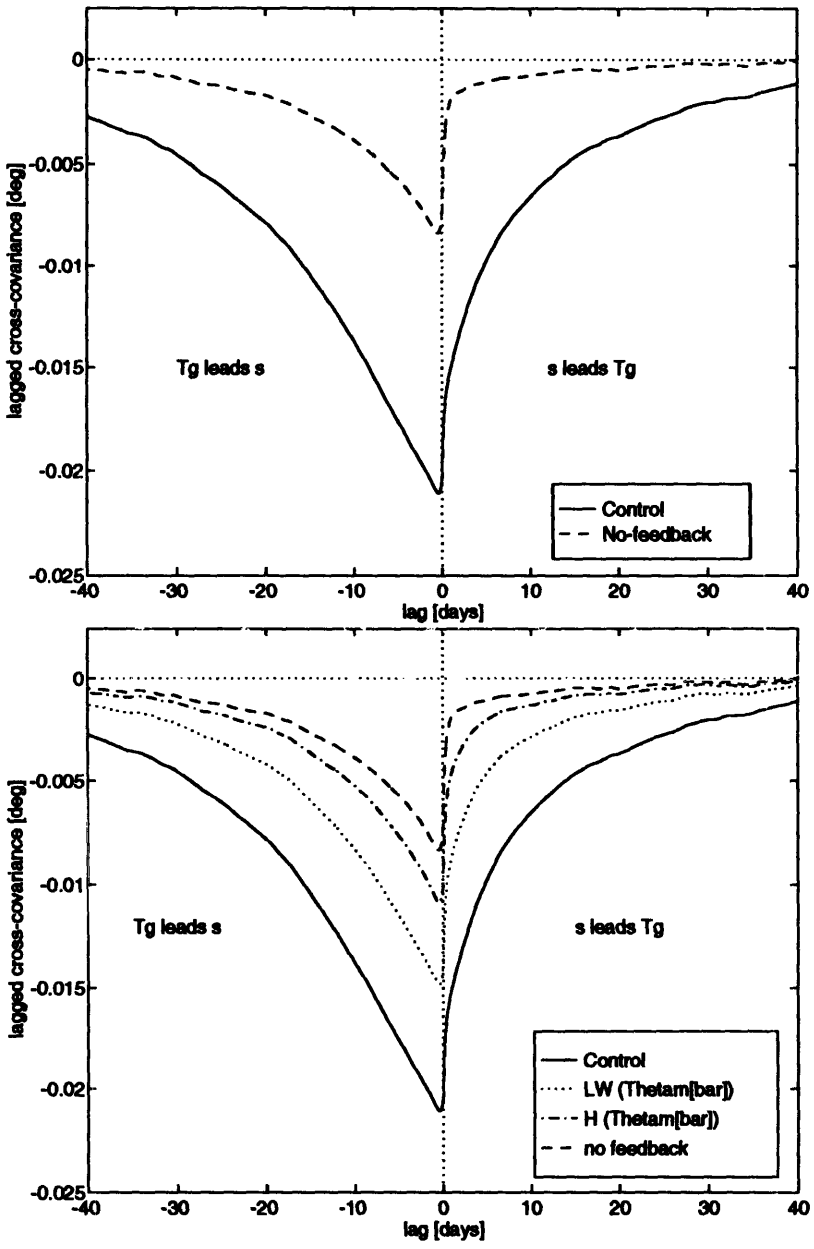

Figure 3-7: Lagged cross-covariances for soil moisture and soil temperature: (a) in the *Control* simulation and the *No–Feedback* case where land-atmosphere interaction is limited, and (b) when the thermal radiation and sensible heat flux are constrained in order to establish the pathways of the feedback.

anomalies retain some persistence due to memory implicit in the water balance alone; the contemporaneous negative correlation in s and T_g anomalies, together with persistence in soil moisture anomalies, results in nonzero lagged covariances when T_g leads s. This simple experiment demonstrates that, in terms of fluctuations and memory, the water–energy linkage *at the soil surface* is established largely via the near–surface atmosphere.

To pinpoint the pathways of these influences, the *No–Feedback* experiment in Figure 3-7a is repeated, but now in going from the *Control* to the *No–Feedback* case (through $\mathbf{G}(\overline{\theta}_m)$ and $\mathbf{g}(\overline{\theta}_m)$), we take smaller steps and differentiate between the role of the two restoring forces in coupling ground and air temperatures. In Figure 3-7b, two intermediary steps are taken; first, the $\overline{\theta}_m$ is used only in the thermal longwave fluxes, and second $\overline{\theta}_m$ is used in only sensible heat. These cases are denoted by $[LW(\overline{\theta}_m)]$ and $[\ H(\overline{\theta}_m)]$. In the first step towards the *No–Feedback* case, the thermal radiative fluxes are not allowed to interact $[LW(\overline{\theta}_m)]$. The lagged cross-covariance is reduced by about 25% but not to the low levels of the *No-Feedback* case. When the turbulent heat flux mechanism is not allowed to be interactive with the atmosphere $[H(\overline{\theta}_m)]$, the lagged cross-covariance is reduced nearly to the *No–Feedback* case. Figures 3-7a and 3-7b are evidence of the importance of land-atmosphere interaction and the two-way coupling of the soil and near-surface atmospheric states in establishing the persistence and covariability of hydrothermal conditions over land.

The most influential factor that controls the degree of soil water balance control on the surface energy balance (as evident in the persistent dependence of soil temperature and moisture with moisture leading temperature anomalies; also evident in the serial auto-dependence of soil temperature) is the partitioning of the available energy into sensible and latent heat flux. The Bowen ratio is functionally dependent on the soil moisture through the evaporation efficiency $\beta(s)$. Figure 3-8a shows the lagged auto-covariance of soil temperature for two situations; first the nominal hydrologic reservoir size Z_h is used as in the *Control* case in Figure 3-5c. The second curve corresponds to the situation when the hydrologic capacity Z_h is doubled. This example shows that the serial dependence of the ground temperature (an energy state) is sensitive to the specification of the hydrologic reservoir. This sensitivity is lost when the evaporation efficiency $\beta(\cdot)$ is evaluated at the fixed mean soil saturation $\overline{s}$, $\beta(\overline{s})$. In this case, the serial dependence of ground temperature as evident in the lagged auto-covariance in Figure 3-8b is identical for both the nominal $1\times$ and $2\times Z_h$ cases. The decorrelation is also much more rapid, since sensible heat flux replaces latent heat flux as the main mechanism to dissipate anomalies. When the latent heat flux is the dominant

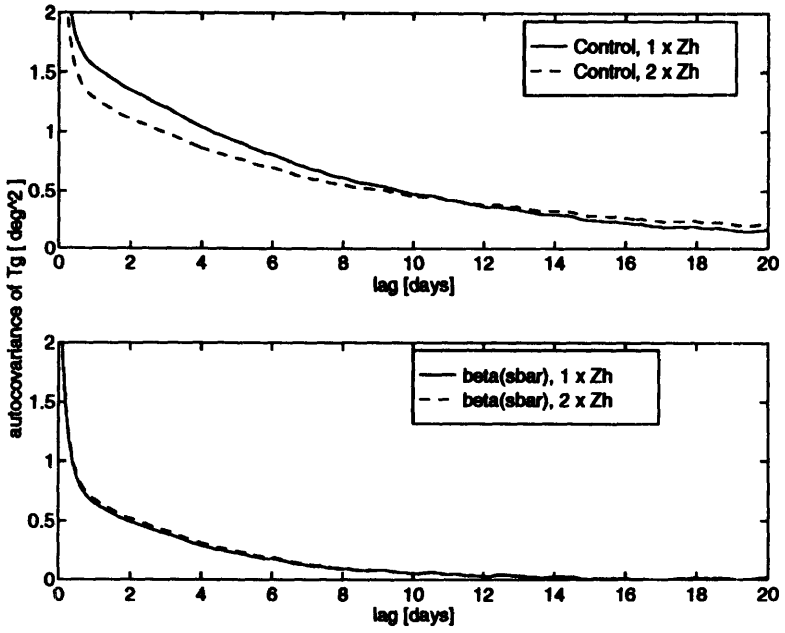

Figure 3-8: Evaporation efficiency communicates variability in soil moisture to soil temperature: (a) the *Control* simulation is subject to doubling of its hydrologic reservoir Z_{h}, (b) simulation with fixed evaporation efficiency $\beta(\bar{s})$, again with nominal and doubled hydrologic reservoir Z_{h}.

mechanism (in terms of controlling the response, not necessarily in magnitude), the dependence of β on the slowly-varying soil moisture adds to the serial dependence in surface energy balance and ground temperature. This experiment indicates that the evaporation efficiency $\beta(\cdot)$ and its role in partitioning the available energy into sensible and latent heat fluxes is the agent through which the soil moisture conditions principally contribute to the variability of soil temperatures.

3.5 Conclusions

The partitioning of atmospheric radiative and precipitation forcing at the land surface into turbulent fluxes and storage defines the regional hydrothermal climate, and it has major influences on the patterns of temporal variability in the system. The feedbacks and interactions that govern these processes are dependent on the heat and moisture states of the soil and the near–surface atmosphere.

Routing white noise through the 4–state stochastic model results in a physically consistent covariability response, including consistent budgets of moisture and heat in land–atmosphere system due to the state–dependent turbulent and radiative fluxes; transmission of ground solar heating to the air by thermal re-radiation; and a thermal radiation feedback (greenhouse effect). The variabilities and covariabilities in the

model's basic and derived states are consistent in that they are borne out of the structure of the interactions and feedbacks. Statistical analyses of these fluctuations are used to identify feedbacks in land-atmosphere interaction. The analytic structure of the model is used to explore these processes in detail and specifically map the pathways of interactions. Experiments in which various feedback mechanisms are suppressed are used to establish the influence of heat and moisture partitioning at the land surface on climatic and hydrologic variability. The suppressed-feedback experiment demonstrates the importance of *two–way* land–atmosphere coupling in establishing memory and covariability of the soil moisture and temperature states.

Due to nonlinearity and feedbacks, the initiation and persistence of perturbations of different type and magnitude depend on what system state the external forcing encounters, not only the sign, magnitude, and persistence of the forcing. The cross-covariance, as used in this Chapter, is a linear measure and does not distinguish between transitions into, or recovery from, different regions of state space. The structure of the model allows the use of both analytical tools and stochastic simulations to explore the temporal behavior of the system.

Chapter 4

Recovery from Anomalies

4.1 Introduction

Meteorologic drought may be broadly defined as a decreased precipitation supply to a region, resulting from reinforcement of large-scale circulation anomalies. The ensuing soil-moisture deficit is termed hydrologic drought; although causally related, the two types of drought are different phenomena having different onset and recovery characteristics (McNab 1989). It has been observed that an end to a meteorologic drought — i.e., a return to normal precipitation patterns — does not immediately or necessarily bring about recovery from the hydrologic drought, partly due to the time lag associated with the moisture reservoirs in surface and subsurface storage zones (Figure 4-1). This Chapter presents and evaluates the hypothesis that the physical interaction between soil water and energy balance contributes significantly to this delay.

If the hydrologic drought (soil moisture deficit) persists and there is a strong coupling of land surface processes and atmospheric conditions, it is then possible that the land-atmosphere interaction forms feedback mechanisms which reinforce meteorological droughts. Large–scale forcing mechanisms that initiate meteorological droughts may thus be reinforced in magnitude and persistence through local interaction with the land surface. This Chapter reports on these local land-atmosphere interaction processes which serve as (positive and negative) feedback mechanisms in climate variability.

The influence of the land surface in reinforcing large-scale induced drought conditions are evident in regions such as the African Sahel and Midwest United States. Nicholson (1986, 1989) argues that land–atmosphere interaction is an important factor

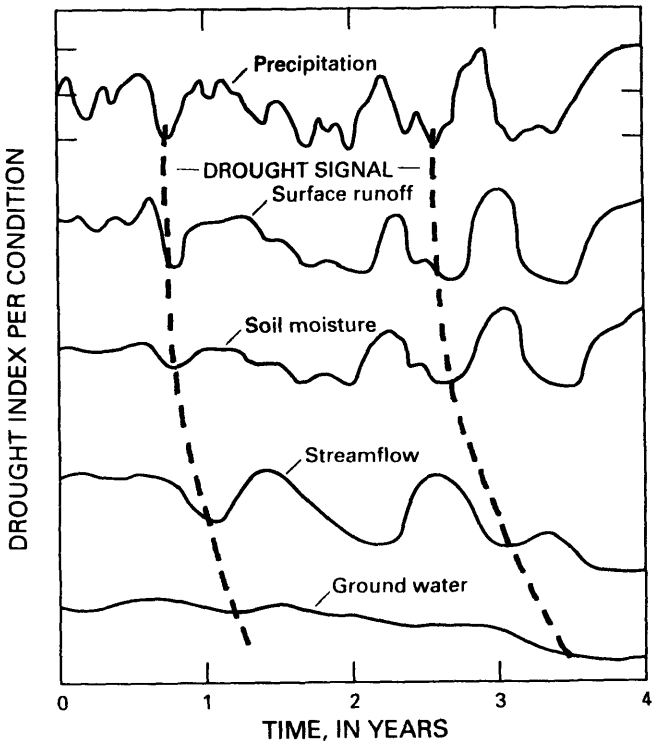

Figure 4-1: Conceptual diagram of how meteorologic drought signal translates to hydrologic drought. After McNab (1989).

in perpetuating drought episodes in the Sahelian region, although the initial drought trigger is probably some change in large-scale atmospheric dynamics. Synoptic observations over the United States (Namias 1988) indicate that large-scale soil moisture deficit may inhibit precipitation because the elevated surface temperature deepens the adiabatically-mixed air layer and intensifies the mid-continental high-pressure ridge. Escape from such reinforced anomaly conditions comes about through a strong external forcing such as disturbances and seasonal shifts in atmospheric general circulation.

Considered alone, the soil moisture state is self-restoring: As the soil matrix over a hillslope becomes moister, less infiltration occurs because the infiltration capacity is generally a decreasing function of soil saturation. More importantly for the soil water balance, the moisture state determines whether evaporation can occur at a rate to satisfy the atmospheric demand. Potential evaporation (E_p) occurs if the soil is sufficiently saturated; otherwise, evaporation proceeds at less than the potential rate. As a result, when the soil is anomalously moist, it both evaporates more efficiently and reduces the infiltration additions to storage. When dry, the soil restricts evaporation and enhances infiltration. These mechanisms work to restore the moisture state from anomalies of either sign toward a stable equilibrium value — a negative feedback.

However, when the *coupled* water-energy system is considered, positive feedbacks are possible. The soil moisture state and the temperature state are negatively correlated due to the deficit in latent heat flux and the corresponding substitution of the less efficient sensible heat flux cooling mechanism. Dry soil tends to be associated with a high surface temperature; high temperature raises E_p, which — depending on the severity of the anomaly — may lead to further drying, or even when precipitation returns, the elevated evaporative demand may exhaust the newly-supplied water before the soil moisture reservoir can be replenished. With high soil temperature, net available energy increases and the potential vapor gradient is increased due to the temperature dependence of saturation specific humidity; in addition a warm surface enhances free convection, which contributes to greater efficiency in turbulent transport.

These positive feedbacks in the linked water and energy budgets at the land surface are *local*, in the sense that they are independent of large-scale persistence. Local positive feedbacks can help to trigger and sustain meteorologic drought by contributing to the establishment of persistent large-scale circulation anomalies, and they can delay recovery from hydrologic drought even when meteorologic drought has ended. Because these potential feedback mechanisms are dependent on the moisture and temperature state of the soil and the atmosphere, a relevant issue concerns whether or not the return to normal conditions is more efficient when in a positive anomaly as opposed to when in a negative anomaly. Droughts are observed to last longer than wet spells over much of the conterminous United States (Diaz 1983). In practical terms, are there feedback mechanisms that delay recovery from droughts and reinforce dry conditions?

4.2 Analytic Approach

This Chapter examines the presence or absence of asymmetries in the recovery time from warm-dry and cool-moist conditions in the physically-based stochastic model of water-energy coupling in land-atmosphere interaction developed in Chapters 2 and 3.

In this Chapter, the stochastic model of Chapter 3 is used to explore the effects of water-energy linkages and land–atmosphere interaction on the dynamics of recovery from soil moisture anomalies, focusing on the state-space first-passage times associated with the system of stochastic differential equations (3.5). The development of feedback mechanisms based on land-atmosphere interaction is presented, and the differences in recovery to normal from dry and moist soil moisture conditions are esti-

mated. The key focus is soil moisture in this application because: 1) the interest is on the role of hydrologic drought in forming local reinforcing mechanisms, and 2) when dealing with multi-dimensional state-space, the analysis of the diagnostics is simpler when the problem is reduced to at most two dimensions. Thus the three other model variables form conditioning states in terms of probability. Any marginal probability distribution must therefore be integrated in all its conditioning states by weighting with the joint probability distribution.

4.3 State-Space First-Passage Times

4.3.1 Definitions

The land-atmosphere interaction model represents the random trajectories of soil moisture $s(t)$, soil temperature $T_g(t)$, mixed-layer specific humidity $q_m(t)$ and potential temperature $\theta_m(t)$ such that their covariances are derived from the linkages in coupled water and energy balances in the soil and the atmosphere. Beginning from an initial state $\mathbf{x}(t=0) = \mathbf{x}_0$, the first-passage time $T_{\mathbf{x}_0 \to \mathcal{B}}$ to excursion over a state-space boundary $\mathcal{B}$ is a random variable whose probability distribution $f_T(T_{\mathbf{x}_0 \to \mathcal{B}})$ is conditional on the initial states. The distribution is also dependent on the internal structure and the physical processes represented in the model. Feedback mechanisms and physical interactions affect the first-passage time distributions.

In the four-variable system of the model, $f_T(T_{\mathbf{x}_0 \to \mathcal{B}}; \mathbf{x})$ is a function of $\mathbf{x}_0 = [s_o\, q_{mo}\, T_{go}\, \theta_{mo}]^T$. Each initial state $\mathbf{x}_0$ exhibits a different distribution of $T_{\mathbf{x}_0 \to \mathcal{B}}$, characterized by moments $T_n, n = 1, \infty$. For the stochastic differential equation (3.5), the n^{th} moment of first-passage time T satisfies the Fokker-Planck Equation in the form,

$$-nT_{n-1}(\mathbf{x}) = \sum_i G_i(\mathbf{x}) \partial_i T_n(\mathbf{x}) + \frac{1}{2} \sum_{ij} \left(\mathbf{g}\mathbf{g}^T\right)_{ij} \partial_i \partial_j T_n(\mathbf{x}) \tag{4.1}$$

subject to the boundary conditions $T_n = 0$ on the passage boundary, and either reflecting, absorbing, or natural domain boundaries (see Gardiner 1985). Entekhabi et al. (1992) analytically solve the first three moments of passage times for a univariate soil moisture system; they then estimate the pdf $f_T(T)$ by fitting the moments to an assigned probability density function. In principle, equation (4.1) can be solved for the four-state system, if not analytically, at least numerically by a relaxation method, for example. Such solution represents a significant computational effort. Furthermore, because the solution to T_{n-1} becomes the right-hand side to the partial

differential equation for T_n, errors would propagate through this cascade of partial differential equations. The result would be very approximate probability density function of first-passage times over $\mathcal{B}$, for every point in the domain. For the current application, a reasonably accurate probability density function of first-passage time for each of a few selected initial states is of more interest. In this study, the complete probability density functions $f_T(T;\mathbf{x})$ are computed by constructing the histograms of the numerical integration of the system.

In this application we narrow our focus on anomalies at the surface and mostly analyze the soil moisture and soil temperature variables ($s(t)$ and $T_g(t)$); the remaining atmospheric variables thus form conditioning probabilities, and the joint probability density function of the model states are used to find the (marginal) probabilistic behavior of the main diagnostics. The excursions are defined in terms of beginning from an anomalous soil moisture state and the first-passage is defined in terms of soil moisture recovery to normal conditions.

Given that the soil moisture state is s_o, how long will it take to reach another state, s_1? The passage boundary $\mathcal{B}$ selected for this study is the median soil moisture, that is, s_{50} such that 50 percent of the stationary probability mass lies above, and 50 percent below, s_{50}. The median is selected rather than the mean or expected value, because the median is a more meaningful measure of "normal" for a skewed distribution. In general, it cannot be assumed that a natural physical variable is gaussian, and in fact the stochastic model solution probability density functions are skewed (Chapter 3).

The quantities of interest are the first-passage time from a soil moisture anomaly in the dry sector ($s \leq s_{50}$) across the average (median) value into the wet sector ($s > s_{50}$), and vice versa. In the four-dimensional state space, the boundary $s = s_1$ has three dimensions; this study is not concerned with the temperatures and air humidity when soil moisture crosses this boundary. The initial-condition anomalies selected are s_{05} and s_{95}, defined by:

$$\begin{aligned} P[s \leq s_{05}] &= 0.05 \\ P[s \leq s_{95}] &= 0.95 \end{aligned} \tag{4.2}$$

That is, in the ergodic sense, the soil moisture state is drier than s_{05} five percent of the time, and moister than s_{95} five percent of the time. These two anomalies are equidistant from the median s_{50} in a probabilistic sense.

In the 4-variable model, s_o is associated with a distribution of the other three

states (q_m, T_g, θ_m). The distribution of the other three variables, conditional on a given s_o, is given the notation,

$$p\left(q_{mo}, T_{go}, \theta_{mo} \,|s_o\right). \tag{4.3}$$

4.3.2 Passage–time solution technique

With $(s_n, q_{mo}, T_{go}, \theta_{mo}), n = 05(95)$ as the initial condition, the equations are integrated in time until the value of s is greater (less) than the crossing value s_{50}; the time to crossing $T_{s_n \to s_{50}}$ is recorded; the system is restarted at the same physical initial condition repeatedly to construct a probability density function of T corresponding to that initial condition,

$$f_T\left[T_{s_n \to s_{50}}; q_{mo}, T_{go}, \theta_{mo}\right]. \tag{4.4}$$

The procedure is repeated, varying q_{mo}, T_{go}, and θ_{mo}. The overall probability density function of first passage time from s_n to s_{50} is a probability-weighted average of the individual probability density functions, using (4.3) and (4.4):

$$f_T\left[T_{s_n \to s_{50}}\right] = \iiint f_T\left[T_{s_n \to s_{50}}; q_{mo}, T_{go}, \theta_{mo}\right] p\left(q_{mo}, T_{go}, \theta_{mo} \,|s_n\right) \, dq_{mo} \, dT_{go} \, d\theta_{mo}. \tag{4.5}$$

The resulting probability density function is summed to give the cumulative density function of first-passage time from s_n to s_{50}, $F_T\left(T_{s_n \to s_{50}}\right)$.

4.4 *Control* Solution

The *Control* solution refers to the stochastic solution to the model as presented in Chapter 3. The marginal probability density function of s in the *Control* solution is shown in Figure 4-2. The percentiles s_{05}, s_{50} and s_{95} are indicated with dashed lines. In addition, the stationary expectation (mean) of s is indicated with a dotted line. As indicated by the skewness coefficient of -0.28, the mean lies below the mode; the dry tail is slightly longer than the moist tail.

In the *Control* solution, there is little difference between the cumulative density functions of first-passage time from the moist and the dry anomaly to what is considered to be the normal soil moisture condition (Figure 4-3). The median passage time is about 7.5 days. Fast recovery is fairly likely; for example, there is a 10 percent probability that soil moisture will go from s_{05} to above-average, or from s_{95} to below-average, in under 2.5 days. There is only a 5 percent probability of the mois-

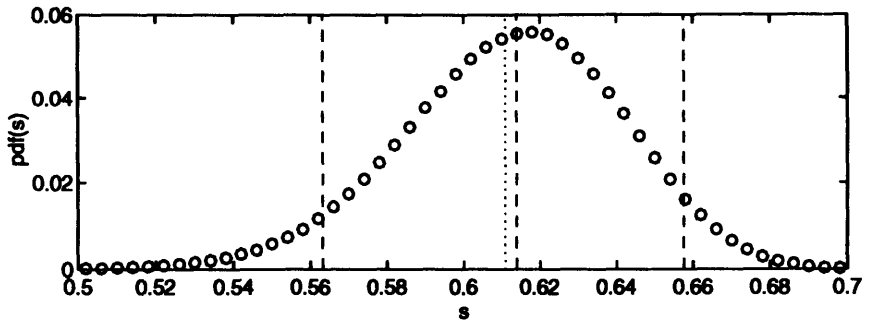

Figure 4-2: The probability density function for soil moisture in the *Control* numerical solution. The percentiles s_{05}, s_{50} and s_{95} are indicated by dashed lines and the mean by a dotted line.

ture remaining in either the dry or the moist sector longer than 25 days, given the corresponding initial 5-percent anomaly.

Because the s distribution is skewed, the anomalies s_{05} and s_{95} are not equidistant (equal volumetric moisture deficit) from s_{50}. The first-passage time analysis is repeated, this time with the soil-moisture midpoint, $s_m = (s_{05} + s_{95})/2$ as the passage boundary. The advantage of using this (mid-point) definition of the normal state instead of the statistical median is that from either anomaly state (s_{05} or s_{95}), it takes the exchange of the same volume of water to recover to normal conditions.

The cdfs for passage times from the s anomalies to s_m appear in Figure 4-4. The first-passage times past this definition of normal conditions are again comparable in distribution. The recovery from dry anomaly is slightly faster. The median recovery time is about 8 days from the moist anomaly and 7 days from the dry anomaly.

The general time scale of about ten days in Figures 4-3 and 4-4 corresponds to local physical processes and land-atmosphere interaction at the regional scale. In essence, this time scale represents the response of the local feedback and recovery mechanisms. Any further interaction with the larger-scale atmospheric general circulation can modify the time scale of recovery from anomalies.

There are two key components of the model that directly affect the first-passage times in Figures 4-3 and 4-4. The depth of the hydrologically active soil layer strongly influences the absolute magnitude of these passage times. The volume of water required will contribute to the determination of the recovery time given the average net exchange at the land surface. In this case, the hydrologically active depth is taken to be 20 cm, corresponding to the penetration depth of storm and interstorm moisture waves.

The other key factor that determines the first-passage times and the relative sym-

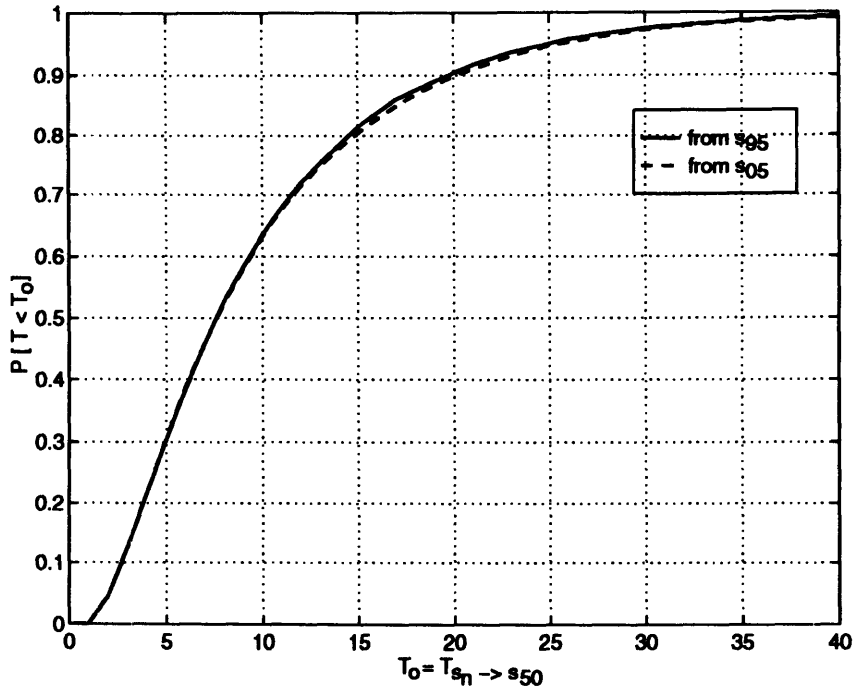

Figure 4-3: Cumulative density function of first-passage times over the median soil moisture, starting from s_{95} and s_{05} in the *Control* solution.

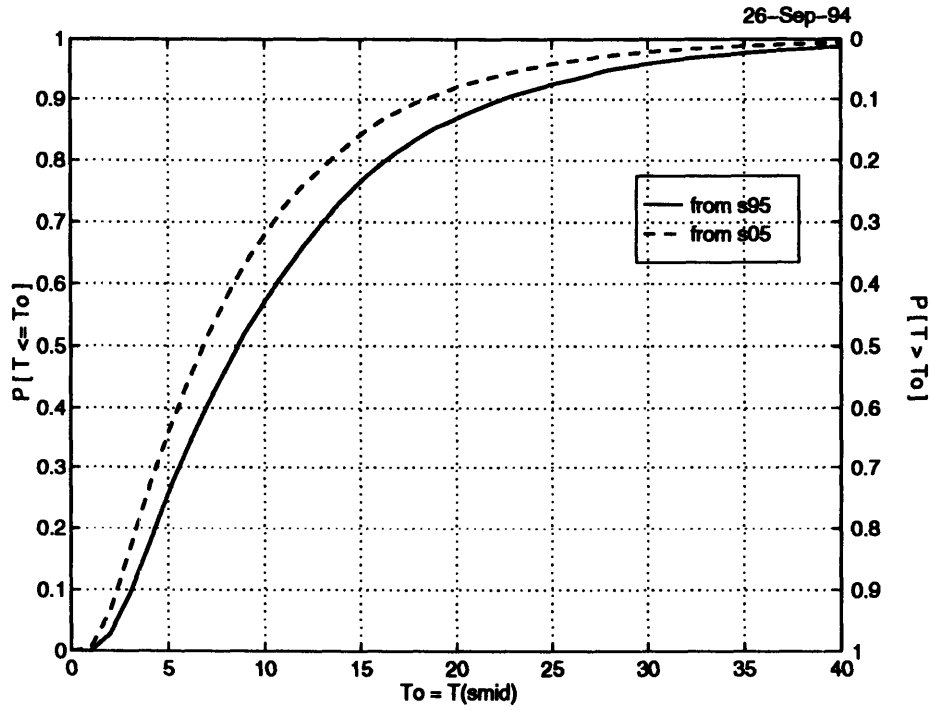

Figure 4-4: Cumulative density function of first-passage times from s_{95} and s_{05} over their soil moisture midpoint, $s_{\text{mid}} = (s_{95} + s_{05})/2$, in the *Control* solution.

metry of recovery from moist and dry anomalies is the shape of the evaporation efficiency function $\beta(s)$. Chapter 3 identifies the central role played by this factor in determining the covariability statistics of the land-atmosphere interaction model. The *Control* solution uses a simple $\beta(s) = s^c$ which for the value of $c = 1$ used yields a linear functional dependence on soil moisture, monotonically increasing from zero at $s = 0$ to unity at soil saturation.

The actual evaporation process is considerably more complex. One of the complexities is due to the fact that the regional evaporation switches between atmosphere-controlled (energy-limited) to soil-controlled regimes. When the soil is adequately wet, available energy limits evaporation. In this case the actual evaporation equals the potential value. When the soil exfiltration rate limits moisture flow below the potential evaporation possible given the amount of available energy, then the evaporation falls in the soil-controlled regime and $\beta(s)$ represents a strong penalty. To explore this important complexity (and nonlinearity) in land-atmosphere interaction, a second set of simulations are performed with a two-regime formulation for $\beta(s)$. Comparisons of the first-passage times from these simulations are then compared with the *Control* solutions to isolate the influence of evaporation efficiency formulation on the problem.

4.5 *Two-Regime-β* Solution

In the *Control* solution, evaporation is never under atmospheric control (i.e., never equal to the potential rate), because β is equal to unity only when the soil is saturated. While the monotonically-increasing β succeeds in linking the heat and moisture balances, it does not succeed in mimicking the physical reality of the switch between soil-controlled and atmosphere-controlled evaporation. Evaporation is under atmospheric control when the soil moisture is capable of exfiltrating water at least equal to the atmospheric evaporative demand; in this case, evaporation is at its potential rate. Under soil control, evaporation is limited because the rate of exfiltration from the soil is constrained by the reduced conductivity of the unsaturated soil. To investigate the system behavior when two distinct evaporative regimes exist, a *Two-regime-β* function was constructed as shown in Figure 4-5. The purpose of this analysis is to test the recovery of the regional soil moisture and energy states when there is a significant difference in the slope of the evaporation efficiency $\beta(s)$ at anomalous states. The slope of the evaporation efficiency β on soil saturation is a strong determinant of the degree of coupling between the water and energy balances at the land surface. Design

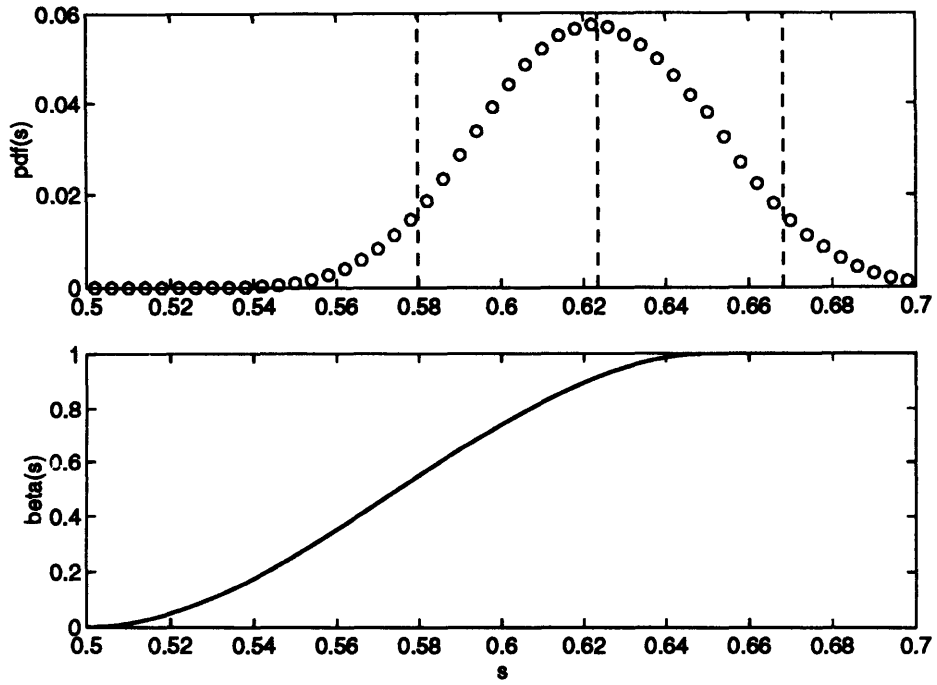

Figure 4-5: The probability density function for the *Two-regime-β* solution (the percentiles s_{05}, s_{50} and s_{95} are indicated with dashed lines) and the constructed two-regime evaporation efficiency function ($\beta(s)$).

of the functional form of β here is thus strictly aimed at *illustrating a physical process.* Application of this land–atmosphere interaction model to a particular location requires a β formulation (and other model parameters) that takes into detailed account the regional soil type, vegetation characteristics, large–scale forcing, and other important factors.

The stationary distribution of soil moisture for the stochastic solution of the new system is shown in Figure 4-5, with the percentiles indicated. The dry-anomaly soil moisture state (s_{05}) lies in the soil-controlled evaporation regime and the moist anomaly (s_{95}) in the atmospheric-controlled regime.

The cumulative density functions of $T_{sn \to s50}$ for the *Two-regime-β* system are plotted in Figure 4-6. For this case the definition of the normal soil moisture condition is fortuitously identical for s_{50} and s_m; this facilitates comparisons. There are significant differences in the two first-passage time distributions and, in addition, there is strong asymmetry in the recovery from the dry and moist anomalies. Whereas the *Control* solution with the simple $\beta(s)$ showed no major difference in the recovery times from the dry and moist anomalies, when the evaporation efficiency representation includes the switch from atmosphere control to soil control, the first-passage distributions are

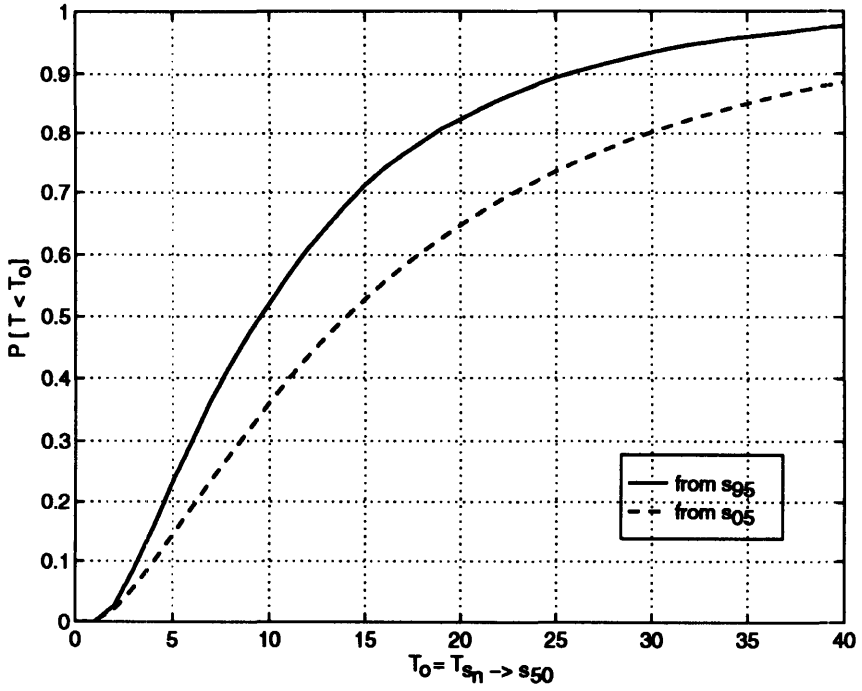

Figure 4-6: The cumulative density function of first-passage time from s_{95} and s_{05} over the median soil moisture in the *Two-regime-β* solution.

markedly different. The median first-passage time in recovering from a moist anomaly to normal conditions is about 10 days. Recovery to similar normal conditions from a (probabilistically and volumetrically) dry initial state takes about 14 days. Recovery times of as long as several tens of days are possible for this system, especially from the dry anomaly.

The slope of the evaporation efficiency function on soil moisture is a key determinant of the strength of the coupling of the water and energy balance at the surface. Chapter 3 demonstrates the influence of this function on the covariance between the soil moisture and soil temperature states, and that the sensitivity of the land-atmosphere interaction to hydrologic variables is modulated by the dependence of the evaporation efficiency on soil moisture.

As mentioned in the introduction, the water balance equation alone produces a negative feedback for anomalies of soil moisture. Moist soil moisture anomalies are rapidly depleted by increased evaporation and reduced infiltration. On the other hand, dry conditions are restored to normal by reduced evaporation and increased infiltration. When the energy balance is coupled to the water balance, the possibility of positive feedbacks develops. In dry-warm anomalies, the potential evaporation increases sharply, which induces even greater drying. Similarly in cool-moist conditions

the potential evaporation is lower and the moist anomaly may persist. The strength of the water and energy balance coupling is through the evaporation efficiency function $\beta(s)$. Thus the influence of the positive feedback that reinforces anomalies of a sign and forces them to persist (increased first-passage times) is dependent on the form of the function $\beta(s)$.

In the *Two-regime-β* solution, the degree of sensitivity of the energy balance to soil moisture availability and hydrologic processes is markedly different for the dry anomaly than for the moist anomaly. Figure 4-5 shows that in the moist anomaly the evaporation rate is energy-limited and thus atmosphere-controlled. The energy balance sensitivity to soil moisture availability is minimal, and the water and energy balances are only weakly coupled. Thus the positive feedback influences of the energy balance on a soil moisture anomaly are not present.

The opposite is true for the dry anomaly. The strong dependence of the evaporation efficiency on soil moisture in this soil-controlled evaporation regime region means that the water and energy balances are closely coupled and that the positive feedback mechanism associated with the soil temperature is active for soil moisture. The presence of the strong coupling of the water balance to the energy balance in the dry anomaly state, and the lack of it in the moist anomaly state, yields different degrees of the positive feedback influence on soil moisture anomalies at each sign anomaly. Because the dry anomaly is affected by this factor that leads to persistence and intensification, the first-passage times are considerably longer for recovery from dry conditions as opposed to moist conditions. Asymmetry in recovery times is the result of this unequal coupling of the water and energy balances at dry and moist anomaly conditions.

4.6 Evolution of Anomalous States

Recovery or any movement in the state-space occurs due to the local deterministic drift $\mathbf{G}(\mathbf{x}_t)$, which ultimately drives the system towards an equilibrium state $\mathbf{x}^\star$, and due to the stochastic fluctuations in the random forcing variable, which affects the states in proportion to the diffusion function $\mathbf{g}(\mathbf{x}_t)$. The two functions derive their functional form and dependencies from the radiative and turbulent fluxes that link the coupled water and energy balance in the soil and the atmospheric mixed-layer. By mapping the values of the drift and diffusion functions at different portions of the state-space, we find the deterministic and noise-induced factors that underlie the first-passage times behavior at the dry and moist anomaly initial states.

Because the solar energy forcing at the top of the atmosphere is invariant in these applications (neither seasonal nor diurnal cycle is included), the independent variable time does not appear explicitly in the drift and diffusion functions. The deterministic contribution to time evolution $\mathbf{G}(\mathbf{x})$ and the modulation of the noise $\mathbf{g}(\mathbf{x})$ are functions of the system state alone and can be plotted in state–space as phase plane portraits.

In this application we again focus on the two soil state variables: soil moisture and soil temperature. This allows visual inspection of the two-dimensional state-space. Again the conditioning on the two remaining (atmospheric) state variables is removed by integrating over the joint probability distribution.

4.6.1 Drift

The coupled evolution of the soil moisture and soil temperature states are plotted in (s, T_g) space. Figure 4-7 is the (s, T_g) phase-plane portrait for the *Control* solution, and Figure 4-8 for the *Two-regime-β* solution. In these figures, the horizontal (s) component of each vector is the deterministic drift of soil moisture (water balance equation), given that the system is at that (s, T_g) point; the vertical component is the deterministic drift of soil temperature (energy balance equation) at that point. This vector represents the instantaneous direction and magnitude of the system trajectory in the (s, T_g) plane. As a four-equation system, the model trajectory actually lies in the 4-dimensional hyperplane. These figures constitute weighted-average phase-plane portraits of the drift part of the system; the other two (atmospheric) variables are accounted for in these figures by integrating over the joint probability density function. Thus, the vector components G_1 and G_3 as plotted for each (s, T_g) are the expected value of each component over all possible q_m and θ_m, conditional on s and T_g, according to the stationary joint probability density of the system.

In Figures 4-7 and 4-8, the G_1 component gives the effect of the mean (without noise) wind–speed forcing, solar radiation, and the system state on soil moisture evolution whereas the G_3 component of the vector gives the effect of system state and mean forcing on soil temperature. [For visual and interpretive reasons, vectors are not plotted for (s, T_g) pairs having stationary probability less than a negigible value.] Also indicated are the equilibrium values $s^\star$ and $T_g^\star$, corresponding to the solution that the system would reach in the absence of noise, such that $\mathbf{G}(\mathbf{x}^\star) = \mathbf{0}$. The equilibrium solution $\mathbf{x}^\star$ is at the intersection of the dotted lines in Figures 4-7 and 4-8.

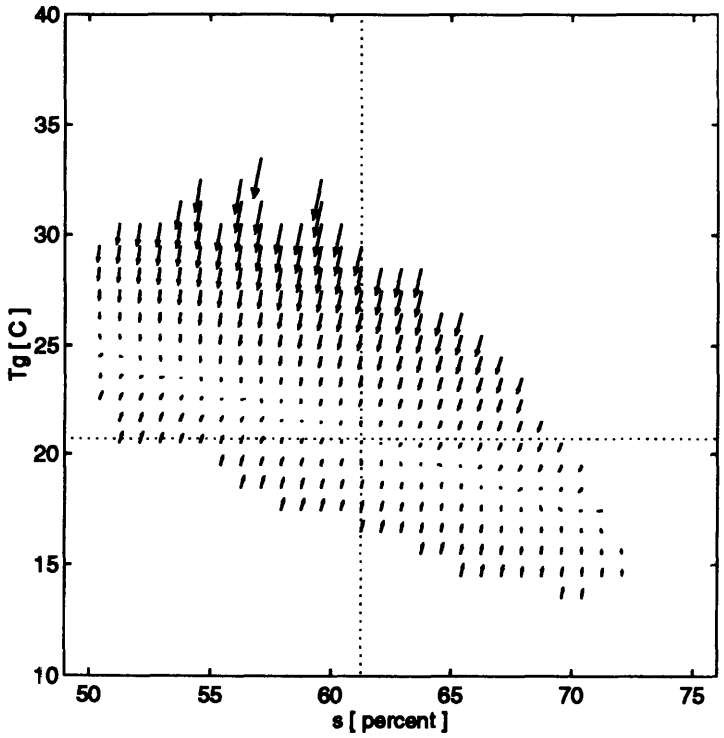

Figure 4-7: Vector plot of the deterministic contribution to (s, T_g) evolution in the *Control* solution. The drift vector components G_1 and G_3 are averaged over the other two state variables.

The point $(s^\star, T_g^\star)$ is a stable improper node. All system trajectories lead to the node, indicating that it is stable. This stability results from self–restoring (negative feedback) mechanisms in all the state variables. [Hasselmann (1976) showed that without such stabilizing (negative) feedbacks in the drift term, the system's variance would grow without bound, analogous with "the continuous, unbounded dispersion of particles in Brownian motion."]

The trajectories in Figure 4-7 are tangent to a line of negative slope T_g vs. s, making $(s^\star, T_g^\star)$ an improper node. Indeed, evolution *toward* this tangent line is stronger than *along* the line toward the node, as evident by the relative length of the vectors. Of particular interest are the vectors in the warm dry quadrant having a leftward (negative ds or drying) component. If the soil moisture is considered as a self-restoring state, then G_1 should be positive (increasing s) whenever s lies below its equilibrium value. However, when the temperature is high, the evaporative demand may overwhelm the self-restoring mechanisms and cause a dry anomaly to dry further before being moistened again. This is a positive feedback in soil moisture anomalies, brought about by the link to soil temperature through potential evaporation. A parallel positive s feedback occurs in the cool–moist sector of Figures

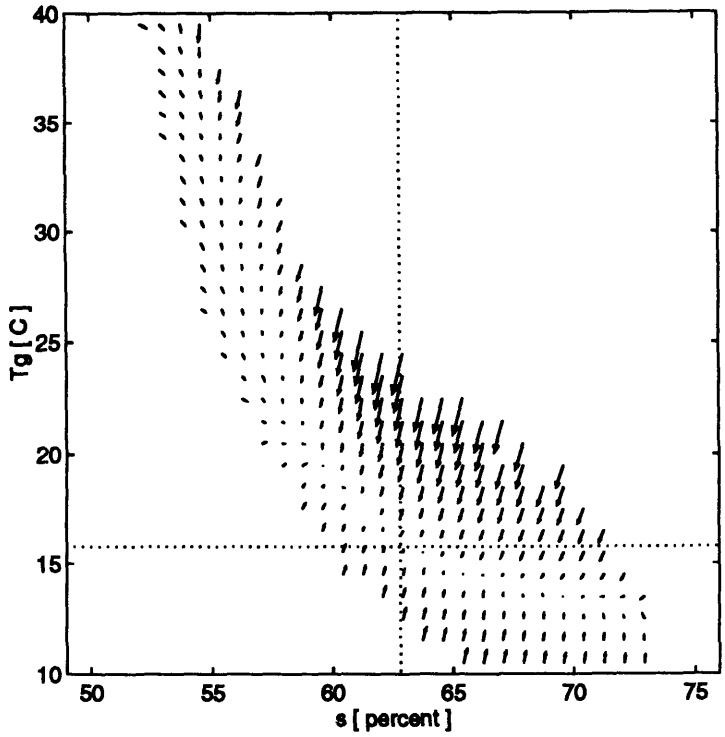

Figure 4-8: Vector plot of the deterministic contribution to (s, T_g) evolution in the *Two-regime-β* solution. The drift vector components G_1 and G_3 are averaged over the other two state variables.

4-7 and 4-8 as well, but as the size of the arrows indicates, it is not as strong as in the warm–dry sector. The positive feedback influence on soil moisture is due to the soil–temperature dependence of saturation specific humidity in surface evaporation; therefore, the positive feedback is stronger at the dry anomaly (versus the wet) because dry anomalies tend to be accompanied by above–average temperatures, which affect the saturated specific humidity, a key component in forming the positive feedback. The thermodynamic Clausius Clapeyron relationship for the temperature dependence of saturation specific humidity has exponentially–increasing slopes with temperature. Although these anomaly-enhancing components are quite small, their very presence demonstrates the competing demands that the water and energy budgets place upon evaporation: evaporation cools and dries, but the system is most often in a state that needs to either cool and moisten, or warm and dry. -1z In the *Two-regime-β* solution (Figure 4-8), the mean (s, T_g) evolution tends toward a curve, rather than a line, through the equilibrum solution. As in the *Control* solution, for a given $s < s^*$, when T_g lies above this curve, a slight positive feedback in s exists, drying an already dry anomaly. Likewise, when T_g lies below this curve for a moist anomaly $s > s^*$, a slight positive moistening effect exists.

Because the (G_1, G_3) vectors are plotted only for (s, T_g) pairs of non-negligible stationary probability, the shape that they define reflects the degree of correlation between s and T_g. The most striking difference between the *Control* and *Two-regime-β* figures is the two-lobed structure of the (s, T_g) joint probability in the latter case. The two variables are more strongly negatively correlated when evaporation is under soil control ($s < 0.65$), and only slightly negatively correlated when the soil does not control evaporation. The *Control* solution also shows negative correlation between the two variables, but in that case the magnitude of the correlation is consistent across the different sectors of state space, due to the linear form of $\beta(s)$.

Can the deterministic drift alone explain the probability distributions of first-passage time? The *Control* system is next integrated in time, without noise, from the anomalous initial states. For the initial state $s = s_n$, the other three variables must also be specified. The solid-line trajectory in Figure 4-9a starts from s_{05} and the expected values of q_m, T_g, and θ_m, conditional on $s = s_{05}$. The dot-dash line starts from s_{95} and the corresponding conditional expectations of the other three states. In this state-space depiction of system evolution, a time scale is indicated by three open circles at 2-day intervals along the beginning of each trajectory. The asterisk indicates 25 days. An additional trajectory (Figure 4-9b) starts from s_{05} and a higher T_g, 5 degrees greater than the conditional expected value of T_g; the remaining two variables are set at their expected values conditional on s_{05} and the higher T_g. Presumably, a higher initial T_g should enhance the positive feedback; this positive feedback is evident in the transient greater excursion of the trajectory away from s equilibrium.

Figure 4-9 shows that — even with an extreme initial value of T_g in the dry case — the deterministic return to equilibrium takes about the same time from each sign anomaly in the *Control* case. Interestingly, the equilibrium s^* lies slightly closer to s_{95}, indicating that recovery from the dry anomaly is actually *faster* than from the moist one, covering a slightly greater Δs in the same amount of time. In Figure 4-9c, the time-series plot of the deterministic trajectory of $(T_g - \theta_m)$ is an interesting diagnostic; it shows that from any of the three initial anomalous states, the two temperatures quickly adjust (primarily by sensible heat exchange) to the equilibrium value of $(T_g - \theta_m)$ and then evolve to their equilibrium values in parallel. This creates the (s, T_g) asymptote visible in Figure 4-7. Once on that asymptote, both s and T_g restore toward equilibrium exponentially. The recovery from anomalies is thus strongly influenced by an initial (and rapid) restoration of an equilibrium temperature gradient $(T_g - \theta_m)$ and then a relatively slower approach to $\mathbf{x}^*$. The fact that a non-vanishing gradient exists between the soil and atmosphere temperatures is due to the

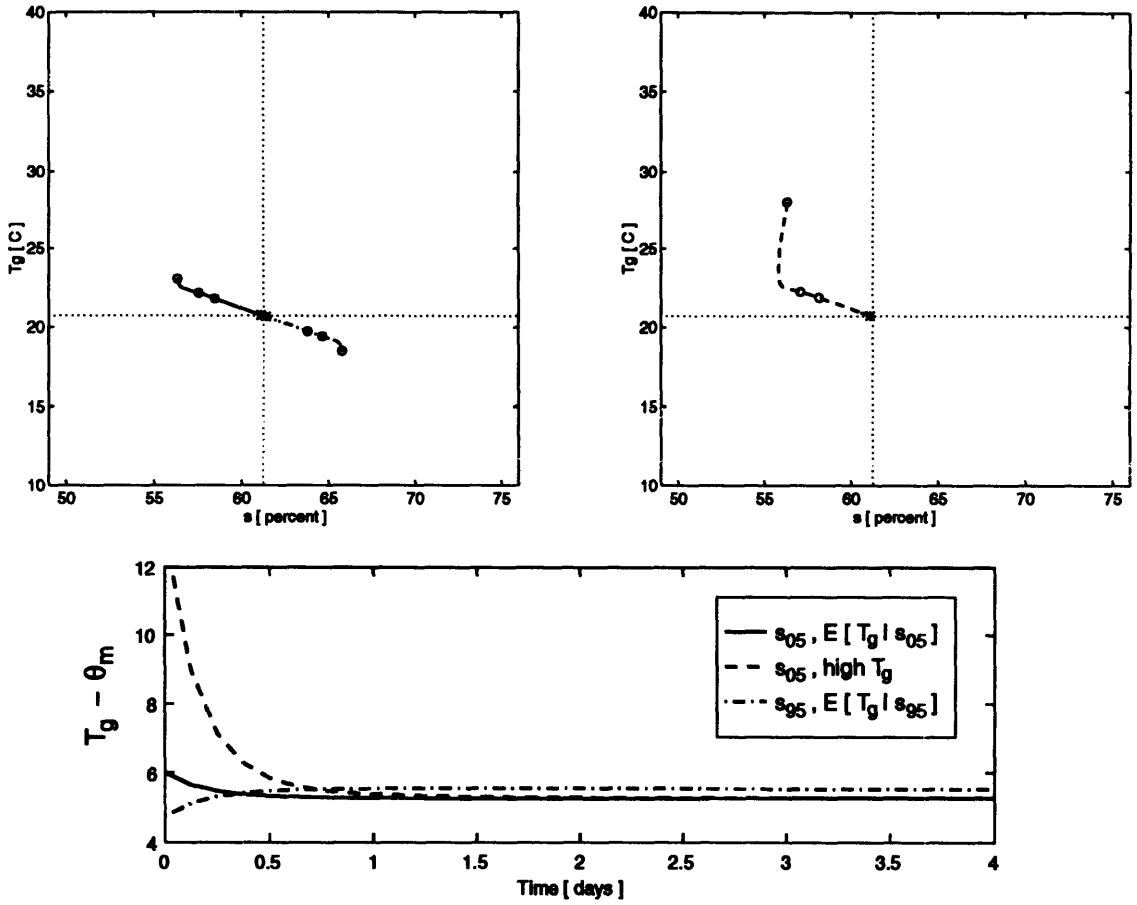

Figure 4-9: Deterministic (no noise) state-space trajectories from s_{05} and s_{95} to equilibrium in the *Control* model. At the bottom is a time-series of the difference between soil and mixed-layer temperature corresponding to each trajectory in the state-space plot.

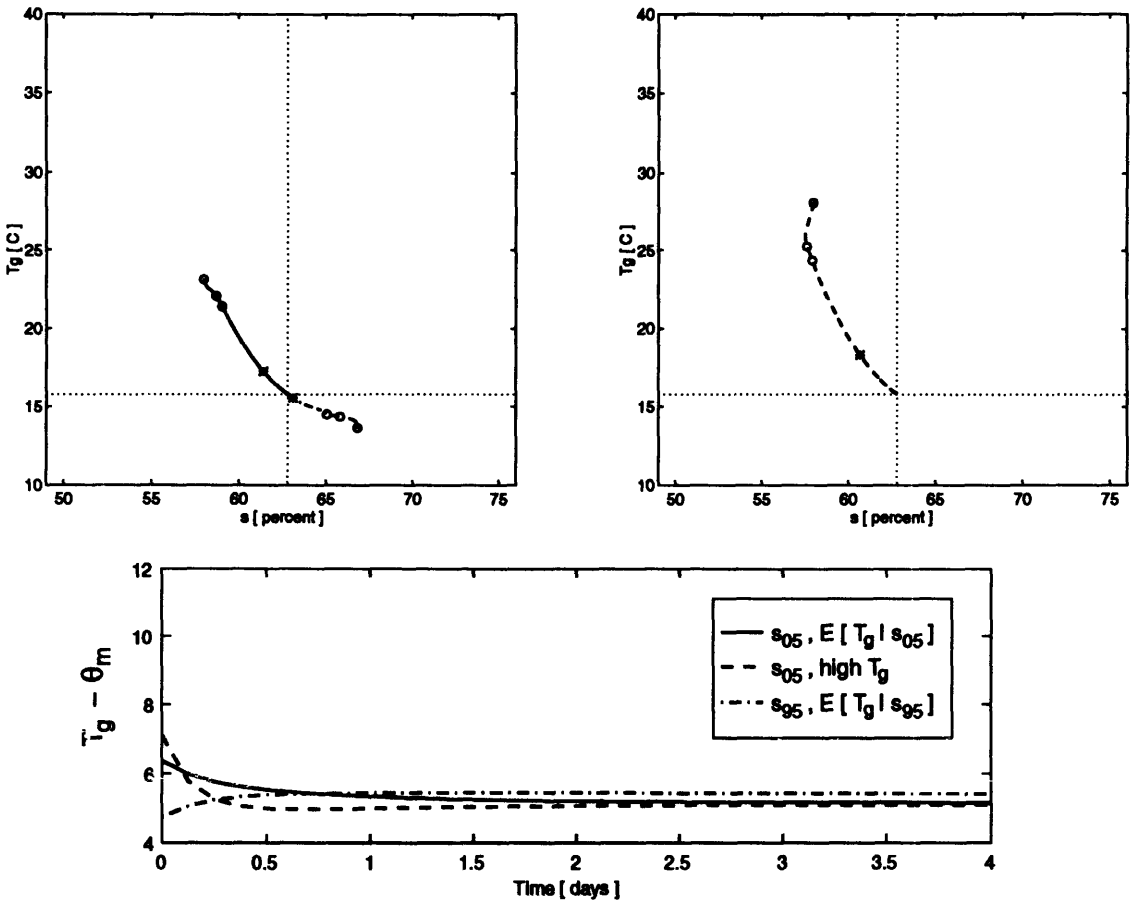

Figure 4-10: Deterministic (no noise) state-space trajectories from s_{05} and s_{95} to equilibrium in the *Two-regime-β* model. At the bottom is a time-series of the difference between soil and mixed-layer temperature corresponding to each trajectory in the state-space plot.

competing effects of solar radiation forcing a positive difference with the soil heating to be warmer than the atmosphere. Sensible and latent heat flux as well as net thermal radiative exchange then work to dissipate this gradient. Because all four state variables are linked, an equilibrium temperature gradient ($T_g - \theta_m$) develops which, in the long-term, balances radiative exchange at top of the atmospheric boundary. Heat advection (latent and sensible), as well as entrainment, also contributes to this balance, yet in terms of magnitude the vertical radiative exchanges dominate in the energy balance.

The *Two-regime-β* deterministic recoveries from selected anomalies are shown in Figures 4-10a and 4-10b. The initial states for each anomaly were constructed as for the *Control* solution, and time is again indicated in the state-space plot with open circles every two days for the first 6 days, and an asterisk at 25 days. Again,

the time series of $(T_g - \theta_m)$ (Figure 4-10c) shows that, from any of the three initial points, the system quickly ($\approx$ 1 day) equilibrates first to an equilibrium temperature gradient and maintains that difference as the two temperatures return in parallel to their equilibrium values.

Due to deterministic drift alone, the recovery from a moist and a dry anomaly to equilibrium is symmetric in the *Control* solution, and asymmetric in the *Two-regime-β* case. In the latter case, it appears that the system recovers more quickly from the moist anomaly because of the shape of the (s, T_g) distribution; although the s distance to $s^\star$ is about the same for both the dry and warm anomaly, the system actually has farther to travel from the dry side, because temperature is more disequilibrated than on the moist side. The need to recover from a greater T_g anomaly (Figure 4-10b) delays the recovery from a dry s anomaly because the increased evaporative demand creates a positive soil-moisture feedback. Reciprocally, soil moisture control of evaporation slows T_g recovery in this sector, so the temperature and moisture states are mutually inhibiting one another's recovery toward equilibrium. In the *Control* case, this inhibition exists nearly equally on both sides.

The positive feedback mechanism in the dry soil moisture anomaly is evident in Figures 4-9b and 4-10b. The water balance forms (in a strict sense) a negative feedback for soil moisture anomalies because the dependence of the hydrologic fluxes on soil moisture is such that a negative soil moisture anomaly necessarily moves (in its deterministic drift component) towards the equilibrium, and a positive anomaly is reduced by the hydrologic fluxes. When the energy balance is coupled to the water balance, a positive feedback is possible such that an anomaly of one sign is shifted further away from the equilibrium, at least locally. Figures 4-9b and 4-10b show that when viewed in the coupled $s - T_g$ space, the negative soil moisture anomaly becomes more (negative) anomalous during its trajectory towards equilibrium. The strength of this effect has been shown to be related to the degree of water and energy balance coupling through the evaporation efficiency function β. Because this function dramatically changes its shape at the switch between soil-control and atmosphere-control evaporation regime, asymmetric recovery times from anomalies are possible (Figure 4-6).

So far the focus has been on the deterministic evolution of the system. The same turbulent and radiative fluxes that link the four state variables and produce the deterministic drift function $\mathbf{G}(\mathbf{x}_t)$, define the diffusion function $\mathbf{g}(\mathbf{x}_t)$ which measures the strength and direction of the responses of the state variables to the noise. In this case noise enters the system through wind speed, affecting both advection and

turbulent fluxes.

4.6.2 Diffusion

The deterministic solution trajectories described above assume an initial condition $\mathbf{x}_o$; because the equilibrium is stable, a non-equilibrium initial condition can only arise due to noise. The complete stationary probability density function of each system is determined by the solution to the full Îto equation (3.5) and depends on both drift and diffusion through the Fokker-Planck equation,

$$\frac{\partial f_s}{\partial t} = 0 = -\sum_i \frac{\partial}{\partial x_i}(G_i f_s) + \frac{1}{2}\sum_{ij} \frac{\partial^2}{\partial x_i \partial x_j}\left(\mathbf{g}\mathbf{g}_{ij}^T f_s\right) \tag{4.6}$$

where $f_s = f_s(s, T_g, q_m, \theta_m)$ represents the stationary multivariate probability density function for the system. The components of the $\mathbf{g}(\mathbf{x})$ function establish a heterogeneous, non-isotropic diffusion that the stationary probability must balance. The covariance structure is thus the result of both the drift and the diffusion functions.

The classic deterministic approach used in Section 4.6.1 is to give a non-equilibrium initial condition and allow the system to restore to equilibrium. In reality, the state is being continuously buffeted by noise as it tries to move along its recovery path. In a system with state-dependent noise, this buffeting is not totally random; it depends on the physical linkages in the model.

Vector plots of (g_1, g_3), the ds and dT_g components of the diffusion term, show the state-dependence of the system's susceptibility to random perturbations (Figures 4-11 and 4-12). In these figures, the two components of the $\mathbf{g}$ function are indicated by a 2-headed arrow emanating from each (s, T_g) point having non-negligible stationary probability. The gaussian-distributed incremental noise dw_t may take either a positive or a negative sign with equal probability, hence the two-headed arrows. The arrow has a horizontal component proportional to the expected value of g_1, and a vertical component proportional to the expected value of g_3, where, as before, the expectations are conditional on that (s, T_g). The g_1 component corresponds to the effect of noise on soil moisture evolution whereas the g_3 component is the magnitude of the modulation of noise for the third state variable, soil temperature.

The relative magnitude of the vectors shows that for a given s, the state is increasingly susceptible to noise as T_g increases. The direction of the vectors indicates that as T_g increases, the noise affects s less and T_g more. (The same pattern is observed in the diffusion vector plot, both for the *Control* and the *Two-regime-β* solution.) This

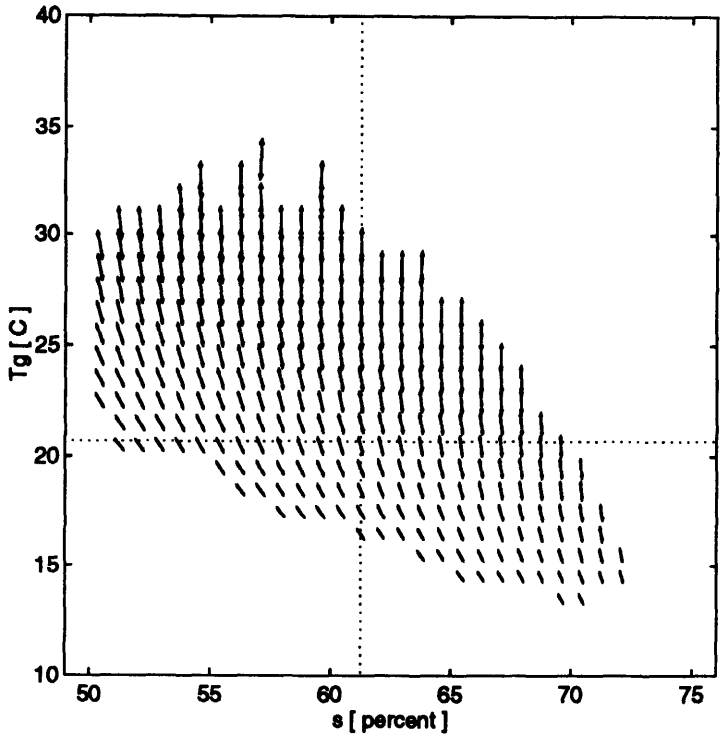

Figure 4-11: Vector plot of the noise contribution to (s, T_g) evolution in the *Control* solution. The diffusion vector components g_1 and g_3 are averaged over the other two state variables.

behavior is again due to the rapid restoration of the surface-air temperature gradient through sensible heat flux. This same behavior is evident in the deterministic component of the system (Figures 4-9c and 4-10c). The sensible heat flux mechanism goes towards structuring this apparent dependence of the drift and diffusion function on the state of the system. Recovery from anomalies in state variables is thus intricately linked to the location of the anomaly in state-space, i.e., type of anomaly, dry or moist, warm or cool, in the atmosphere or in the soil.

Now, consider the system state as a particle moving in state-space. If the particle finds itself in a hot dry state, the drift term (Figures 4-7 and 4-8) is likely to cause further drying to cool by latent heat exchange. At the same time, random noise (Figures 4-11 and 4-12) may perturb it to an even hotter state — but not moister, due to the lack of a g_1 component in this range. A physical implication is that when ground temperature is high, even a large perturbation will not serve to moisten the system. (Conversely, at this high ground temperature, noise does not cause further drying either; however, the deterministic drift term may cause drying.)

Finally we examine an important diagnostic related to the finding that the system in an anomalous state tends to first (and rapidly) adjust the temperature gradient

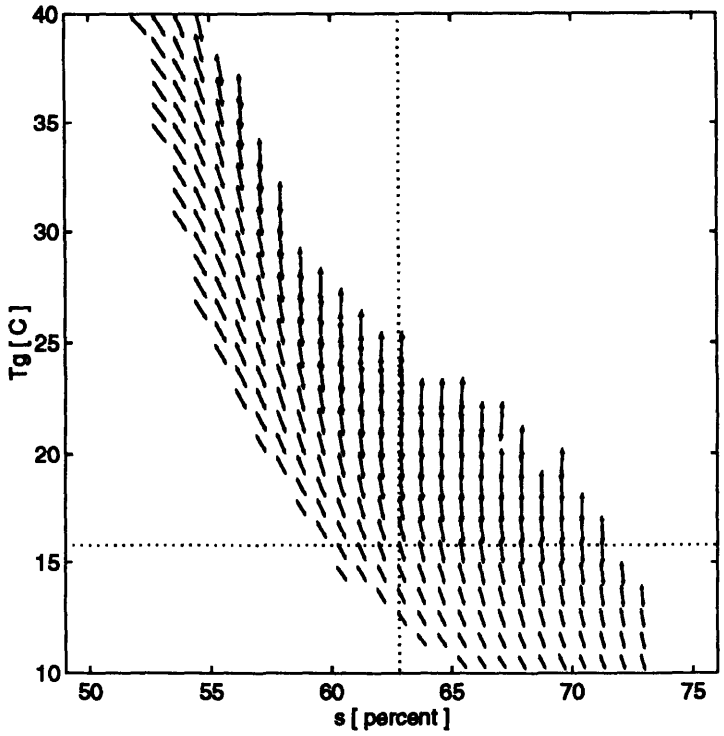

Figure 4-12: Vector plot of the noise contribution to (s, T_g) evolution in the *Two-regime-β* solution. The diffusion vector components g_1 and g_3 are averaged over the other two state variables.

$(T_g - \theta_m)$ to near the equilibrium value and then follow trajectories along this line to the full restoration of equilibrium $\mathbf{x}^\star$ at a relatively (and increasingly) slower rate. Figure 4-13 is a plot of the drift components G_3 and G_4 that are the deterministic restoring forcings of the soil temperature T_g and atmosphere potential temperature θ_m. The vectors indicate that wherever the anomaly is situated, the primary tendency is to rapidly move towards the equilibrium temperature gradient (indicated on Figure 4-13 by the dashed line). The tendency is stronger, the larger the disequilibrium. This is also the case in the *Two-regime-β* deterministic trajectories; however, once on the constant $(T_g - \theta_m)$ curve in that solution, the system has farther to travel to reach equilibrium, owing to the greater (s, T_g) correlation.

An interesting result in Figure 4-13 is that once on the equilibrium temperature gradient (dashed line) there is very small deterministic drift towards the equilibrium point $\mathbf{x}^\star$. Full recovery to the equilibrium point has to be achieved through the remaining dependencies in the land-atmosphere system.

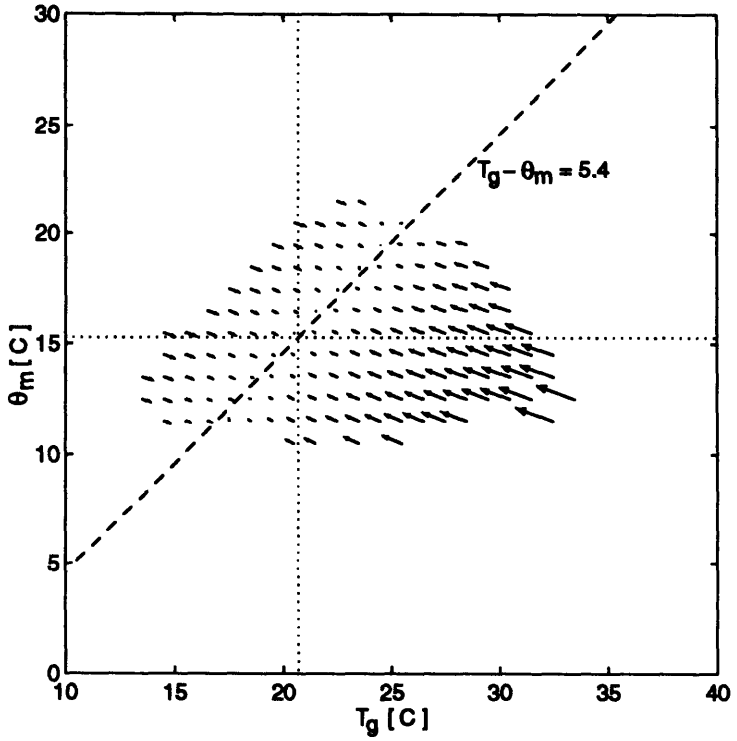

Figure 4-13: Vector plot of the deterministic contribution to (T_g, θ_m) evolution in the *Control* solution. The drift vector components G_3 and G_4 are averaged over the other two state variables.

4.7 Conclusions and Discussion

The asymmetry of first-passage times from dry and moist anomalies across the normal state of soil moisture is found to hold for the *Two-regime-β* solution, in which evaporation switches between soil and atmosphere control. This difference arises from a stronger correlation between soil moisture and soil temperature in the soil-controlled regime. The correlation, in turn, is created by the form of evaporation efficiency β through both the drift and diffusion terms.

Positive soil moisture feedbacks (anomaly-enhancing mechanisms) exist in both solutions, due to the role of evaporation in balancing both the hydrologic and the heat balance, and due to the fact that evaporation is a product, $E = E_p\beta$, where β increases with s, and E_p with T_g. Enhanced evaporation constitutes a means to restore from a wet or a hot anomaly, but it exacerbates a dry or a cool anomaly. Anomalies tend to be wet and cool, or hot and dry; therefore the restoration and anomaly-enhancement effects tend to be in competition.

It is only in the *Two-regime-β* solution, however, that these feedbacks are seen to operate asymmetrically for moisture anomalies of different sign. If indeed natural

drought and pluvial phenomena show temporal asymmetries in their recovery time, we may postulate that soil control of evaporation in the dry state, and lack of it in the moist state, helps to account for some of the difference. We may thus expect the patterns of recovery from droughts and wet periods to be most affected by land–atmosphere interaction if the climate of the region straddles the boundary between soil–controlled and energy–limited evaporation regimes. Strong seasonality may also enhance this behavior.

Both land-atmosphere interaction and the functional form of $\beta(s)$ are critical in establishing the correlation between soil temperature and soil moisture. Without the coupling of ground and mixed-layer temperatures, the soil energy budget can be balanced largely by sensible heat flux and is not at the mercy of soil-controlled evaporation. This is evident in both the deterministic trajectories from the dry anomaly in the *Control* case and in the auto-correlation analysis in Chapter 3.

Water-energy coupling at the land surface results in the presence of positive soil moisture anomaly feedbacks that are not evident if the water balance is considered alone. The next step in this analytical work is to decompose the model's drift and diffusion functions to isolate positive and negative feedback mechanisms, and to identify and quantify the physical processes controlling restoring and coupling terms in the multivariate system.

Chapter 5

Analysis of Feedback Mechanisms

5.1 Introduction

The heat and moisture budgets at the land surface are linked by evaporation, which is an expenditure of both energy and water mass. As a result of this and other equally important linkages in land–atmosphere interaction, the soil heat and moisture states tend to be negatively correlated, either warm-dry or cool-moist. When the evaporation rate responds to an anomalous state, the water and energy budgets are in competition. In a warm-dry anomaly, the elevated temperature creates a demand for *increased* evaporation to cool the surface; at the same time, the low moisture state requires *restricted* evaporation to allow re-moistening.

Chapter 4 demonstrated the presence of these feedbacks by analyzing system transitions in soil-moisture/soil-temperature state-space, for a simplified mathematical model of land-atmosphere interaction. Feedback mechanisms that are not apparent if soil moisture is considered alone become apparent when the surface water and energy budgets in both land and atmosphere are allowed to affect one another. In this Chapter, the model equations are decomposed to isolate the physical processes responsible for these feedbacks, as well as to determine the sign and magnitude of their competing contributions.

The mathematical model provides a unique opportunity to quantify positive and negative feedbacks in the coupled water and energy budgets at the land surface. The covariabilities among the model states are due to internal constraints; they arise through the equations describing the states' physical linkages and are not prescribed at the outset as in, for example, a statistical model. The deterministic drift and diffusion equations are analytically tractable, owing to the model's low dimensionality.

The major challenge in investigations of land–atmosphere interaction is to decipher the major influences and feedbacks when the many state variables and physical processes in water and energy balance are all interconnected in complicated ways. If we sketch a diagram of even the simplest representation of the land-atmosphere system and draw arrows between the states and processes that affect one another (Figure 1-1), it is still extremely difficult to predict the net effect of a change in one state or system parameter. For example, precipitation recycling creates a positive feedback in regional soil moisture, but moisture-controlled infiltration capacity and evaporation efficiency contribute restoring forces — negative feedbacks. When the soil dries and heats, the *coupled* moisture/temperature state can create a positive moisture feedback — further drying. Which processes dominate? Under what conditions? And why? The simplified analytic model allows us to dissect and — more importantly — quantify the "arrows" in conceptual diagrams such as Figure 1-1.

5.2 Stochastic Model

For convenience, the stochastic land–atmosphere interaction model, as developed in Chapters 2 and 3 is briefly reviewed here. The model is composed of a one-dimensional (in the vertical) four-state balance for the soil and turbulently-mixed atmospheric boundary layer reservoirs of heat and moisture; the radiative and turbulent heat fluxes that couple these states are explicitly represented. The major simplifying assumptions in the model are: 1) adiabatic mixing in the boundary layer, and 2) parameterization of warm dry air entrainment *in lieu* of variations in boundary layer height. The source of noise is considered to be in the advection of air-mass; the regional wind-speed is taken to be composed of a mean component with additions of uncorrelated white-noise as perturbations around this mean value. The time evolution of the system is described by the multivariate Îto stochastic differential equation,

$$d\mathbf{x}_t = \mathbf{G}(\mathbf{x}_t)dt + \mathbf{g}(\mathbf{x_t})dw_t\,, \tag{5.1}$$

where dw_t represents the differential of the Wiener process (white noise), and the time-varying state vector is defined as

$$\mathbf{x}_t = [s\; q_{\rm m}\; T_{\rm g}\; \theta_{\rm m}]^T \tag{5.2}$$

Table 5.1: Statistics of State Variables, *Control* Solution

Index j	Variable	Equilibrium Solution $x^\star$	Stochastic Solution $\overline{x}$	Stochastic Solution σ_x
1	s [ ]	0.613	0.611	0.043
2	q_m [g kg^{-1}]	4.27	4.25	0.39
3	T_g [deg C]	20.7	20.6	2.1
4	θ_m [deg C]	15.3	15.5	1.4
5	$T_g - \theta_m$ [deg C]	5.4	5.3	1.7

where s represents relative soil saturation (soil moisture, dimensionless), q_m specific humidity in the mixed layer [g H_2O (kg air)$^{-1}$], T_g soil temperature [°C], and θ_m potential temperature in the mixed layer [°C]. In equation (5.1), $\mathbf{G}(\mathbf{x}_t)$ is the *drift* function; its four components $G_1(\mathbf{x}_t)$, $G_2(\mathbf{x}_t)$, $G_3(\mathbf{x}_t)$, $G_4(\mathbf{x}_t)$ describe the time evolution of, respectively, s, q_m, T_g, θ_m in the absence of noise. The deterministic function $\mathbf{g}(\mathbf{x}_t) = [g_1(\mathbf{x}_t), g_2(\mathbf{x}_t), g_3(\mathbf{x}_t), g_4(\mathbf{x}_t)]^T$ multiplying the noise is the *diffusion* function, through which the state of the system at the time of the event modulates the influence of the random fluctuation. The notations $G_i(\mathbf{x}_t)$ and $g_i(\mathbf{x}_t)$ are used here to emphasize that each component is a function of all four model states. The full model equations are given in Appendix C and a list of notation is provided in Appendix A.

The 4-equation system is integrated in time using an Euler–type discretization (Pardoux and Talay 1984) of equation (5.1); solution statistics are computed from the resulting stochastic time-series. The presentations in Chapter 3 describe the properties of the stochastic solution upon which the analysis in this paper is based, in particular the marginal probability distributions and covariability structure of the model states. The basic statistics for the model states in this *Control* stochastic solution are given in Table 5.1, together with the equilibrium solution. Comparison of the model equilibrium state $\mathbf{x}^\star$ resulting from $\mathbf{G}(\mathbf{x}^\star) = \mathbf{0}$ and the stochastic expectation $\overline{\mathbf{x}}$ is illuminating in that it illustrates whether the covariability of heat and moisture in the land and atmosphere contribute to the definition of regional climate. In this case, it is apparent that the equilibrium climate is a strong attractor for the system; noise produces fluctuations around this state.

5.3 Definitions and Method

5.3.1 The drift function: Tendency to equilibrate

If the noise term is removed from the right-hand side of equation (5.1), the system is reduced to a set of four coupled ordinary differential equations, describing coupled water and energy balance in the land–atmosphere system:

$$\frac{d\mathbf{x}}{dt} = \mathbf{G}(\mathbf{x}) \, . \tag{5.3}$$

Chapter 2 explored the equilibrium behavior [$\mathbf{G}(\mathbf{x}^\star) = \mathbf{0}$] of this deterministic form of the model and its sensitivity to several important parameters. The model is an open system, for both energy and water mass; the equilibrium solution reflects the existence of temperature and moisture states that balance the specified external insolation and water mass convergence. At this 4-variable equilibrium state, the model's air and soil stores are coupled in terms of both the water and energy states such that the net incoming solar radiation is exactly balanced by longwave back-radiation and latent heat advection; moisture convergence is exactly balanced by runoff; and the net exchange between air and soil is zero for both water mass and energy. This does not imply that the fluxes themselves are zero — they are not — but that they are in balance. From any physically realistic initial state, in the absence of noise, the $\mathbf{G}(\mathbf{x})$ function will drive the system to $\mathbf{x}^\star$.

Because $\mathbf{x}^\star$ is a stable equilibrium of the system , it is a natural choice to analyze the deterministic behavior of $\mathbf{x}(t)$ in relation to $\mathbf{x}^\star$. The $G(x)$ function is expanded in truncated Taylor series around $\mathbf{x}^\star$, for $i = 1, 4$:

$$G_i(\mathbf{x}) \approx G_i\left(\mathbf{x}^\star\right) + \left.\frac{\partial G_i}{\partial s}\right|_{\mathbf{x}^\star} (s - s^\star) + \left.\frac{\partial G_i}{\partial q_\mathrm{m}}\right|_{\mathbf{x}^\star} (q_\mathrm{m} - q_\mathrm{m}^\star) + \left.\frac{\partial G_i}{\partial T_\mathrm{g}}\right|_{\mathbf{x}^\star} \left(T_\mathrm{g} - T_\mathrm{g}^\star\right) + \left.\frac{\partial G_i}{\partial \theta_\mathrm{m}}\right|_{\mathbf{x}^\star} (\theta_\mathrm{m} - \theta_\mathrm{m}^\star) \tag{5.4}$$

When the differentiation in (5.4) is performed, a number of common terms appear with opposite sign in the T_g and θ_m derivatives, due to the presence of the temperature gradient $T_\mathrm{g} - \theta_\mathrm{m}$ in the turbulent flux terms. Clearly, an equilibrium temperature difference exists; it is given the notation $\Delta^\star$, where $\Delta = T_\mathrm{g} - \theta_\mathrm{m}$. Thus, (5.4) may be rewritten to include the dependence of each drift component on the system's departure from its equilibrium temperature gradient, as well as on the departure

from its equilibrium state in absolute terms:

$$G_i(\mathbf{x}) \approx \left.\frac{\partial G_i}{\partial s}\right|_{\mathbf{x}^\star}(s - s^\star) + \left.\frac{\partial G_i}{\partial q_\mathrm{m}}\right|_{\mathbf{x}^\star}(q_\mathrm{m} - q_\mathrm{m}^\star) + \left.\frac{\partial G_i}{\partial T_\mathrm{g}}\right|_{\mathbf{x}^\star}\left(T_\mathrm{g} - T_\mathrm{g}^\star\right) + \left.\frac{\partial G_i}{\partial \theta_\mathrm{m}}\right|_{\mathbf{x}^\star}(\theta_\mathrm{m} - \theta_\mathrm{m}^\star) + \left.\frac{\partial G_i}{\partial \Delta}\right|_{\mathbf{x}^\star}(\Delta - \Delta^\star) \ . \tag{5.5}$$

In equation (5.5), $G_i(\mathbf{x}^\star)$, which is by definition equal to zero, has been omitted. To non-dimensionalize the various state disequilibria for ease of comparison in the analysis that follows, each difference $x_j - x_j^\star$ is divided by the stationary standard deviation of the respective state; the notation δx_j is introduced to signify the non-dimensional disequilibrium in variable j,

$$\delta x_j = \frac{x_j - x_j^\star}{\sigma_{x_j}} \ . \tag{5.6}$$

In the analysis, the non-dimensional disequilibria are referred to as δs, δT_g, and so forth. With this notation, equation (5.5) can be compactly written as

$$G_i(\mathbf{x}) \approx \sum_{j=1}^{5} \Lambda_{ij}\delta x_j = \Lambda_{i1}\delta s + \Lambda_{i2}\delta q_\mathrm{m} + \Lambda_{i3}\delta T_\mathrm{g} + \Lambda_{i4}\delta\theta_\mathrm{m} + \Lambda_{i5}\delta\Delta. \tag{5.7}$$

The coefficients Λ_{ij} are the derivatives (linear coefficients) of the drift function for the i^{th} state variable with respect to the j^{th} variable.

5.3.2 Definition of restoring and coupling terms

According to (5.7), each G_i is approximated by a weighted sum of the various disequilibria, where each weight Λ_{ij} is determined by the various physical processes through which a disequilibrium in variable j affects the evolution of variable i.

Let us first examine the terms where $i = j$, that is, the effect of a variable's disequilibrium upon its own evolution. For a self-restoring process, Λ_{ii} must be negative, consistent with the definition of a negative feedback as one that counteracts an anomaly. The terms Λ_{ii} indicate each variable's tendency to restore itself toward its own equilibrium, and therefore will be called *restoring* terms. If Λ_{ii} is positive, then disequilibrium in the state variable is enhanced due to some positive feedback influences in the water and energy balance.

The terms $\Lambda_{ij}, i \neq j$, express the effect of disequilibrium in variable j on the evolution of variable i. If Λ_{ij} is positive, then an above-equilibrium δx_j will contribute

to an increase in variable i, regardless of whether δx_i is positive or negative. The terms $\Lambda_{ij}, i \neq j$ are *coupling* terms; they signify the dependence of variables upon each other's disequilibria.

Rewriting (5.7) in complete matrix form shows that the restoring terms (underlined) are the diagonal terms of the matrix that transforms the vector of non-dimensional disequilibria to the approximate drift functions:

$$\begin{bmatrix} G_1 \\ G_2 \\ G_3 \\ G_4 \end{bmatrix} \approx \begin{bmatrix} \underline{\Lambda_{11}} & \Lambda_{12} & \Lambda_{13} & \Lambda_{14} & \Lambda_{15} \\ \Lambda_{21} & \underline{\Lambda_{22}} & \Lambda_{23} & \Lambda_{24} & \Lambda_{25} \\ \Lambda_{31} & \Lambda_{32} & \underline{\Lambda_{33}} & \Lambda_{34} & \Lambda_{35} \\ \Lambda_{41} & \Lambda_{42} & \Lambda_{43} & \underline{\Lambda_{44}} & \Lambda_{45} \end{bmatrix} \begin{bmatrix} \delta s \\ \delta q_{\mathrm{m}} \\ \delta T_{\mathrm{g}} \\ \delta \theta_{\mathrm{m}} \\ \delta \Delta \end{bmatrix} \tag{5.8}$$

Once we derive the expressions for Λ_{ij} in the analytic model of land–atmosphere interaction and coupled water and energy balance, we may then evaluate their sign and magnitude to identify and quantify the feedback processes contributing to climatic and hydrologic variability (see Figure 1-1).

5.3.3 The diffusion function: Susceptibility to noise

The diffusion function components, which multiply the noise in (5.1), are also expanded in Taylor series about the same $\mathbf{x}^*$ as in equation (5.4), with the result,

$$g_i(\mathbf{x}) \approx g_i(\mathbf{x}^*) + \lambda_{i1}\delta s + \lambda_{i2}\delta q_{\mathrm{m}} + \lambda_{i3}\delta T_{\mathrm{g}} + \lambda_{i4}\delta \theta_{\mathrm{m}} + \lambda_{i5}\delta \Delta \, . \tag{5.9}$$

In (5.9), $g_i(\mathbf{x}^*)$ must be included because it is not necessarily equal to zero. In fact, it is necessary that at least one g_i be non-zero at $\mathbf{x}^*$ for a stochastic solution to exist. If all the diffusion functions were zero at the deterministic equilibrium, then noise could not perturb the system from that equilibrium, and once in the equilibrium state, the system would no longer evolve either randomly or deterministically. Each λ_{ij} in equation (5.9) represents the susceptibility of variable i to random perturbations due to the effect of a disequilibrium in variable j. Again, it is emphasized that the expressions for λ_{ij} and Λ_{ij} are derived from an analytic model of land–atmosphere interaction, which represents the coupled water and energy balance between the soil and the near-surface atmosphere.

5.4 Decomposition of the Terms

The drift and diffusion functions $\mathbf{G}(\cdot)$ and $\mathbf{g}(\cdot)$ in the evolution of land and atmospheric moisture and temperature states are defined through the coupled water and energy balance for the soil and the well-mixed atmospheric boundary layer. The exchanges of mass and energy link the four state variables in two-way land–atmosphere interaction (The full equations are given in Appendix C). The restoring and feedback factors quantified by the linear coefficients Λ_{ij} and λ_{ij} are thus physically based through these balance equations. In this Section, the component parts of the weighting terms are decomposed and their physical meaning discussed. Differences in sign are noted in this Section, but numerical values are not assigned until the following Section.

5.4.1 Soil moisture drift

The restoring term Λ_{11} represents the effect of soil moisture itself on the physical processes that re-equilibrate it from a disequilibrated state. Here a runoff ratio, φ, has been defined, such that φ equals the ratio of runoff to precipitation, and $(1-\varphi)$ equals the ratio of infiltration to precipitation. The evaporation efficiency β represents the soil control on evaporation; it is the ratio of the allowed evaporative flux to the energy-limited potential value. From equation (C.7) and the definition of Λ_{11},

$$
\begin{aligned}
\Lambda_{11} &= \frac{\partial G_1}{\partial s}\sigma_s = \\
\text{(a)} \qquad & + (1-b)\frac{M q_{\text{in}} \overline{U}}{\rho_{\text{w}}}\frac{d}{ds}(1-\varphi)\,\sigma_s \\
\text{(b)} \qquad & + (1-b)\frac{\left(C_1\overline{U} + C_2 w_{\text{B}}\right)\rho\left[q^*\left(T_{\text{g}}, p_{\text{s}}\right) - q_{\text{m}}\right]}{\rho_{\text{w}}}\frac{d}{ds}\left[(1-\varphi)\,\beta\right]\sigma_s \\
\text{(c)} \qquad & - \frac{\left(C_1\overline{U} + C_2 w_{\text{B}}\right)\rho\left[q^*\left(T_{\text{g}}, p_{\text{s}}\right) - q_{\text{m}}\right]}{\rho_{\text{w}}}\frac{d\beta}{ds}\sigma_s
\end{aligned}
\tag{5.10}
$$

The subterms (a) and (b) represent the infiltration of precipitation water. In both, the factors $(1-b)$ and the vapor gradient are always positive at the equilibrium point. Subterm (a) is the infiltration of that precipitation water derived from moist advection. Subterm (b) is the infiltration of precipitation water derived from local evaporation. Because the infiltration fraction of precipitation $(1-\varphi)$ is generally decreasing with increasing soil saturation, the infiltration process due to large-scale advective forcing is a negative feedback mechanism for soil moisture anomalies [sub-

term (a) is always a negative contribution to Λ_{11}]. The infiltration of locally derived (recycled) precipitation, nonetheless, may be either a positive or negative feedback, depending on the surface hydrologic partitioning. The runoff ratio φ and evaporation efficiency β are both increasing functions of soil saturation; the term $\frac{d}{ds}[(1-\varphi)\beta]$ may take either sign depending on the partitioning of hydrologic fluxes at the surface. The locally-recycled precipitation water may thus constitute a positive feedback on soil moisture anomalies. The final subterm (c) represents the evaporative loss of soil moisture in the land water balance equation. Its contribution to soil moisture anomalies and Λ_{11} necessarily constitutes a negative feedback and a restoring force. Drier soils reduce evaporation efficiency and thus tend to remoisten if precipitation occurs. Moist soils are subject to enhanced evaporation when the energy is available, thus also tend to restore soil moisture anomalies.

The term Λ_{12} quantifies the coupling of soil moisture drift to specific humidity disequilibrium:

$$\begin{aligned}\Lambda_{12} &= \frac{\partial G_1}{\partial q_{\mathrm{m}}}\sigma_q \\ &= [1-(1-b)(1-\varphi)]\frac{\rho}{\rho_{\mathrm{w}}}\left(C_1\overline{U}+C_2 w_{\mathrm{B}}\right)\beta\sigma_q \end{aligned} \tag{5.11}$$

This term is necessarily positive. A moist disequilibrium in air humidity decreases the humidity gradient in the surface sublayer and thus suppresses net evaporation. (In this expression, net evaporation equals total evaporation minus recycled precipitation.) Conversely, a dry air humidity disequilibrium enhances net evaporation. Depending on the correlation of soil moisture and air specific humidity, this physical interaction may constitute either positive or negative feedback.

The coupling of soil moisture drift to disequilibrium in soil temperature is given by Λ_{13}:

$$\begin{aligned}\Lambda_{13} &= \left(\frac{\partial G_1}{\partial T_{\mathrm{g}}}-\mathcal{F}\right)\sigma_T \\ &= -[1-(1-b)(1-\varphi)]\frac{\rho}{\rho_{\mathrm{w}}}\frac{\partial q^*}{\partial T_{\mathrm{g}}}\left(C_1\overline{U}+C_2 w_{\mathrm{B}}\right)\beta\sigma_T \end{aligned} \tag{5.12}$$

As discussed above, the term Λ_{13} does not include all the constituents of $\partial G_1/\partial T_{\mathrm{g}}$; the items that arise in common with $(-\partial G_1/\partial\theta_{\mathrm{m}})$ are indicated by $\mathcal{F}$ and appear in Λ_{15}, multiplying the temperature difference, Δ. A very important property to note is that this term is necessarily negative; $[1-(1-b)(1-\varphi)]$ is always greater than zero. A positive disequilibrium in T_{g} (usually occurring when the soil is dry) raises potential

evaporation through the strong temperature dependence of ground–surface saturation specific humidity [$\partial q^*/\partial T_g$ appears in (5.12)], thus exerting a drying influence in the soil moisture drift. This is the source of the strong positive feedback on soil moisture evolution, and it is brought about by the coupling of water and energy balances.

A disequilibrium in absolute air-slab potential temperature drives soil moisture drift through the term Λ_{14}:

$$\begin{aligned}\Lambda_{14} &= \left(\frac{\partial G_1}{\partial \theta_m} + \mathcal{F}\right)\sigma_\theta \\ &= [1-(1-b)(1-R)]\frac{\rho}{\rho_w}C_2\sqrt{gh\frac{T_g-\theta_m}{\theta_m}}\frac{1}{\theta_m}\beta\sigma_\theta \end{aligned} \tag{5.13}$$

This term arises from the presence of θ_m in the denominator of the buoyancy velocity scale, w_B. In w_B, the expression $g(T_g-\theta_m)/\theta_m$ represents the buoyancy acceleration that a parcel of air at the surface would experience if lifted adiabatically into the mixed layer. The square root of this acceleration multiplying a distance (here, the mixed-layer thickness h) gives a velocity scale for the buoyant thermals, which is related to the surface turbulent fluxes. For a given temperature gradient $(T_g-\theta_m)$, buoyant acceleration decreases as the coupled absolute temperatures increase. Therefore, in equation (5.13), an increase in absolute θ_m — independent of a change in Δ — suppresses evaporation and provides a moistening influence, a negative feedback if the soil is dry.

The effect of land–atmosphere thermal coupling on soil moisture evolution is given by Λ_{15}:

$$\begin{aligned}\Lambda_{15} &= \mathcal{F}\sigma_\Delta \\ &= -[1-(1-\varphi)(1-b)]\frac{\rho}{\rho_w}[q^*(T_g,p_s)-q_m]\frac{1}{2}C_2\sqrt{gh}\left(\frac{T_g-\theta_m}{\theta_m}\right)^{-1/2}\frac{1}{\theta_m}\beta\sigma_\Delta \end{aligned} \tag{5.14}$$

This necessarily negative term arises from the presence of $\Delta = T_g - \theta_m$ in the numerator of the buoyancy veclocity scale. For a given θ_m, as the temperature gradient increases, thermal buoyancy and consequently evaporation are enhanced. This also constitutes a contribution to positive feedback influences on the evolution of dry soil moisture anomalies.

5.4.2 Soil temperature drift

The contribution of disequilibrium in each variable j to the state-dependent deterministic evolution of soil temperature is estimated by the weighting terms Λ_{3j} in the approximation to G_3.

The effect of soil moisture disequilibrium is through Λ_{31},

$$\begin{aligned}
\Lambda_{31} &= \frac{\partial G_3}{\partial s}\sigma_s = \\
\text{(a)} \quad & -\frac{d\alpha}{ds} RS \frac{1}{C_s Z_t}\sigma_s \\
\text{(b)} \quad & -\lambda\left(C_1\overline{U} + C_2 w_{\mathrm{B}}\right)\rho\left[q^*\left(T_{\mathrm{g}}, p_{\mathrm{s}}\right) - q_{\mathrm{m}}\right]\frac{d\beta}{ds}\frac{1}{C_s Z_t}\sigma_s
\end{aligned} \tag{5.15}$$

Here, subterm (a) is the effect of soil-moisture controlled albedo $[\alpha(s)]$ on dT_{g}. Moist soil (high δs) means a less reflective surface; α decreases with increasing s ($d\alpha/ds$ is negative) and the contribution of this term is that moister soil has a warming influence. Although albedo may depend only weakly on soil moisture, this term may be large, due to the dominance of solar radiation in the energy balance. Subterm (b) reflects soil moisture control of evaporation; evaporation efficiency $[\beta(s)]$ increases with moister soil ($d\beta/ds$ is positive). Thus, moister soil contributes a cooling influence.

Disequilibrium in air-slab specific humidity q_{m} drives soil temperature evolution through Λ_{32}:

$$\begin{aligned}
\Lambda_{32} &= \frac{\partial G_3}{\partial q_{\mathrm{m}}}\sigma_q = \\
\text{(a)} \quad & (1-\alpha) RS_e \frac{\partial Y_c}{\partial q_{\mathrm{m}}}\frac{1}{C_s Z_t}\sigma_q \\
\text{(b)} \quad & +(1-\epsilon_{\mathrm{col}})\frac{\partial}{\partial q_{\mathrm{m}}} RL_{\mathrm{ad}}\frac{1}{C_s Z_t}\sigma_q \\
\text{(c)} \quad & -RL_{\mathrm{ad}}\frac{\partial}{\partial q_{\mathrm{m}}}\epsilon_{\mathrm{col}}\frac{1}{C_s Z_t}\sigma_q \\
\text{(d)} \quad & +\left(\sigma\theta_{\mathrm{m}}^4\frac{\partial}{\partial q_{\mathrm{m}}}\epsilon^{\downarrow}X_c)\right)\frac{1}{C_s Z_t}\sigma_q \\
\text{(e)} \quad & +\left(RL_{\mathrm{sdc}}\frac{\partial}{\partial q_{\mathrm{m}}}X_c\right)\frac{1}{C_s Z_t}\sigma_q \\
\text{(f)} \quad & +\lambda\beta\left(C_1 U_z + C_2 w_{\mathrm{B}}\right)\rho\frac{1}{C_s Z_t}\sigma_q
\end{aligned} \tag{5.16}$$

In subterm (a), Y_c signifies the effect of clouds in blocking solar radiation. $\partial Y_c/\partial q_{\mathrm{m}}$ is negative (more water vapor, more cloud, less solar radiation), therefore a positive

air humidity disequilibrium has a cooling effect on soil temperature if this factor were considered alone. Subterm (b) is the enhancement of above-slab downwelling longwave due to both vapor and cloud; $RL_{\rm ad}$ increases with increased humidity — a warming effect; however, this effect is largely cancelled by re-absorption of $RL_{\rm ad}$ in the mixed layer itself due to enhanced emissivity/absorptivity (c). Subterms (d) and (e) reflect the effect of $q_{\rm m}$ on the downward longwave radiation from the mixed–layer through the clear-sky radiation and the cloud correction (X_c). An anomalously moist air slab has a warming influence on the soil by suppressing the latent heat flux from the soil slab (f).

The soil temperature state influences its own deterministic drift through the restoring term Λ_{33}:

$$\begin{aligned}
\Lambda_{33} &= \left(\frac{\partial G_3}{\partial T_{\rm g}} - \mathcal{E}\right)\sigma_T = \\
\text{(a)} \qquad & - 4\sigma T_{\rm g}^3 \frac{1}{C_s Z_t}\sigma_T \\
\text{(b)} \qquad & - \lambda\beta\left(C_1\overline{U} + C_2 w_{\rm B}\right)\frac{\partial q^*}{\partial T_{\rm g}}\rho\frac{1}{C_s Z_t}\sigma_T
\end{aligned} \tag{5.17}$$

These terms are both necessarily negative, as expected for a self-restoring state: the fourth-power longwave back-radiation (a), and the dependence of potential evaporation on temperature-dependent saturation specific humidity ($\partial q^*/\partial T_{\rm g} > 0$) (b). The important roles of soil temperature in the turbulent sensible and latent heat flux occur due to the gradient between $T_{\rm g}$ and $\theta_{\rm m}$, not due to absolute $T_{\rm g}$; therefore these terms (indicated by $\mathcal{E}$) appear in Λ_{35} below.

Absolute mixed-layer potential temperature affects $T_{\rm g}$ through Λ_{34}:

$$\begin{aligned}
\Lambda_{34} &= \left(\frac{\partial G_3}{\partial \theta_{\rm m}} + \mathcal{E}\right)\sigma_\theta \\
\text{(a)} \qquad & (1-\alpha) RS_e \frac{\partial}{\partial \theta_{\rm m}} Y_c \frac{1}{C_s Z_t}\sigma_\theta \\
\text{(b)} \qquad & + \left(\frac{\partial}{\partial \theta_{\rm m}} RL_{\rm adc} X_c + RL_{\rm adc}\frac{\partial}{\partial \theta_{\rm m}} X_c\right)\frac{1}{C_s Z_t}\sigma_\theta \\
\text{(c)} \qquad & + \left(\frac{\partial}{\partial \theta_{\rm m}} RL_{\rm sdc} X_c + RL_{\rm sdc}\frac{\partial}{\partial \theta_{\rm m}} X_c\right)\frac{1}{C_s Z_t}\sigma_\theta \\
\text{(d)} \qquad & + \lambda\beta C_2\rho\left[q^*\left(T_{\rm g}, p_{\rm s}\right) - q_{\rm m}\right]\frac{\sqrt{gh}}{2}\sqrt{\frac{T_{\rm g}-\theta_{\rm m}}{\theta_{\rm m}}}\frac{1}{\theta_{\rm m}}\frac{1}{C_s Z_t}\sigma_\theta \\
\text{(e)} \qquad & + C_2\rho C_{\rm pa}\left(T_{\rm g} - \theta_{\rm m}\right)\frac{\sqrt{gh}}{2}\sqrt{\frac{T_{\rm g}-\theta_{\rm m}}{\theta_{\rm m}}}\frac{1}{\theta_{\rm m}}\frac{1}{C_s Z_t}\sigma_\theta
\end{aligned} \tag{5.18}$$

A positive potential temperature disequilibrium contributes a warming influence on the soil temperature through all the mechanisms that depend on absolute θ_m. Warmer air has decreased relative humidity and is more transparent to solar radiation (warmer air, lower relative humidity, less cloud, more sunshine) (a). Both the overlying atmosphere and slab downwelling longwave fluxes respond to the θ_m^4 dependence and to the LW cloud correction (b and c). The high θ_m in the buoyancy velocity denominator suppresses the turbulent fluxes, contributing an additional warming influence (d).

The weighting term Λ_{35} gives the effect on soil temperature drift of a disequilibrium in land–atmosphere thermal coupling:

$$
\begin{aligned}
\Lambda_{35} &= \mathcal{E}\sigma_\Delta = \\
\text{(a)} \quad & -\rho C_{pa}\left(C_1 U_z + C_2 w_B\right)\frac{1}{C_s Z_t}\sigma_\Delta \\
\text{(b)} \quad & -\rho C_{pa} C_2 \left(T_g - \theta_m\right)\frac{\sqrt{gh}}{2\theta_m}\left(\frac{T_g - \theta_m}{\theta_m}\right)^{1/2}\frac{1}{C_s Z_t}\sigma_\Delta \\
\text{(c)} \quad & -\lambda\beta\rho C_2 \left[q^*\left(T_g, p_s\right) - q_m\right]\frac{\sqrt{gh}}{2\theta_m}\left(\frac{T_g - \theta_m}{\theta_m}\right)^{1/2}\frac{1}{C_s Z_t}\sigma_\Delta
\end{aligned}
\tag{5.19}
$$

A large temperature gradient in the surface sublayer (high $\delta\Delta$) enhances the turbulent fluxes in two ways: the gradient dependence in sensible heat (a) and the transfer coefficient in both the latent and sensible heat fluxes, through the buoyancy velocity (b and c). The result is that a high disequilibrium in Δ leads to cooling of the soil layer, and a low, to warming. This contribution, due to two-way land-atmosphere interaction, is thus necessarily a negative feedback factor for the evolution of soil temperature.

5.4.3 Soil moisture diffusion term

Similar analysis of the diffusion function $\mathbf{g}(\mathbf{x})$ reveals the effect of coupled noise and state–variable disequilibrium on the evolution of anomalies. Because noise is introduced through the wind–speed, which affects advection and turbulent fluxes, this analysis quantifies the relative susceptibility of soil moisture and temperature anomalies to fluctuations in wind speed. Of course, these factors are mediated by disequilibria in the soil and air temperature and moisture states, and the fluxes of water and energy that link them. The diffusion functions' sensitivity to the state disequilibria are decomposed in the same manner as the drift functions.

First, the effect of soil moisture on its own susceptibility to random perturbations

λ_{11} is made up of three contributions:

$$\begin{aligned}
\lambda_{11} &= \frac{\partial g_1}{\partial s}\sigma_s = \\
\text{(a)} \qquad & + (1-b)\frac{M q_{\text{in}}\sigma_{\text{u}}}{\rho_{\text{w}}}\frac{d}{ds}(1-\varphi)\sigma_s \\
\text{(b)} \qquad & + (1-b)\frac{\rho}{\rho_{\text{w}}}\left[q^*\left(T_{\text{g}}, p_{\text{s}}\right) - q_{\text{m}}\right] C_1 \frac{d}{ds}\left[(1-\varphi)\,\beta\right]\sigma_{\text{u}}\,\sigma_s \\
\text{(c)} \qquad & - \frac{\rho}{\rho_{\text{w}}}\left[q^*\left(T_{\text{g}}, p_{\text{s}}\right) - q_{\text{m}}\right] C_1 \sigma_{\text{u}} \frac{d\beta}{ds}\sigma_s
\end{aligned} \tag{5.20}$$

The infiltrated fraction of precipitation $(1-\varphi)$ generally decreases with increasing soil saturation, the s-dependent infiltration of anomalous advection, subterm (a), is a negative factor multiplying the random noise. As discussed in connection with equation (5.10), subterm (b) may take either sign, depending upon the partitioning of fluxes at the surface. The modulation of evaporative loss due to noise, subterm (c), is negative — that is, an above-average wind speed would tend to dry the soil, and this drying effect increases with increased saturation, through β being an increasing function of s.

The magnitude of noise-induced soil moisture perturbations is affected by a disequilibrium in air specific humidity q_{m} through the humidity gradient in potential evaporation,

$$\begin{aligned}
\lambda_{12} &= \frac{\partial g_1}{\partial q_{\text{m}}}\sigma_q \\
&= \left[1-(1-b)(1-\varphi)\right]\frac{\rho}{\rho_{\text{w}}} C_1 \sigma_{\text{u}}\,\sigma_q \beta
\end{aligned} \tag{5.21}$$

and by a soil-temperature disequilibrium through the temperature-dependence of saturation specific humidity,

$$\begin{aligned}
\lambda_{13} &= \frac{\partial g_1}{\partial T_{\text{g}}}\sigma_T \\
&= -\left[1-(1-b)(1-\varphi)\right]\frac{\rho}{\rho_{\text{w}}} C_1 \sigma_{\text{u}} \beta \frac{\partial q^*}{\partial T_{\text{g}}}
\end{aligned} \tag{5.22}$$

The diffusion functions do not include buoyancy velocity w_{B}, which has no noise component in this model. Because w_{B} is the only way that air-slab potential temperature affects the evolution of soil moisture, s diffusion is not affected by disequilibrium in

θ_m and Δ:

$$\lambda_{14} = 0 \tag{5.23}$$

$$\lambda_{15} = 0 \tag{5.24}$$

5.4.4 Soil temperature diffusion term

The soil-moisture dependence of evaporation efficiency and soil heat capacity affect the susceptibility of the temperature state to noise:

$$\lambda_{31} = \frac{\partial g_3}{\partial s}\sigma_s =$$

$$\text{(a)} \qquad -\lambda C_1 \sigma_u \rho \left[q^*(T_g, p_s) - q_m\right] \frac{d}{ds}\beta \frac{1}{C_s Z_t}\sigma_s \tag{5.25}$$

$$\text{(b)} \qquad -C_1 \sigma_u \rho \left[C_{pa}(T_g - \theta_m) + \lambda\beta\left[q^*(T_g, p_s) - q_m\right]\right] \frac{d}{ds} C_s \frac{1}{C_s^2 Z_t}\sigma_s$$

Because $d\beta/ds$ and dC_s/ds are both positive, terms (a) and (b) are both negative.

The mixed layer specific humidity moderates the effect of noise on soil temperature through the vapor gradient,

$$\begin{aligned} \lambda_{32} &= \frac{\partial g_3}{\partial q_m}\sigma_q \\ &= \lambda\beta C_1 \sigma_u \rho \frac{1}{C_s Z_t}\sigma_q \end{aligned} \tag{5.26}$$

The absolute temperature state affects its own sensitivity to noise through saturation specific humidity in potential evaporation:

$$\begin{aligned} \lambda_{33} &= \left(\frac{\partial g_3}{\partial T_g} - \mathcal{D}\right)\sigma_T \\ &= \lambda\beta C_1 \sigma_u \rho \frac{\partial q^*}{\partial T_g}\frac{1}{C_s Z_t}\sigma_T \end{aligned} \tag{5.27}$$

Again, because buoyancy velocity does not appear in the diffusion terms, T_g diffusion is insensitive to absolute mixed-layer potential temperature:

$$\begin{aligned} \lambda_{34} &= \left(\frac{\partial g_3}{\partial \theta_m} + \mathcal{D}\right)\sigma_\theta \\ &= 0 \end{aligned} \tag{5.28}$$

However, diffusion of T_g is dependent on the temperature gradient, Δ, through the

sensible heat flux:

$$\begin{aligned} \lambda_{35} &= \mathcal{D}\sigma_{\Delta} \\ &= -\rho C_{\mathrm{pa}} C_1 \sigma_{\mathrm{u}} \frac{1}{C_s Z_t} \sigma_{\Delta} \end{aligned} \tag{5.29}$$

5.5 Evaluation of the Term-wise Decomposition in the Stochastic Solution

In this Section, the component sub-terms described in Section 5.4 for the drift and diffusion of soil moisture and temperature states are evaluated. The results are presented in Tables 5.2 and 5.3 for the deterministic drift, and in Tables 5.4 and 5.5 for the diffusion functions. [In accordance with equation (5.4), all functions included in the derivatives are evaluated at the control equilibrium solution, $\mathbf{x}^*$.] This analysis quantifies the relative strength of the co-existing positive and negative feedbacks in the evolution of moisture and temperature anomalies.

5.5.1 Drift

In the deterministic drift tables, a positive entry in the column labeled "scaled value" means that a positive disequilibrium in variable j contributes to an *increase* in variable i through the itemized physical mechanism. A negative value indicates that variable i will *decrease* due to a positive disequilibrium in variable j. These also correspond to positive and negative feedback influences on the evolution of the anomalies.

For soil moisture drift (Table 5.2), only the precipitation recycling mechanism could oppose the self-restoring soil moisture effect [see the discussion of Equation (5.10)]. In this case, the positive recycling feedback is insufficient to outweigh the strong negative (restoring) feedback mechanisms of s-dependent infiltration and evaporation efficiency. Thus, all the terms in the water balance (Λ_{11} constituents) are negative feedback factors. The other four states influence soil moisture deterministically through one physical process each; the temperature dependence of surface saturation specific humidity dominates ($\Lambda_{13} = -0.48$ mm day^{-1}) The soil moisture evolution's dependence on temperature disequilibrium (Λ_{13}) is important because it contributes to a strong positive feedback and possible intensification of moisture anomalies. From Equation (5.12), it is evident that a key factor is the slope of the saturation specific humidity on temperature (the thermodynamic Clausius–Clapeyron relationship). Since

Table 5.2: Decomposition of Terms in G_1 (Soil Moisture Drift), *Control* Solution

Term	Multiplies	Sub-term	Scaled Value [mm day^{-1}]
Λ_{11}	δs	Infiltration (advected precipitation)	-0.25
		Recycled precipitation (incl. evaporation efficiency and infiltration)	-0.03
		Evaporation efficiency (total evaporation loss)	-0.36
		Sum	-0.64
Λ_{12}	δq_m	Vapor gradient in potential evaporation	0.08
Λ_{13}	δT_g	Saturation specific humidity	-0.48
Λ_{14}	$\delta \theta_m$	Buoyancy velocity in potential evaporation	0.00
Λ_{15}	$\delta \Delta$	Buoyancy velocity in potential evaporation	-0.22

this relationship is itself related to temperature (slope is approximately exponentially increasing), the strength of the positive feedback depends on the sign and magnitude of the temperature anomaly. Dry anomalies tend to be warm (greater partitioning toward sensible heat flux and higher bowen ratio), therefore this positive feedback is stronger when the soil is in a dry anomaly (drought) than in a wet anomaly (pluvial). There is thus the possibility of asymmetric intensification of anomalies and greater persistence when the soil is anomalously dry. This possibility becomes evident in the analyses of the next Section and is also reflected in the first–passage times computed in Chapter 4.

Disequilibrium in the temperature gradient near the surface is also an influential factor in restoring or enhancing soil moisture anomalies ($\Lambda_{15} = -0.22$ mm day^{-1}).

The situation is more complicated for soil temperature drift (Table 5.3), where each state contributes through at least two physical mechanisms. Among the two influences of soil moisture (albedo and evaporation efficiency), soil control of evaporation efficiency dominates; nonetheless, they are opposite–sign feedbacks on soil temperature. For atmospheric humidity, the relatively large shortwave cloud contribution is essentially cancelled by several terms taking the opposite sign: downwelling longwave radiation and vapor deficit. Vapor-enhanced downwelling longwave radition from above is counteracted by vapor-enhanced re-absorption in the mixed layer; in fact, because of the greater vapor concentration at lower levels, the latter overrides the former.

The soil temperature state is strongly self-restoring, interestingly more so through

Table 5.3: Decomposition of Terms in G_3 (Soil Temperature Drift), *Control* Solution

Term	Multiplies	Sub-term	Scaled Value [deg day^{-1}]	
Λ_{31}	δs	Albedo	0.11	
		Evaporation efficiency	−0.99	
		Sum		−0.88
Λ_{32}	δq_m	Shortwave cloud correction	−1.02	
		Above–slab downwelling longwave (clear–sky and cloud)	0.15	
		Column absorption of same	−0.21	
		Downwelling longwave from slab (clear–sky)	0.34	
		Downwelling longwave from slab (cloud correction)	0.17	
		Vapor deficit in potential evaporation	0.50	
		Sum		−0.08
Λ_{33}	δT_g	Upwelling longwave from soil	−1.19	
		Saturation specific humidity in potential evaporation	−2.62	
		Sum		−3.81
Λ_{34}	$\delta\theta_m$	SW cloud correction	0.44	
		Above–slab downwelling LW (clear–sky and cloud)	0.09	
		Downwelling LW from slab (clear–sky and cloud)	0.35	
		Buoyancy velocity in H	0.00	
		Buoyancy velocity in E_p	0.02	
		Sum		0.90
Λ_{35}	$\delta\Delta$	Gradient in sensible heat flux	−1.52	
		Buoyancy velocity in H	−0.35	
		Buoyancy velocity in E_p	−1.05	
		Sum		−2.91

the temperature dependence of saturation specific humidity, which plays a major role in potential evaporation, than through thermal radiation. The restoring contribution of the ground longwave flux is about half that of $\partial q^*/\partial T_g$. Because $\partial q^*/\partial T_g$ is temperature dependent (Clausius Clapeyron relation), this factor will have different strengths depending on the sign and magnitude of the temperature anomaly.

The decrease in cloudiness due to increased air potential temperature creates an effect on soil temperature drift that equals the effect of net downwelling longwave (b) + (c). The contribution of absolute mixed-layer potential temperature through the buoyancy velocity is small.

A temperature gradient greater than the equilibrium value has a strong cooling influence, $-1.87°$ day^{-1} through the sensible heat flux [(a)+(b)] and $-1.05°$ day^{-1} through latent heat flux (c). The presence of Δ in buoyancy velocity contributes $-1.4°$ day^{-1} [(b)+(c)], about half of the total Δ contribution, demonstrating the importance of free convection to turbulent transfer.

5.5.2 Diffusion

In interpreting the numerical results for the diffusion terms (Tables 5.4 and 5.5), it is important to keep in mind that the noise (zero-mean gaussian perturbations around the mean wind speed) can be either positive or negative with equal probability. This wind anomaly multiplies either a positive or negative disequilibrium in each state, through the approximate g_i functions. It is useful, for purpose of discussion, to consider a positive wind anomaly encountering a positive state disequilibrium.

For the soil moisture diffusion (Table 5.4), $g_1(\mathbf{x}^*)$ is positive, indicating that above-average wind-speed acting on the equilibrium soil moisture state has a moistening influence, that is, the anomalous import of advected moisture outweighs the anomalous evaporation *at that point in state-space.* If an anomalously strong wind encounters a high moisture state (positive δs), both the elevated runoff ratio and evaporation efficiency cause less noise-induced soil-moisture moistening to occur than in the equilibruim state. If the strong wind encounters high soil temperature, then its moistening effect is also decreased due to elevated potential evaporation through $q^*(T_g)$. The effect of anomalously moist air is of the opposite sign: suppressed evaporation would allow the wind anomaly to produce a slightly greater soil moistening than at equilibrium (Table 5.4).

For soil temperature diffusion (Table 5.5), $g_3(\mathbf{x}^*)$ is negative, meaning that at equilibrium, an anomalously strong wind cools the soil. If the soil is moist, then

Table 5.4: Decomposition of Terms in g_1 (Soil Moisture Diffusion), *Control* Solution

Term	Multiplies	Sub-term		Scaled Value [mm day^{-1}]
		$g_1(\mathbf{x}^*)$		0.52
λ_{11}	δs	Infiltration (advected precipitation)	−0.09	
		Recycled precipitation (incl. evaporation efficiency and infiltration)	−0.01	
		Evaporation efficiency (total evaporation loss)	−0.07	
		Sum		−0.17
λ_{12}	δq_m	Vapor gradient in potential evap.		0.02
λ_{13}	δT_g	Saturation specific humidity		−0.11
λ_{14}	$\delta \theta_m$	(does not appear)		0.00
λ_{15}	$\delta \Delta$	(does not appear)		0.00

this cooling is enhanced through evaporation efficiency but suppressed by greater soil heat capacity. If the anomalously high wind encounters warm soil and/or a strong temperature gradient, noise-induced cooling is enhanced with respect to the equilibrium state's response. As in the soil moisture case, a disequilibrium in air humidity has a slight counteracting effect by suppressing the noise-induced component of evaporation.

5.6 Analysis of Moisture Anomalies in the *Control* Stochastic Solution

The analyses in Sections 5.4 and 5.5 focused on the identification and quantification of the interactions and feedbacks inherent in coupled water and energy balance in two-way land-atmosphere interaction. The influence of the physical linkages in soil and atmosphere heat and moisture states on the evolution of the state variables have been represented by linear coefficients (Λ_{ij} and λ_{ij}) that multiply anomalous departures of the state variables from their equilibrium. In this sense, the sign of the these coefficients signifies the character of the feedback (negative or positive) and their magnitude represent the strength of the component. They force either restoration or reinforcement of disequilibrium.

Table 5.5: Decomposition of Terms in g_3 (Soil Temperature Diffusion), *Control* Solution

Term	Multiplies	Sub-term	Scaled Value [deg day^{-1}]
		$g_3(\mathbf{x}^*)$	−3.81
λ_{31}	δs	Evaporation efficiency	−0.20
		Soil heat capacity	0.08
		Sum	−0.12
λ_{32}	δq_m	Vapor deficit in potential evaporation	0.10
λ_{33}	δT_g	Saturation specific humidity in potential evaporation	−0.53
λ_{34}	$\delta \theta_m$	(does not appear)	0.00
λ_{35}	$\delta \Delta$	Gradient in sensible heat flux	−0.31

In this Section, the analysis is extended to the investigation of these same feedbacks and interactions not only near the equilibrium point, but also at locations in state variable phase-space representing anomalies in climatic conditions. Examples of such anomalies are hydrologic droughts and wet periods. How effective are these same feedbacks and interactions when the general conditions are characterized by a hydrologic dry anomaly? Or wet anomalies?

Because the focus here is on the land surface, we shall continue to define the anomaly states in terms of hydrologic dry and pluvial periods. As in Chapter 4, a hydrologic drought condition (Dry Anomaly) is defined as when the soil moisture state (s) is at or below the fifth percentile on its probability distribution. The Moist Anomaly is defined as when the soil moisture is at or above the ninety-fifth percentile. The probability distribution is defined by the integration of equation (5.1). There is significant covariance between the model states that come about due to the routing of external white-noise forcing through the physical linkages in the balance model (Chapter 3). Thus the conditions of the three remaining state variables must be weighted according to the joint probability distribution for the system when considering any measure (such as Λ_{ij} and λ_{ij}) evaluated at the Dry or Moist soil moisture anomaly states.

In this Section, the normalized tendencies to restore or reinforce anomalies in soil moisture and temperature are evaluated for both Dry and Moist anomalies. For the sake of limiting the length of presentation, only the overall contributions from Λ'_{ij}s and λ'_{ij}s (and not the component-by-component contributions as in Section 5.5) are

Table 5.6: Terms in G_1 (Soil Moisture Drift), *Control* Solution

		Dry Anomaly		Moist Anomaly	
j	Variable	$E[\delta_j]$ [ ]	$\Lambda_{1j}E[\delta_j]$ [mm day^{-1}]	$E[\delta_j]$ [ ]	$\Lambda_{1j}E[\delta_j]$ [mm day^{-1}]
1	s	−1.15	0.74	1.05	−0.67
2	q_m	1.21	0.12	−0.96	−0.10
3	T_g	1.09	−0.58	−1.02	0.54
4	θ_m	1.25	0.00	−1.11	0.00
5	Δ	0.34	−0.07	−0.37	0.08
	Linearized G_1		0.21		−0.15
	E[Nonlinear G_1]		0.19		−0.16

presented.

The approximate G_1, G_3, g_1, and g_3 functions according to equations (5.5) and (5.9) are tabulated in Tables 5.6 through 5.9, respectively. Table 5.6, which presents the analysis of the soil moisture drift function, G_1, will be discussed in detail; the format of the other tables is identical. The expected value of each disequilibrium $\delta_j = E[x_j - x_j^*]$ at an anomalous state is computed from the stationary conditional probability density functions and non-dimensionalized by the respective stationary standard deviation (these are often termed Z-scores in statistical analysis). The product $\Lambda_{ij}E[\delta_j]$ is given for each of the four state disequilibria and Δ. As a product of terms, a large entry can result from either a large Λ_{ij} or a large δ_j, or both. The terms are summed to give the result in the line "Linearized G_1." To judge the adequacy of the truncated Taylor series approximation, the actual conditional expectation of G_1 given the anomalies, listed as "E[Nonlinear G_1]," gives the value computed from the nonlinear stochastic solution.

The Dry anomaly represents a soil moisture disequilibrium of $-1.15\sigma_s$ (Table 5.6). High soil temperature is associated with dry soil, thus the expected T_g disequilibrium is $1.09\sigma_T$. The restoring term multiplying δs is large and negative; the product of a negative restoring Λ_{11} and negative δs gives a positive (moistening) contribution to the deterministic evolution of s (G_1). Thus the soil water balance which constitutes $\Lambda_{11}E[\delta_1]$ is a self-restorive system, with negative feedbacks built into it. However, the coupling term Λ_{13} multiplying $E[\delta T_g]$ is also large and negative; when multiplying the positive (warm) δT_g, it gives a negative (drying) contribution to G_1. The coupled energy balance for the land surface contributes to the terms in $\Lambda_{13}E[\delta_3]$, and it serves

Table 5.7: Terms in G_3 (Soil Temperature Drift), *Control* Solution

		Dry Anomaly		Moist Anomaly	
j	Variable	$E[\delta_j]$ [ ]	$\Lambda_{3j}E[\delta_j]$ [° day^{-1}]	$E[\delta_j]$ [ ]	$\Lambda_{3j}E[\delta_j]$ [° day^{-1}]
1	s	−1.15	1.02	1.05	−0.93
2	q_m	1.21	−0.09	−0.96	0.07
3	T_g	1.09	−4.15	−1.02	3.90
4	θ_m	1.25	1.12	−1.11	−1.00
5	Δ	0.34	−0.75	−0.37	0.81
	Linearized G_3		−2.85		2.87
	E[Nonlinear G_3]		−2.64		2.32

as a positive feedback on soil moisture anomalies. Table 5.6 shows that in this case — the evolution of soil moisture anomalies — the soil water balance constitutes a negative feedback, but the coupled energy balance provides for an almost equal strength positive feedback, which serves to enhance and intensify the dry anomaly. At the positive soil moisture anomaly state (Moist anomaly in Table 5.6), the roles of the water and energy balance in constituting feedbacks also work in opposite directions.

For the Dry Anomaly in Table 5.6, a moist (positive) specific humidity anomaly (δ_2) multiplies a positive Λ_{12}, a moistening effect due to the decreased vapor gradient in potential evaporation. A positive temperature gradient disequilibrium, $E[\delta_5]$, multiplying a negative Λ_{15} contributes further drying, due to the enhanced turbulent fluxes. As a result of these competing influences — mostly that of soil temperature — the soil moisture's self-restoring tendency 0.74 mm day^{-1} is reduced to less than one-third of its strength. The exact reverse occurs for the moist anomaly, where a cool disequilibrium in T_g reduces the evaporative demand, contributing to moistening and opposing the restoring term's drying effect.

For the soil temperature drift (G_3) from anomalously dry and moist states (Table 5.7), we see the contribution of a strong T_g restoring term, Λ_{33} being counteracted by both the s and θ_m contributions. In the warm-dry case, reduced soil moisture inhibits cooling by suppressing evaporation. It thus contributes a positive feedback on the soil temperature anomaly evolution. Increased mixed-layer air temperature (θ_m disequilibrium of $1.25\sigma_\theta$) in the dry-soil case also suppresses cooling by reducing the sensible heat flux in addition to warming the soil by longwave radiation.

The diffusion functions (g_i) multiply the random noise in (5.1) and thus allow the

Table 5.8: Terms in g_1 (Soil Moisture Diffusion), *Control* Solution

		Dry Anomaly		Moist Anomaly	
j	Variable	$E[\delta_j]$ [ ]	$\lambda_{1j}E[\delta_j]$ [mm day^{-1}]	$E[\delta_j]$ [ ]	$\lambda_{1j}E[\delta_j]$ [mm day^{-1}]
1	s	−1.15	0.20	1.05	−0.18
2	q_m	1.21	0.03	−0.96	−0.02
3	T_g	1.09	−0.12	−1.02	0.11
4	θ_m	1.25	0.00	−1.11	0.00
5	Δ	0.34	0.00	−0.37	0.00
	$g_1(\mathbf{x}^*)$		0.52		0.52
Linearized g_1			0.63		0.43
E[Nonlinear g_1]			0.61		0.41

system state at the time of the perturbation to control the effect of the perturbation on each state. The perturbations are zero-mean and can be either positive or negative with equal probability. The fact that g_1 is positive means that a positive perturbation (above-average wind-speed) contributes a moistening effect to whatever deterministic drift is happening at the time, as set by the average wind speed and system state, and a negative perturbation (below-average wind-speed) contributes a drying effect to the instantaneous deterministic drift.

The weighting terms, the non-dimensional disequilibria, and their products corresponding to the soil moisture diffusion function (g_1) are tabulated and summed in Table 5.8. The nonzero additional term $g_1(\mathbf{x}^*)$ must be included in estimating $g_1(\mathbf{x})$. The soil moisture state is, on average, more susceptible to random perturbations at the Dry anomaly than at the Moist anomaly. As in the soil moisture drift, the moisture anomaly δs and the soil temperature anomaly δT_g are in competition to determine g_1, in both the dry and wet cases; they constitute opposite-sign feedbacks.

The soil temperature state is also more sensitive to diffusion when the system is anomalously dry than when it is anomalously moist (Table 5.9). The sign of g_3 is negative, indicating that an above-average wind-speed adds a cooling influence in addition to the deterministic drift at the time, and a below-average wind-speed a warming influence. Once again, the influences of the temperature and moisture disequilibria are of opposite sign. However, in the case of g_3 (ground temperature response to random fluctuations), the magnitude of the soil-moisture contribution $\lambda_{31}\delta s$ is about 25 percent of the soil temperature contribution $\lambda_{33}\delta T_g$, whereas for g_1

Table 5.9: Terms in g_3 (Soil Temperature Diffusion), *Control* Solution

		Dry Anomaly		Moist Anomaly	
j	Variable	$E[\delta_j]$ [ ]	$\lambda_{3j}E[\delta_j]$ [° day^{-1}]	$E[\delta_j]$ [ ]	$\lambda_{3j}E[\delta_j]$ [° day^{-1}]
1	s	−1.15	0.14	1.05	−0.13
2	q_m	1.21	0.12	−0.96	−0.10
3	T_g	1.09	−0.58	−1.02	0.54
4	θ_m	1.25	0	−1.11	0
5	Δ	0.34	−0.10	−0.37	0.11
	$g_3(\mathbf{x}^\star)$		−3.81		−3.81
	Linearized g_3		−4.23		−3.38
	E[Nonlinear g_3]		−4.33		−3.48

(soil moisture response to random fluctuations, Table 5.8) the magnitude of the soil temperature contribution is almost two-thirds that of the soil moisture contribution. This means that the temperature state does more to moderate the system's moisture susceptibility to noise than vice versa.

The drift and diffusion functions are linearized around $\mathbf{x}^\star$ in this analysis; thus the weighting terms Λ_{ij} and λ_{ij} take the same sign and value for soil moisture anomalies of either sign. Therefore, any asymmetries between the Dry and Moist anomalies, in terms of how the states contribute to negative or positive feedback, must be due to the magnitude of the states' disequilibrium.

First, examining the various contributions to soil moisture drift (G_1, Table 5.6), because the Dry anomaly is slightly more disequilibrated than the moist anomaly, the magnitude of the self-restoring negative feedback is larger on the dry side. However, the ground temperature is also more disequilibrated for the Dry anomaly than for the Moist one, contributing a stronger positive feedback on the Dry side. In this particular case, the stochastic *Control* solution, the net result is a slightly stronger restoring force for the Dry anomaly. For soil temperature drift (G_3, Table 5.7), the various products $\Lambda_{ij}E[\delta_j]$ sum to give nearly equal contributions to G_3 at the two anomalies, although considered separately, each variable (except Δ) contributes a stronger positive or negative feedback on the Dry side, due to the variables' greater disequilibrium when the soil moisture is anomalously dry. As a result, for the *Control* solution, the deterministic (no-noise) trajectories from these anomalies to $\mathbf{x}^\star$ are nearly symmetric (Figure 4-9)

In this particular application, the deterministic positive and negative feedback effects of the system states upon each other balance in such a way that there is not a strong asymmetry between the system's (s, T_g) recovery behavior from dry-warm and moist-cool anomalies. However, from Tables 5.6 and 5.7, one can see how asymmetric behavior might arise, depending upon the correlation structure of the states.

All else being equal, a much larger temperature disequilibrium (δT_g) corresponding to the Dry anomaly would strengthen the positive feedback, $\Lambda_{13} E[\delta_3]$, perhaps even causing further drying before recovery to normal. This behavior was observed in the *Two-regime-β* case in Chapter 4. In that solution, due to the stronger negative correlation between soil moisture and temperature in the soil-controlled evaporation regime, temperature is greatly more disequilibrated at the Dry anomaly than at the Moist anomaly. As a result, when deterministically recovering from the warm-dry anomaly, the system cools and dries first before recovering to equilibrium soil moisture (Figure 4-10).

The differences in susceptibility to noise between the Dry and Moist anomalies in the *Control* solution (Tables 5.8 and 5.9) apparently do not contribute differences in the time to recover to normal soil moisture, as explored in Chapter 4. This is due to the fact that the noise is modeled as white; at any point in time and state-space, the noise can take either sign with equal probability. Thus, for a given point in state-space, a cooling-moistening perturbation (positive noise) is as likely as a warming-drying one (negative noise). Any persistence in the noise could introduce noticeably different behavior; for example, if a warming-drying perturbation is more likely to be followed by continued perturbations of the same sign, the consequences would be greater in the warm-dry sector, where the system is more susceptible to noise. In addition, the stronger the (s, T_g) correlation, the stronger the competition between these two states to determine the sign and magnitude of the response to random fluctuations.

5.7 Conclusions and Discussion

A basic linearization technique has been combined with a model of two–way land–atmosphere interaction incorporating coupled water and energy balance, to analyze how and why feedback mechanisms arise in the coupled moisture and temperature states at the land surface and in the lower atmosphere. The findings include the observation that anomalous moisture and temperature states affect each other so as to create mutual positive feedbacks. The contribution of this analysis is to quantify the pathways of those feedbacks. The stochastic solution gives a physically consistent

probability density function, incorporating realistic covariances among the states by means of drift and diffusion functions that describe, respectively, the system's simultaneous state-dependent tendency to equilibrate and state-dependent susceptibility to random perturbations. The resulting correlations are then taken into account when anomalous moisture states are selected for truncated Taylor Series analysis.

Decomposition of the drift and diffusion functions into the dependence of each of their component physical processes upon each of the model states shows that:

- Soil-moisture control of infiltration and of evaporation efficiency are self-restoring forces of comparable strength for the soil moisture state.

- The temperature dependence of surface saturation specific humidity is a major factor in enhancing, or delaying recovery from, soil moisture anomalies.

- The individually strong effects of atmospheric humidity on ground temperature take opposite signs and cancel one another.

- Soil-moisture control of evaporation efficiency is the major mechanism by which the moisture state enhances, or slows recovery from, temperature anomalies.

- The temperature dependence of surface saturation specific humidity is a major self-restoring factor for the temperature state and it exceeds the thermal radiation factor.

- The buoyancy velocity is a significant recovery factor for temperature anomalies because it affects both the soil temperature and its coupling to air temperature. Soil temperature is positively correlated with temperature gradient anomalies; when the soil is anomalously warm, a strong gradient that enhances cooling also tends to be present.

- Both soil temperature and soil moisture tend to be more susceptible to random perturbations when the soil is dry than when it is moist. This is due, as in the deterministic drift, largely to temperature-dependent saturation specific humidity and to soil-moisture control of evaporation efficiency and infiltration.

The fundamental result of this model study is that the soil moisture and soil temperature states are negatively correlated (cool-moist or warm-dry), and that these states communicate their covariability partially through local-scale interaction with the near-surface atmosphere. Because of the negative correlation between the states,

the physical mechanisms that serve as restoring forces for each state individually (soil-moisture control of evaporation and temperature-dependence of saturation specific humidity) act as anomaly-enhancing positive feedback mechanisms for the other state.

Chapter 6

Discussion

6.1 Major Findings

The results of each phase of this work (model development, stochastic extension, recovery from anomalies, and analysis of feedbacks) are summarized in Chapters 2, 3, 4, and 5, respectively. The following is a summary of the principal results.

- The 4–state stochastic model results in a physically consistent covariability response for the moisture and energy states in the land–atmosphere system due to the state–dependent turbulent and radiative fluxes.

- *Two–way* land–atmosphere coupling is critical in establishing the memory and covariability of the soil moisture and temperature states.

- Water-energy coupling at the land surface results in the presence of positive soil moisture feedbacks (anomaly-enhancing mechanisms) that are not evident if the water balance is considered alone. These positive feedbacks exist due to the role of evaporation in balancing both the hydrologic and the energy balance, and because evaporation is a product, $E = E_p\beta$, where β increases with s, and E_p with T_g. Because of the negative correlation between these two states, the physical mechanisms that serve as restoring forces for each state individually (soil-moisture control of evaporation and temperature-dependence of surface saturation specific humidity) act as anomaly-enhancing positive feedback mechanisms for the other state.

- Longer recovery times to normal soil moisture are more probable from a dry anomaly than from a moist anomaly when evaporation efficiency is formulated

such that evaporation switches between soil and atmosphere control. This asymmetry arises from a stronger correlation between soil moisture and soil temperature in the soil-controlled regime.

- Quantitative decomposition of the drift and diffusion functions into the dependence of each of their component physical processes upon each of the model states shows that:
  - the temperature dependence of surface saturation specific humidity is a major factor in enhancing, or delaying recovery from, soil moisture anomalies;
  - reciprocally, soil-moisture control of evaporation efficiency is the major mechanism by which the moisture state enhances, or slows recovery from, temperature anomalies;
  - the temperature dependence of saturation specific humidity is a major self-restoring factor for the temperature state, and it exceeds the thermal radiation factor; and
  - the buoyancy velocity (representing free convection) is a significant recovery factor for temperature anomalies because it affects both the soil temperature and its coupling to air temperature.
- Both soil temperature and soil moisture tend to be more susceptible to random perturbations from the mean wind speed when the soil is dry than when it is moist.
- Disequilibria and anomalies first quickly restore to an equilibrium land–atmosphere temperature gradient through sensible heat flux, then approach the overall equilibrium state through the interaction of the remaining coupling mechanisms.

6.2 Future Research Directions

This thesis demonstrates the versatility and utility of the simplified model for analyzing and understanding land-atmosphere interaction. The current form of the model contains a number of assumptions that could be relaxed to make the results even more physically realistic. Among these are:

- **Land–surface evaporation control.** Many of the findings in Chapters 3, 4 and 5 result from the formulation of actual evaporation as a product of potential evaporation $E_p(T_g, q_m, \theta_m)$ and evaporation efficiency $\beta(s)$. Chapter 4 shows that the functional form of $\beta(s)$ strongly controls the stationary probability distribution of the states and results in noticeable asymmetries between the persistence behavior of dry and moist anomalies. In contrast to "β" formulations of actual evaporation, "α"-type formulations calculate an actual vapor pressure at the soil surface, usually relating surface specific humidity to soil moisture; with an explicit moisture gradient in the surface sublayer, the concept of potential evaporation does not need to be invoked. (Mahfouf and Noilhan, 1991, discuss the different approaches.) Obviously, the model solution would be different with an "α" formulation of evaporation rather than the present "β" formulation. However, the use of a "β" formulation shows promise for bulk characterization of large regions, possibly avoiding the problem of spatial heterogeneity posed by the "α" methods.

- **Time–invariant boundary–layer height.** In accordance with the discussion in Section 2.2.5, the air-slab heat and moisture capacities and longwave radiation fluxes would become much more variable. In response to such a change, reduction in soil-air thermal coupling might be observed: as the mixed-layer grows in response to surface sensible heat flux, it increases its heat capacity and may experience less change in its potential temperature in response to anomalous surface heating. On the other hand, boundary-layer growth implies the entrainment of potentially warmer air from the overlying atmosphere, an effect which may counteract that of the changing heat store; since the entrainment of warm air from above is already parameterized in the current model, this effect of variable h would probably be small.

- **Incessant precipitation.** The range of variation in soil moisture is small. This is believed to result from the fact that precipitation is continuous in the model, and therefore that dry-down periods — and true *drought* conditions — are not present in the solutions.

- **Single soil layer.** A second (deep) soil moisture reservoir would add more memory to the soil water balance. If a thin surface layer were included, functions (such as albedo) that depend on surface — rather than soil–layer — moisture conditions would be more realistically evaluated.

- **Gaussian noise.** Due to the assumption that the random forcing has a gaussian marginal distribution, the variance parameter σ_u may only be increased to the level (with respect to the mean $\overline{U}$) such that negative wind-speeds (a physical impossibility) are probabilistically very infrequent. This constrains the ability to investigate the effects of increased variance in the noise on the states' joint and marginal distributions.

  In fact, the constraint of gaussianity on the noise is the reason for incessant precipitation in this model. Theory exists for shot noise (i.e., Poisson processes) in systems of stochastic equations similar to the Îto equation [equation (3.5)]; such a formulation for precipitation could be used to make the model's hydrologic forcing more realistic by allowing dry-down periods.

- **White noise.** Colored (temporally–correlated) noise is fairly easily incorporated into the model by adding an additional state equation for the physical forcing term (Palleschi and de Rosa 1992), in this case, wind speed. As discussed in Section 5.6, it is expected that such persistence in the forcing would enhance differences between the system's recovery from warm and dry anomalies.

- **Univariate noise.** The model construct allows any number of forcing noise terms, that is a vector $\mathbf{dw}_t$ in equation (3.5). Instead of introducing random perturbations through the wind speed alone, as in this application, randomness could be formulated as entering through the incoming specific humidity (q_{in}) or sensible heat advection (θ_{in}) or both. It would be possible, using three terms for $\mathbf{dw}_t$, to force the system with gaussian moisture advection and sensible heat advection having a specified covariance structure.

In the other direction, continued insight might be derived from further simplifications of the model to make it yet more tractable. Gardiner (1985) notes the difficulty of analytically solving the multivariate Fokker-Planck equation [equations (4.1) and (4.6)] for systems that do not satisfy detailed balance (essentially a reversibility of probability flow). This 4–state model does not satisfy that condition; indeed, it may be impossible to represent land–atmosphere interaction in such a way. Nonetheless, an analytic solution to a simplified version of the model might be possible; because of the critical role of two-way land–atmosphere interaction in communicating variability between soil moisture and soil temperature, at least three states are necessary.

The results in Chapter 4 suggest an intriguing application of this model to large–scale land–surface observations. The bivariate probability histograms of s and T_g in the model solutions [*Control* and *Two-Regime* β] tend to follow the shapes of their respective β functions (Figures 4-7 and 4-8). To the extent that this model is representative of water and energy fluxes in land–atmosphere interaction, this result indicates that it may be possible to estimate evaporation efficiency functions for large land regions on the basis of joint probability histograms of remotely-sensed large-scale soil moisture and temperature. As time-series of such large-footprint observations are developed, they may be used to validate the temporal correlation structure among the soil moisture, soil temperature, air humidity, and air temperature for land regions.

6.3 Discussion

The further development and extensions of this and similar simple models, in conjunction with observational studies and numerical atmospheric modeling, form a hierarchy of tools at various levels of detail. Such multi-level analysis of the land–atmosphere system is needed, because the complex interconnectedness of processes and their action at a multitude of scales require diverse perspectives and vantage points.

The analyses derived based on such class of simplified analytic models may be used to focus on specific processes that are established to be relevant and influential. The gain in understanding may then be used to design guided experiments for numerical atmospheric models (mesoscale or global primitive equation models). These numerical models contain the major large-scale feedbacks in more detail and they are spatially-distributed.

An approach in the reverse direction is also recommended. Numerical (atmospheric) models may be used to identify key interactions that are considered to essentially capture the role of land processes on climate variability. The analytical model and its stochastic extension may then be used to explore the long-term statistical behavior of the system. Whereas numerical atmospheric models are computationally burdensome and limited by sampling shortcomings, the analytic-stochastic approach yields robust statistical and probabilistic measures of variability.

The final and most important use of both these modeling approaches is to guide field observations of the processes. Sampling strategies may be optimized once the character and space–time scales of feedback interactions and their constituitive components are identified. In turn, observations are used to build and verify modeling components and process representations. Limited sources of observations on land-

atmosphere interaction currently exist; integrated and simultaneous measurements of heat and moisture content of the soil and atmosphere, and surface fluxes, are available for short periods over small areas (*e.g.* intensive field campaigns associated with the FIFE, HAPEX, and other hydrologic and micrometeorologic experiments). These field observations may be used to verify the model's process representations such as land–surface control of evaporation, inversion–base heat and moisture entrainment, and advective fluxes. However, the time scale of the stochastic model is not compatible with the relatively short duration of these field experiments; months, or even a few years, of observations are not sufficient to characterize the statistics of moisture and temperature states. An integrated approach using observed data and a hierarchy of modelling approaches is needed.

Appendix A

List of Symbols

Symbol	Definition	Units
A	empirical coefficient in longwave emissivity formulation	$[\mathrm{cm}^{-1/7}]$
A_{top}	empirical coefficient in expression for sensible heat entrainment at slab top	[ ]
a	scaled amount of (mainly water vapor) mass in air column between p_{h} and p_{s}	[cm]
Bo	surface Bowen ratio $H/\lambda E$	[ ]
b	partitioning parameter — fraction of incoming water vapor that moistens the air slab; the remainder precipitates	[ ]
B_1, B_2	empirical constants in RS	[ ]
C_1, C_2	empirical constants in turbulent transfer coefficient	[ ]
C_{HE}	transfer coefficient for surface turbulent fluxes	$[\mathrm{m\ s}^{-1}]$
C_{pa}	dry-air specific heat at constant pressure	$[\mathrm{J\ kg}^{-1}\ \mathrm{deg}^{-1}]$
C_{soil}	soil layer bulk heat capacity	$[\mathrm{J\ m}^{-3}\ \mathrm{deg}^{-1}]$
c	exponent in evaporation efficiency	[ ]
d_{m}/d	ratio of mean to instantaneous earth-sun distance	[ ]
dw_t	differential of the Wiener process (white noise)	
E	evaporation from the soil into the air slab	$[\mathrm{kg\ s}^{-1}\ \mathrm{m}^{-2}]$
EF	evaporative fraction	[ ]
E_{p}	potential evaporation	$[\mathrm{kg\ s}^{-1}\ \mathrm{m}^{-2}]$

f_s	stationary probability density function	[ ]
$\mathbf{G}$	deterministic drift function	—
$\mathbf{g}$	diffusion function	—
G	heat flux into soil layer	[W m^{-2}]
g	acceleration of gravity	[m s^{-2}]
H	turbulent flux of sensible heat from soil to air slab	[W m^{-2}]
H_o	half-day hour angle	[rad]
H_{in}	lateral advection of sensible heat into the region	[W m^{-2}]
H_{out}	lateral advection of sensible heat out of the region	[W m^{-2}]
H_{top}	turbulent entrainment of sensible heat at air-slab top	[W m^{-2}]
h	height of mixed-layer	[m]
K	empirical longwave correction for cloudiness	[ ]
L	length scale of region	[m]
M	mixed–layer air mass per unit width	[kg m^{-1}]
m	empirical exponent in longwave emissivity formulation	[ ]
N_c	fraction of sky covered by cloud	[ ]
N_s	ratio of actual to total possible hours of sunshine	[ ]
n	soil porosity	[ ]
P	precipitation	[mm day^{-1}]
p	atmospheric pressure	[mb]
p_h	atmospheric pressure at air slab top	[mb]
p_s	atmospheric pressure at surface (defined as 1000 mb)	[mb]
p_{ref}	reference pressure in θ_m	[mb]
Q_{in}	water vapor laterally advected into the region	[mm day^{-1}]
Q_{out}	water vapor laterally advected out of the region	[mm day^{-1}]
q^*	saturation specific humidity	[(g H_20) (kg air)$^{-1}$]
q_{in}	effective specific humidity of incoming air	[(g H_20) (kg air)$^{-1}$]
q_m	model mixed–layer specific humidity	[(g H_20) (kg air)$^{-1}$]

R	surface and subsurface runoff	[mm day^{-1}]
R_{d}	gas constant for dry air	[J kg^{-1} deg^{-1}]
RH_{surf}	relative humidity of near-surface air	[ ]
RL_{ad}	downwelling thermal (longwave) radiation flux density at top of mixed layer	[W m^{-2}]
RL_{gu}	upwelling thermal (longwave) radiation flux density from the soil surface	[W m^{-2}]
RL_{sd}	downwelling thermal (longwave) radiation flux density from the mixed layer	[W m^{-2}]
RL_{sdc}	clear-sky downwelling thermal (longwave) radiation flux density from the mixed layer	[W m^{-2}]
RL_{su}	upwelling thermal (longwave) radiation flux density from the mixed layer	[W m^{-2}]
RL_{suc}	clear-sky upwelling thermal (longwave) radiation flux density from the mixed layer	[W m^{-2}]
RS	solar (shortwave) radiation flux density at soil surface	[W m^{-2}]
$RS\mathrm{e}$	solar (shortwave) radiation flux density at top of atmosphere	[W m^{-2}]
r	exponent in runoff parameterization	[ ]
s	model relative soil saturation (soil moisture)	[ ]
s_{05}, s_{50}, s_{95}	stationary 5^{th}, 50^{th} (median) and 95^{th} percentiles of soil moisture	[ ]
T	temperature	[deg]
T_{g}	model soil layer temperature	[deg]
T_{h}	temperature at height h (top of mixed layer)	deg
$T_{\mathbf{x}\to\mathcal{B}}$	first-passage time from $\mathbf{x}$ over state-space boundary $\mathcal{B}$	[time]
U_{z}	mixed layer wind speed	[m s^{-1}]
$\overline{U}$	mean mixed–layer wind speed	[m s^{-1}]
$v_{\mathrm{min}}, v_{\mathrm{org}}$	volume fractions of mineral and organic matter in the soil	[ ]
w_{B}	buoyancy velocity scale	[m s^{-1}]
X_c	Correction for cloud in longwave radiation	[ ]

$\widehat{x}$	model climatic equilibrium solution	—
$\langle x \rangle$	model equlibrium solution with diurnal solar forcing	—
$x^\star$	model equilibrium solution with daily–averaged solar forcing	—
Y_c	correction for cloud in shortwave radiation	[ ]
Z_h	hydrologically active soil depth	[m]
Z_t	thermally active soil depth	[m]
z	height variable	[m]
α	soil-surface albedo	[ ]
β	evaporation efficiency	[ ]
Δ	surface sublayer temperature gradient $T_\mathrm{g} - \theta_\mathrm{m}$	[deg C]
$\Delta\theta$	jump in potential temperature at top of mixed layer	[deg]
$\Delta\theta_\mathrm{v}$	difference in virtual potential temperature between near-surface and mixed-layer	[deg]
δ	solar inclination angle	[rad]
δx	non-dimensional disequilibrium in variable x	—
$\epsilon^\uparrow, \epsilon^\downarrow$	effective emissivities of the mixed layer for upwelling and downwelling longwave radiation	[ ]
$\epsilon_\mathrm{effective}$	effective emissivity of the atmosphere above the mixed layer	[ ]
ϵ_col	bulk longwave emissivity/absorptivity of the mixed layer	[ ]
ε	coefficient in runoff parameterization	[ ]
θ	potential temperature	[deg]
θ_m	model air-slab potential temperature	[deg]
θ_o	solar zenith angle	[rad]
θ_v	virtual potential temperature	[deg]
$\overline{\theta' w'}_\mathrm{h}$	turbulent sensible heat flux at top of mixed layer (correlation between potential temperature and vertical air motion)	[deg m s^{-1}]

Λ_{ij}	linear coefficient for effect of state variable j on variable i in drift	—
λ_{ij}	linear coefficient for effect of state variable j on variable i in diffusion	—
λ	latent heat of vaporization of water	[J kg^{-}1]
λ_{o}	latitude	[rad]
ρ	air density	[kg m^{-3}]
ρ_{w}	density of liquid water	[kg m^{-3}]
σ	Stefan-Boltzmann constant	[W m^{-2} deg^{-4}]
σ_{x}	stationary standard deviation of variable x	—
σ_{u}	standard deviation of mixed–layer wind speed	[m s^{-1}]
φ	runoff ratio (runoff/precipitation)	[ ]

Appendix B

Longwave Radiation

B.1 Contribution of the Mixed Layer

We apply a broad-band, plane-parallel slab emissivity formulation to estimate the clear-sky longwave radiation from the mixed layer, following Brutsaert (1975), as adjusted to incorporate our assumption of constant potential temperature and specific humidity in the mixed layer. For a mixed layer extending to height h, we wish to find RL_{su} and RL_{sd} (see Fig. 2-1). Consider first the upward flux,

$$RL_{su} = \int_{a=0}^{a(h)} \pi B(T) \frac{\partial \epsilon_c(1.66a, T)}{\partial a} da \tag{B.1}$$

where $B(T) = \sigma T^4/\pi$, and ϵ_c is the column emissivity; in (B.1), a is the scaled amount of (mainly water vapor) mass in the air column measured downward from h. The water vapor mass is scaled for the pressure effect following

$$da = \rho_v \left(\frac{p}{p_s}\right)^{1/2} dz \tag{B.2}$$

(Brutsaert 1975), where ρ_v is the water vapor density, and p and p_s are the pressures at z and at the surface, respectively. Assuming a hydrostatic atmosphere and transforming to pressure as the vertical coordinate, $dp = -\rho g\, dz$, where ρ is the density of air at level z, and g is the acceleration of gravity, measuring a downward from $z = h$ (i.e., from $p = p_h$) to $p(z)$, and invoking the model assumption that $q_m = \rho_v/\rho$ is constant in the slab,

$$a(p, p_h) = \frac{2}{3}\frac{q_m p_s}{g}\left[\left(\frac{p}{p_s}\right)^{3/2} - \left(\frac{p_h}{p_s}\right)^{3/2}\right] \tag{B.3}$$

The bracketed term lies in the range $[0,1]$ since $p_h \leq p \leq p_s$. From Brutsaert (1975), the emissivity is

$$\epsilon_s(a) = \epsilon_c(1.66a) = Aa^m. \tag{B.4}$$

Brutsaert suggests $A = 0.75$ and $m = 1/7$, for a in cm. Substituting (B.4) into (B.3),

$$\frac{\partial \epsilon}{\partial a} = Ama^{m-1} = mA\left(\frac{2}{3}\frac{q_m p_s}{g}\right)^{m-1}\left[\left(\frac{p}{p_s}\right)^{3/2} - \left(\frac{p_h}{p_s}\right)^{3/2}\right]^{m-1} \tag{B.5}$$

Equation (B.1) is reassembled with the terms appropriate to the constant-θ_m mixed layer:

$$RL_{su} = \sigma\theta_m^4 mA\left(\frac{2}{3}\frac{q_m p_s}{g}\right)^m \int_{p_s}^{p_h}\left(\frac{p}{p_s}\right)^{4\frac{R_d}{C_p}}\left[\left(\frac{p}{p_s}\right)^{3/2} - \left(\frac{p_h}{p_s}\right)^{3/2}\right]^{m-1}\frac{3}{2}\left(\frac{p}{p_s}\right)^{1/2}\frac{dp}{p_s} \tag{B.6}$$

The integral in (B.6) may be simplified using the change of variable, $y = \left(\frac{p}{p_s}\right)^{3/2}$. Thus,

$$RL_{su} = \sigma\theta_m^4 mA\left(\frac{2}{3}\frac{q_m p_s}{g}\right)^m \int_{y_h}^{1} y^{\frac{8}{3}\frac{R_d}{C_p}}[y - y_h]^{m-1}dy. \tag{B.7}$$

Similarly, for the downward flux at $z = 0$, a is measured upward from $z = 0$ (i.e., from $p = p_s$) to $p(z)$,

$$a(p_s, p) = \frac{2}{3}\frac{q_m p_s}{g}\left[1 - \left(\frac{p}{p_s}\right)^{3/2}\right] \tag{B.8}$$

Again, the bracketed term lies in the range [0,1] because $p \leq p_s$. For the downward flux, (B.1) becomes

$$RL_{sd} = \sigma\theta_m^4 mA\left(\frac{2}{3}\frac{q_m p_s}{g}\right)^m \int_{y_h}^{1} y^{\frac{8}{3}\frac{R_d}{C_p}}(1-y)^{m-1}dy. \tag{B.9}$$

Equations (B.7) and (B.9) have the form

$$RL_{su} = \sigma\theta_m^4\epsilon^{\uparrow} \tag{B.10}$$

$$RL_{sd} = \sigma\theta_m^4\epsilon^{\downarrow} \tag{B.11}$$

where $\epsilon^{\uparrow}$ and $\epsilon^{\downarrow}$ are effective upward and downward clear-sky emissivities for the mixed-layer air slab, given by

$$\epsilon^{\downarrow} = q_m^m\left\{mA\left(\frac{2}{3}\frac{p_s}{g}\right)^m \int_{y_h}^{1} y^{\frac{8}{3}\frac{R_d}{C_p}}(1-y)^{m-1}dy\right\}$$

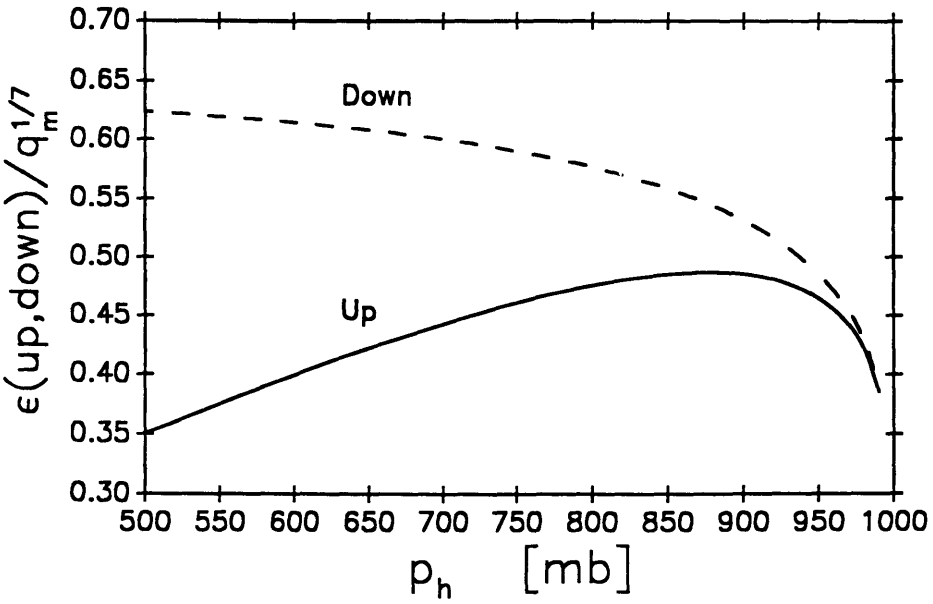

Figure B-1: The term that multiplies $q_{\rm m}^m$ in the upward and downward longwave bulk emissivities of the air slab.

$$\text{and} \qquad \epsilon^{\uparrow} = q_{\rm m}^m \left\{ mA \left(\frac{2}{3} \frac{p_{\rm s}}{g} \right)^m \int_{y_{\rm h}}^1 y^{\frac{8}{3}\frac{R_{\rm d}}{C_{\rm p}}} (y - y_{\rm h})^{m-1} \, dy \right\} . \tag{B.12}$$

The integrals in (B.12) are smooth functions of one variable, $y_{\rm h}$, $0 < y_{\rm h} < 1$, which are evaluated once by numerical integration for each application (Figure B-1).

B.2 Contribution of the Overlying Atmosphere

The downwelling longwave flux density from the overlying atmosphere at height h is given by

$$RL_{\rm ad} = \int_{a=0}^{\infty} \pi B(T) \frac{\partial \epsilon_{\rm c}(1.66a, T)}{\partial a} da \, , \tag{B.13}$$

measuring a upward from $z = h$. Brutsaert (1975) solved (B.13) at $z = 0$; we apply the same solution at $z = h$ to obtain $RL_{\rm ad}$ in terms of the model states. We assume the following profiles for water vapor density, temperature, and pressure above the mixed layer:

$$\rho_{\rm v}(z) = \frac{\epsilon_0 e_{\rm h}}{R_{\rm d} T_{\rm h}} \exp\left[-k_{\rm v}(z - h)\right] \tag{B.14}$$

$$T(z) = T_{\rm h} \exp\left[-\frac{\gamma}{T_0}(z - h)\right] \tag{B.15}$$

$$p(z) \;=\; p_{\rm h} \exp\left[-\frac{g}{R_{\rm d}T_0}(z-h)\right] \tag{B.16}$$

where $(\gamma/T_0)^{-1}$ is a scale height for temperature, $(k_{\rm v})^{-1}$ for vapor density, and $(g/R_{\rm d}T_0)^{-1}$ for pressure, $T_{\rm h}$ is the actual temperature at the top of the slab (Eq. 2.12), and T_0 is a reference surface temperature. Integration of (B.13) using the assumed profiles results in

$$RL_{\rm ad} = \sigma T_{\rm h}^4 m A \left(\frac{\epsilon_0 e_{\rm h}}{k_2 R_{\rm d} T_{\rm h}}\right)^m B\left(\frac{k_1}{k_2}, m\right) , \tag{B.17}$$

where $k_1 = (4\gamma/T_0 + k_2)$ and $k_2 = (k_{\rm w} + g/2R_{\rm d}T_0)$, and $B(\;\;)$ is the beta function [e.g. Abramowitz and Stegun 1970]. With substitution of the values given in Brutsaert ($k_{\rm w} = 0.44$ km^{-1}, $\gamma/T_0 = 0.0226$km^{-1}, and $g/2R_{\rm d}T_0 = 0.065$km^{-1}),

$$RL_{\rm ad} = \left[1.24\left(\frac{e_{\rm h}}{T_{\rm h}}\right)^{1/7}\right]\sigma T_{\rm h}^4 . \tag{B.18}$$

With the slab model's matching conditions for the temperature, $T_{\rm h} = \theta_{\rm m}(p_{\rm h}/p_{\rm s})^{R_{\rm d}/C_{\rm p}}$, and for the vapor pressure, $e_{\rm h} = q_{\rm m}p_{\rm h}/\epsilon_0$ [mb], the resulting expression for the clear-sky downwelling longwave flux density from the overlying atmosphere is

$$RL_{\rm da} = 1.24\left[\frac{q_{\rm m}p_{\rm h}}{0.622\theta_{\rm m}(p_{\rm h}/p_{\rm s})^{R_{\rm d}/C_{\rm p}}}\right]^{1/7}\sigma\left[\theta_{\rm m}\left(\frac{p_{\rm h}}{p_{\rm s}}\right)^{R_{\rm d}/C_{\rm p}}\right]^4 , \tag{B.19}$$

from which we define

$$\epsilon_{\rm effective} = 1.24\left[\frac{q_{\rm m}p_{\rm h}}{0.622\,\theta_{\rm m}(p_{\rm h}/p_{\rm s})^{R_{\rm d}/C_{\rm ps}}}\right]^{1/7} . \tag{B.20}$$

B.3 Column Emissivity of the Air Slab

Both $RL_{\rm ad}$ and $RL_{\rm gu}$ are attenuated by absorption in the mixed layer. Integration of (B.3) from $p_{\rm h}$ to $p_{\rm s}$ or (B.8) from $p_{\rm s}$ to $p_{\rm h}$ give the same result for the slab column absorption path length, a,

$$a = \frac{2}{3}q_{\rm m}\frac{p_{\rm s}}{g}\left[1 - (\frac{p_{\rm h}}{p_{\rm s}})^{3/2}\right] . \tag{B.21}$$

The column absorptivity is then computed using (B.4).

Appendix C

Model Summary

C.1 Basic Model Equations

The model represents the area-averaged surface hydrothermodynamic balance for an inner-continental region. The soil layer and the near-surface atmosphere are treated as reservoirs with storage capacities for heat and water, with the transfers between them regulated by four states: depth-averaged relative soil saturation (or soil moisture, s), soil temperature (T_g), air specific humidity (q_m), and air potential temperature (θ_m).

The horizontal extent of the region is conceptually equivalent to the length scale over which generally homogeneous heat and moisture conditions are present, or over which advective and radiative effects can equilibrate. In mid-continental regions without marked orography, such an area may cover up to 10^4 to 10^5 km^2.

The soil layer is assigned an active depth and a porosity. The atmospheric reservoir is treated as a developed, vertically-mixed turbulent boundary layer with height h, on the order of 1 km. In this idealized mixed layer, specific humidity and potential temperature, defined as $\theta = T\,(p_{ref}/p)^{(R_d/C_p)}$ are invariant with height. (Here, T is the thermodynamic temperature, p the pressure, p_{ref} a reference pressure, and R_d and C_{pa} the dry-air gas constant and specific heat under constant pressure.) Potential temperature is, by definition, conserved under adiabatic pressure change; it is therefore the appropriate conserved temperature quantity in a well-mixed, unsaturated layer. Specific humidity [g H_2O per kg air] is also conserved under adiabatic mixing. The model assumes a gradient in both humidity and potential temperature in the surface sublayer. The mixed–layer height (h) is invariant in the model; the layer–top entrainment of warm dry air (H_{top} and Q_{top}) is parameterized *in lieu* of time-varying h. Precipitation is derived from the fluxes of moisture into the atmospheric control

volume — lateral advection (Q_{in}) and surface evaporation (E) — according to a partitioning parameter, b, such that $P = (1-b)(Q_{\text{in}} + E)$. This approach is conceptually based on the Kuo (1965) moist convection scheme and its application in this model is developed in Chapter 2.

The model's four states evolve in time according to the following system of coupled ordinary differential equations:

$$\frac{d}{dt}\begin{bmatrix} s \\ q_{\text{m}} \\ T_{\text{g}} \\ \theta_{\text{m}} \end{bmatrix} = \begin{bmatrix} \frac{1}{\rho_{\text{w}} n Z_{\text{h}}}\left\{(1-\varphi)(1-b)\,M q_{\text{in}} U_{\text{z}} + [(1-R)(1-b)-1]\,\beta E_{\text{p}}\right\} \\ \frac{1}{(p_{\text{s}}-p_{\text{h}})/g}\left\{b\left[M q_{\text{in}} U_{\text{z}} + \beta E_{\text{p}}\right] - M q_{\text{m}} U_{\text{z}}\right\} \\ \frac{1}{C_{\text{soil}} Z_{\text{t}}}\left[RS(1-\alpha) + RL_{\text{ad}}(1-\epsilon_{\text{col}}) + RL_{\text{sd}} - RL_{\text{gu}} - H - \lambda\beta E_{\text{p}}\right] \\ \frac{1}{C_{\text{pa}}(p_{\text{s}}-p_{\text{h}})/g}\left[(RL_{\text{ad}} + RL_{\text{gu}})\,\epsilon_{\text{col}} - RL_{\text{su}} - RL_{\text{sd}} + (1+A_{\text{top}})H \right. \\ \left. + M C_{\text{pa}} \theta_{\text{in}} U_{\text{z}} - M C_{\text{pa}} \theta_{\text{m}} U_{\text{z}}\right] \end{bmatrix} \tag{C.1}$$

In equation (C.1), $Q_{\text{in,out}}$ and $H_{\text{in,out}}$ represent the large–scale advection of moisture and sensible heat into and out of the region. The functional forms of the terms in equation (C.1) are given in Table C.1, and the model variables are listed in Appendix A.

C.2 System of Stochastic Differential Equations

The model is forced by solar radiation at the top of the atmosphere and by near–surface wind–speed, which advects moisture from the neighboring regions and determines the magnitude of the transfer coefficient for the surface turbulent fluxes. Wind–speed is taken to be composed of a mean component plus (zero–mean, serially–independent, normally–distributed) perturbations with variance σ_{u}^2,

$$U_{\text{z}} = \overline{U} + \sigma_{\text{u}} dw_t \qquad E[dw_t] = 0 \text{ and } E\left[dw_t dw_v\right] = \delta(t-v) \tag{C.2}$$

where $E[\cdot]$ is the expectation operator and $\delta(\cdot)$ is the Dirac delta function. Here noise dw_t is the increment of a Wiener process. Because of the differential formulation of this stochastic equation, its integration in time (using techniques reported in Pardoux and Talay 1984) is independent of the numerical time step.

The functions that are affected by (C.2) are the regional moisture advection terms Q_{in} and Q_{out} as well as the turbulent heat fluxes λE and H. The moisture and heat

Table C.1: Functional Forms of Terms in the Land–Atmosphere Model

Albedo	$\alpha = \alpha(s)$
Evaporation efficiency	$\beta = \beta(s)$
Runoff ratio (Runoff/Precipitation)	$\varphi = \varphi(s)$
Air mass	$M = \frac{(p_s - p_h)/g}{L}$
Sensible heat[1]	$H = F_1(U_z, w_B)\,\rho C_{pa}\,(T_g - \theta_m)$
Potential evaporation[1]	$E_p = F_1(U_z, w_B)\,\rho\,[q^*(T_g, p_s) - q_m]$
Buoyancy velocity scale[1]	$w_B = \left[\frac{g}{\theta_m} h\,(T_g - \theta_m)\right]^{1/2}$
Air–slab thermal radiation (up)[2]	$RL_{su} = \left[0.107\left(\frac{2}{3}\frac{q_m p_s}{g}\right)^{1/7} F_2\left(\frac{p_h}{p_s}\right)\right]\sigma\theta_m^4$
Air–slab thermal radiation (down)[2]	$RL_{sd} = \left[0.107\left(\frac{2}{3}\frac{q_m p_s}{g}\right)^{1/7} F_3\left(\frac{p_h}{p_s}\right)\right]\sigma\theta_m^4$
Thermal radiation from above[2]	$RL_{da} = 1.24\left[\frac{q_m p_h}{\epsilon_0\,\theta_m (p_h/p_s)^{R_d/C_{pa}}}\right]^{1/7}\sigma\left[\theta_m\left(\frac{p_h}{p_s}\right)^{R_d/C_{pa}}\right]^4$
Air-slab bulk thermal emissivity[2]	$\epsilon_{col} = 0.75\left\{\frac{2}{3} q_m \frac{p_s}{g}\left[1 - \left(\frac{p_h}{p_s}\right)^{3/2}\right]\right\}^{1/7}$
Soil-slab thermal radiation	$RL_{gu} = \sigma T_g^4$
Saturation specific humidity	$q^*(T,p) = \frac{\epsilon_0}{p} e_0^* \exp\left\{-\frac{\lambda}{R_v}\left(\frac{1}{T_0} - \frac{1}{T}\right)\right\}$

(1) After Stull (1994) (2) After Brutsaert (1975)

advection terms are given by:

$$\begin{bmatrix} Q_{\rm in} \\ Q_{\rm out} \\ H_{\rm in} \\ H_{\rm out} \end{bmatrix} = \frac{(p_{\rm s} - p_{\rm h})/g}{L} \begin{bmatrix} q_{\rm in} \\ q_{\rm m} \\ \theta_{\rm in} \\ \theta_{\rm m} \end{bmatrix} \left(\overline{U} + dW_t\right) \tag{C.3}$$

where $p_{\rm s}$ and $p_{\rm h}$ are the air pressure at the land surface and at the top of the mixed layer (invariant in this model), L is the length scale of the region, and g is the acceleration of gravity. The surface turbulent fluxes are given (after Stull 1994) as

$$H = \left[C_1\left(\overline{U} + \sigma_{\rm u} dw_t\right) + C_2 w_{\rm B}\right](T_{\rm g} - \theta_{\rm m}) \tag{C.4}$$

$$\lambda E = \beta\left[C_1\left(\overline{U} + \sigma_{\rm u} dw_t\right) + C_2 w_{\rm B}\right](q^*(T_{\rm g}) - q_{\rm m}) \tag{C.5}$$

where $w_{\rm B}$ is a buoyancy velocity scale and $C_{1,2}$ are empirical constants. The variables in (C.2–C.5) are defined in Appendix A.

In this application, only vapor convergence ($Q_{\rm in}$ and $Q_{\rm out}$) is allowed to maintain a regional hydrologic cycle. Sensible heat convergence due to lateral temperature gradients ($H_{\rm in}$ and $H_{\rm out}$) is small, relative to the large radiative exchanges between the soil, boundary–layer air and the atmospheric profile. This parameterized heat advection is also not necessary — in contrast with the moisture convergence, which is needed to maintain a hydrologic cycle — for the basic tests in these first applications of the model.

After substitution of (C.3–C.5) in (C.1) together with this definition, the time evolution of the system is described by a continuous stochastic differential equation that may be compactly written as,

$$d\mathbf{x}_t = \mathbf{G}(\mathbf{x}_t)dt + \mathbf{g}(\mathbf{x_t})dw_t\,, \tag{C.6}$$

where the time-varying state vector $\mathbf{x}_t = [s\ q_{\rm m}\ T_{\rm g}\ \theta_{\rm m}]$ has been defined.

In (C.6), the deterministic function $\mathbf{G}(\mathbf{x}_t)$ represents the *drift* in the state variables, due to the radiative and turbulent fluxes as well as the steady component of moisture advection in incremental time dt. The four components of the drift function are as follows:

$$G_1 = \frac{1}{\rho_{\rm w} n Z_{\rm h}}\left\{(1-\varphi)(1-b)\,M q_{\rm in}\overline{U} +\right.$$

$$[(1-\varphi)(1-b)-1]\beta\left(C_1\overline{U}+C_2w_{\mathrm{B}}\right)\rho\left[q^*\left(T_{\mathrm{g}},p_{\mathrm{s}}\right)-q_{\mathrm{m}}\right]\Big\} \tag{C.7}$$

$$G_2 = \frac{1}{(p_{\mathrm{s}}-p_{\mathrm{h}})/g}\Big\{b\left[Mq_{\mathrm{in}}\overline{U}+\beta\left(C_1\overline{U}+C_2w_{\mathrm{B}}\right)\rho\left[q^*\left(T_{\mathrm{g}},p_{\mathrm{s}}\right)-q_{\mathrm{m}}\right]\right] - Mq_{\mathrm{m}}\overline{U}\Big\} \tag{C.8}$$

$$G_3 = \frac{1}{C_{\mathrm{soil}}Z_{\mathrm{t}}}\{RS(1-\alpha) + RL_{\mathrm{ad}}(1-\epsilon_{\mathrm{col}}) + RL_{\mathrm{sd}} - RL_{\mathrm{gu}} - \rho C_{\mathrm{pa}}\left(C_1U_{\mathrm{z}}+C_2w_{\mathrm{B}}\right)\left(T_{\mathrm{g}}-\theta_{\mathrm{m}}\right) - \lambda\beta\left(C_1\overline{U}+C_2w_{\mathrm{B}}\right)\rho\left[q^*\left(T_{\mathrm{g}},p_{\mathrm{s}}\right)-q_{\mathrm{m}}\right]\Big\} \tag{C.9}$$

$$G_4 = \frac{1}{C_{\mathrm{pa}}(p_{\mathrm{s}}-p_{\mathrm{h}})/g}\{(RL_{\mathrm{ad}}+RL_{\mathrm{gu}})\epsilon_{\mathrm{col}} - RL_{\mathrm{su}} - RL_{\mathrm{sd}} + (1+A_{\mathrm{top}})\rho C_{\mathrm{pa}}\left(C_1U_{\mathrm{z}}+C_2w_{\mathrm{B}}\right)\left(T_{\mathrm{g}}-\theta_{\mathrm{m}}\right) + MC_{\mathrm{pa}}\theta_{\mathrm{in}}\overline{U} - MC_{\mathrm{pa}}\theta_{\mathrm{m}}\overline{U}\Big\} \tag{C.10}$$

The fluctuating part of wind–speed affects the system in proportion to the deterministic function $\mathbf{g}(\mathbf{x}_t)$. Because the wind speed is a physical parameter of the system, the influence of the random fluctuations on the system is modulated by the state of the system at the time of the event [see (C.2–C.5)] The functional dependence of this *diffusion* term on the state $(\mathbf{x}_t)$ indicates complexity in land–atmosphere interaction and the presence of multiplicative stochastic forcing. The four components of the diffusion function are as follows:

$$g_1 = \frac{1}{\rho_{\mathrm{w}}nZ_{\mathrm{h}}}\{(1-\varphi)(1-b)Mq_{\mathrm{in}} + [(1-\varphi)(1-b)-1]\beta C_1\rho\left[q^*\left(T_{\mathrm{g}},p_{\mathrm{s}}\right)-q_{\mathrm{m}}\right]\}\sigma_{\mathrm{u}} \tag{C.11}$$

$$g_2 = \frac{1}{(p_{\mathrm{s}}-p_{\mathrm{h}})/g}\{b\left[Mq_{\mathrm{in}}+\beta C_1\rho\left[q^*\left(T_{\mathrm{g}},p_{\mathrm{s}}\right)-q_{\mathrm{m}}\right]\right]-Mq_{\mathrm{m}}\sigma_{\mathrm{u}}\}\sigma_{\mathrm{u}} \tag{C.12}$$

$$g_3 = \frac{1}{C_{\mathrm{soil}}Z_{\mathrm{t}}}\{\rho C_{\mathrm{pa}}C_1\left(T_{\mathrm{g}}-\theta_{\mathrm{m}}\right)-\lambda\beta C_1\rho\left[q^*\left(T_{\mathrm{g}},p_{\mathrm{s}}\right)-q_{\mathrm{m}}\right]\}\sigma_{\mathrm{u}} \tag{C.13}$$

$$g_4 = \frac{1}{C_{\mathrm{pa}}(p_{\mathrm{s}}-p_{\mathrm{h}})/g}\{(1+A_{\mathrm{top}})\rho C_{\mathrm{pa}}C_1\left(T_{\mathrm{g}}-\theta_{\mathrm{m}}\right)+MC_{\mathrm{pa}}\theta_{\mathrm{in}}-MC_{\mathrm{pa}}\theta_{\mathrm{m}}\}\sigma_{\mathrm{u}} \tag{C.14}$$

Although the system is forced by serially independent white–noise, the output of the model is serially–dependent with some statistical memory, due to the storage and interactions in the system. The random fluctuations in wind speed that drive the system are routed and distributed among components of the system through the state-dependent fluxes of energy and water mass. Any resulting temporal covariability among the model states results from the physical linkages that are implicit in the model, not from pre–assigning a correlation structure to the variables.

Bibliography

Abramowitz, M. and Stegun, I., editors (1970). *Handbook of Mathematical Functions.* Dover. 1046 pp.

Angell, J. (1990). Variation in United States cloudiness and sunshine duration between 1950 and the drought year of 1988. *Journal of Climate*, 3:296–308.

Arakawa, A. and Chen, J.-M. (1986). Closure assumptions in the cumulus parameterization problem. In *WMO/IUGG Numerical Weather Prediction Symposium, Tokyo*, pages 107–131.

Betts, A. K., Ball, J. H., Beljaars, A., Miller, M., and Viterbo, P. (1994). Coupling between land–surface, boundary–layer parameterizations and rainfall on local and regional scales: Lessons from the wet summer of 1993. In *American Meteorological Society Fifth Symposium on Global Change Studies, Jan. 23–28, 1994, Nashville Tennessee*, pages 174–181.

Binkowski, F. (1983). A simple model for the diurnal variation of the mixing depth and transport flow. *Boundary-Layer Meteorology*, 27:217–236.

Bouchet, R. (1963). Evaporation réelle et potentielle, signification climatique. In *General Assembly Berkeley, Intern. Assoc. Sci. Hydrol., Publ. No. 62*, pages 134–142, Gentbrugge, Belgium.

Brubaker, K., Entekhabi, D., and Eagleson, P. (1993). Estimation of continental precipitation recycling. *Journal of Climate*, 6:1077–1089.

Brubaker, K. L. and Entekhabi, D. (1994). An analytic approach to land-atmosphere interaction: 1. Model construct and equilibrium results. *Water Resources Research.* In press.

Brutsaert, W. (1975). On a derivable formula for long-wave radiation from clear skies. *Water Resources Research*, 11:742–744.

Brutsaert, W. (1982). *Evaporation into the Atmosphere.* D. Reidel. 299 pp.

Brutsaert, W. and Stricker, H. (1979). An advection-aridity approach to estimate actual regional evapotranspiration. *Water Resources Research*, 15:443–450.

Camillo, P., Gurney, R., and Schmugge, T. (1983). A soil and atmospheric boundary layer model for evapotranspiration and soil moisture studies. *Water Resources Research*, 19:371–380.

Chang, J.-T. and Wetzel, P. J. (1991). Effects of spatial variations of soil moisture and vegetation on the evolution of a prestorm environment: A numerical case study. *Monthly Weather Review*, 119:1368–1390.

Charney, J. (1975). Dynamics of deserts and droughts in the Sahel. *Quarterly Journal of the Royal Meteorological Society*, 101:193–202.

Charney, J., Quirk, W. J., Chow, S.-H., and Kornfield, J. (1977). A comparative study of the effects of albedo change on drought in semi-arid regions. *Journal of the Atmospheric Sciences*, 34:1366–1385.

Culf, A. (1992). An application of simple models to Sahelian convective boundary-layer growth. *Boundary Layer Meteorology*, 58:1–18.

deBruin, H. (1975). A model for the Priestley–Taylor parameter α. *Journal of Climate and Applied Meteorology*, 22:572–578.

Delworth, T. and Manabe, S. (1988). The influence of potential evaporation on the variabilities of simulated soil wetness and climate. *Journal of Climate*, 1:523–547.

Delworth, T. and Manabe, S. (1989). The influence of soil wetness on near-surface atmospheric variability. *Journal of Climate*, 2:1447–1462.

Diaz, H. (1983). Drought in the United States: Some aspects of major dry and wet periods in the contiguous United States, 1895–1981. *Journal of Climate and Applied Meteorology*, 22:3–16.

Doran, J., Barnes, F., Coulter, R., Crawford, T., Baldocchi, D., Balick, L., Cook, D., Cooper, D., Dobosy, R., Dugas, W., Fritschen, L., Hart, R., Hipps, L., Hubbe, J., Gao, W., Hicks, R., Kirkham, R., Kunkel, K., Martin, T., Meyers, T., Porch, W., Shannon, J., Shaw, W., Swiatek, E., and Whiteman, C. (1992). The Boardman regional flux experiment. *Bulletin American Meteorological Society*, 73:1785–1795.

Driedonks, A. (1981). Sensitivity analysis of the equations for a convective mixed layer. *Boundary Layer Meteorology*, 22:475–480.

Driedonks, A. (1982). Models and observations of the growth of the atmospheric boundary layer. *Boundary Layer Meteorology*, 23:283–306.

Şen, Z. (1990). Critical drought analysis by second-order Markov chain. *Journal of Hydrology*, 120:183–202.

Eagleson, P. (1978). Climate, soil and vegetation: 6. Dynamics of the annual water balance. *Water Resources Research*, 14:749 – 764.

Eagleson, P. S. (1970). *Dynamic Hydrology.* McGraw-Hill. 462 pages.

Ek, M. and Cuenca, R. H. (1994). Variation in soil parameters: Implications for modeling surface fluxes and atmospheric boundary–layer development. *Boundary–Layer Meteorology*, 70:369–384.

Entekhabi, D. (1994). A simple model of the hydrologic cycle and climate: 1. Model construct and sensitivity to the land surface boundary. *Advances in Water Resources*, 17:79–91.

Entekhabi, D. and Brubaker, K. L. (1994). An analytic approach to land-atmosphere interaction: 2. Stochastic extension. *Water Resources Research.* In press.

Entekhabi, D., Rodriguez-Iturbe, I., and Bras, R. (1992). Variability in large-scale water balance with land surface-atmosphere interaction. *Journal of Climate*, 5:798–813.

Fast, J. D. and McCorcle, M. D. (1991). The effect of heterogeneous soil moisture on a summer baroclinic circulation in the central united states. *Monthly Weather Review*, 119:2140–2167.

Gardiner, C. (1985). *Handbook of stochastic methods for physics, chemistry, and the natural sciences.* Springer-Verlag, 2 edition. 442 pp.

Hasselmann, K. (1976). Stochastic climate models: Part I: Theory. *Tellus*, 28:473–485.

Huang, J. and van den Dool, H. M. (1993). Monthly precipitation–temperature relations and temperature prediction over the United States. *Journal of Climate*, 6:1111–1132.

Idso, S., Jackson, R., Reginato, R., Kimball, B., and Nakayama, F. (1975). The dependence of bare-soil albedo on soil water content. *Journal of Applied Meteorology*, 14:109–113.

Kemp, P., Cornelius, J., and Reynolds, J. (1994). Temporal discontinuities in precipitation in the central North American prairie. *International Journal of Climatology*, 14:539–557.

Kuo, H. (1965). On formation and intensification of tropical cyclones through latent heat release by cumulus convection. *Journal of the Atmospheric Sciences*, 22:40–63.

Lanicci, J. M., Carlson, T. N., and Warner, T. T. (1987). Sensitivity of the Great Plains severe-storm environment to soil-moisture distribution. *Monthly Weather Review*, 115:2660–2673.

Lettau, H. (1951). Theory of surface-temperature and heat-transfer oscillations near a level ground surface. *Transactions, AGU*, 32:189–200.

Liou, K.-N. (1980). *An Introduction to Atmospheric Radiation.* Academic Press. 392 pp.

Mahfouf, J. and Noilhan, J. (1991). Comparative study of various formulations of evaporation from bare soil using in situ data. *Journal of Applied Meteorology,* 30:1354–1365.

McNab, A. (1989). Climate and drought. *EOS,* 70:873ff.

McNab, A. L. and Karl, T. R. (1989). Climate and droughts. In *National Water Summary 1988–89 — Floods and Droughts: Hydrology, U.S. Geological Survey Water-Supply Paper 2375,* pages 89–98.

McNaughton, K. (1976). Evaporation and advection I: Evaporation from extensive homogeneous surfaces. *Quarterly Journal of the Royal Meteorological Society,* 102:181–191.

Meehl, G. A. (1994). Influence of the land surface in the Asian summer monsoon: external conditions versus internal feedbacks. *Journal of Climate,* 7:1033–1049.

Mil'shtein, G. (1974). Approximate integration of stochastic differential equations. *SIAM Theory of Probability and Its Applications,* 19:557–562.

Morton, F. (1976). Climatological estimates of evapotranspiration. *J. Hydraulic Div., Proc. ASCE,* 102:275–291.

Moyé, L., Kapadia, A., Cech, I., and Hardy, R. (1988). The theory of runs with applications to drought prediction. *Journal of Hydrology,* 103:127–137.

Namias, J. (1983). Some causes of United States drought. *Journal of Climate and Applied Meteorology,* 22:30–39.

Namias, J. (1988). The 1988 summer drought over the Great Plains: A classic example of air–sea–land interaction. *Transactions of the American Geophysical Union,* 69:1067.

National Research Council (1991). *Four-Dimensional Model Assimilation of Data: A Strategy for the Earth Systems Sciences.* National Academy Press. 78 pp.

Nicholson, S. (1988). Land surface atmosphere interaction: Physical processes and surface changes and their impact. *Progress in Physical Geography,* 12:36–65.

Nicholson, S. E. (1986). African drought: An example of the influence of land–surface properties on climate? In *Proceedings, ISLSCP Conference, Rome, Italy, 2–6 December 1985, ESA SP-248,* pages 405–410.

Nicholson, S. E. (1989). African drought: Characteristics, causal theories and global teleconnections. In Berger, A., Dickinson, R., and Kidson, J., editors, *Understanding Climate Change: International Union of Geodesy and Geophysics Report.*, pages 79–100. American Geophysical Union, Washington, D.C.

Noilhan, J. and Planton, S. (1989). A simple parameterization of land surface processes for meteorological models. *Monthly Weather Review*, 117:536–549.

Novak, M. (1991). Application of a mixed-layer model to bare soil surfaces. *Boundary-Layer Meteorology*, 56:141–161.

Novak, M. and Black, T. (1985). Theoretical determination of the surface energy balance and thermal regimes of bare soils. *Boundary Layer Meteorology*, 33:313–333.

Oglesby, R. and Erickson, D. (1989). Soil moisture and the persistence of North American drought. *Journal of Climate*, 2:1362–1380.

Otterman, J. (1990). A simple two-system-parameter model for surface-effected warming of the planetary boundary layer. *Boundary Layer Meteorology*, 51:213–227.

Palleschi, V. and de Rosa, M. (1992). Numerical solution of the Fokker–Planck equation: II. Multidimensional case. *Physics Letters A*, 163:381–391.

Pardoux, E. and Talay, D. (1984). Discretization and simulation of stochastic differential equations. *Acta Applicandae Mathematicae*, 3:23–47.

Philip, J. (1987). A physical bound on the Bowen ratio. *Journal of Climate and Applied Meteorology*, 26:1043–1045.

Raddatz, R. (1993). Prairie agroclimate boundary-layer model: A simulation of the atmosphere/crop-soil interface. *Atmosphere-Ocean*, 31:339–419.

Rind, D. (1982). The influence of ground moisture conditions in North America on summer climate as modeled in the GISS GCM. *Monthly Weather Review*, 110:1487–1494.

Rodriguez-Iturbe, I., Entekhabi, D., and Bras, R. (1991a). Nonlinear dynamics of soil moisture at climate scales: 2. Chaotic analysis. *Water Resources Research*, 27:1907–1915.

Rodriguez-Iturbe, I., Entekhabi, D., and Bras, R. (1991b). Nonlinear dynamics of soil moisture at climate scales: 1. Stochastic analysis. *Water Resources Research*, 27:1899–1906.

Rowntree, P. and Bolton, J. (1983). Simulation of the atmospheric response to soil moisture anomalies over Europe. *Quarterly Journal of the Royal Meterological Society*, 109:501–526.

Sasamori, T. (1970). A numerical study of atmospheric and soil boundary layers. *Journal of the Atmospheric Sciences*, 27:1122–1137.

Segal, M. and Arritt, R. (1992). Non-classical mesoscale circulations caused by surface sensible heat flux gradients. *Bulletin of the American Meteorological Society*, 73:1593–1604.

Serafini, Y. (1990). The time scale of land surface hydrology in response to initial soil moisture anomalies: a case study. *Tellus*, 42A:390–400.

Shukla, J. and Mintz, Y. (1982). Influence of land-surface evapotranspiration on the earth's climate. *Science*, 215:1498–1500.

Siebert, J., Sievers, U., and Zdunkowski, W. (1992). A one-dimensional simulation of the interaction between land surface processes and the atmosphere. *Boundary-Layer Meteorology*, 59:1–34.

Smith, E., Hsu, A., Crosson, W., Field, R., Fritschen, L., Gurney, R., Kanemasu, E., Kustas, W., Nie, D., Shuttleworth, W., Stewart, J., Verma, S., Weaver, H., and Wesely, M. (1992). Area-averaged surface fluxes and their space-time variability over the FIFE experimental domain. *Journal of Geophysical Research D*, 97:18599 - 18622.

Steyn, D. (1990). An advective mixed-layer model for heat and moisture incorporating an analytic expression for moisture entrainment. *Boundary-Layer Meteorology*, 53:21–31.

Stull, R. (1994). A convective transport theory for surface fluxes. *Journal of the Atmospheric Sciences*, 51:3–22.

Sun, W.-Y. and Ogura, Y. (1983). Boundary-layer forcing as a possible trigger to a squall-line formation. *Journal of Climate and Applied Meteorology*, 36:235–254.

Tennekes, H. (1973). A model for the dynamics of the inversion above a convective boundary layer. *Journal of the Atmospheric Sciences*, 30:558–567.

Tennekes, H. and Driedonks, A. (1981). Basic entrainment equations for the atmospheric boundary layer. *Boundary-Layer Meteorology*, 20:515–531.

Tennessee Valley Authority (1972). Heat and mass transfer between a water surface and the atmosphere. Technical report, Tennessee Valley Authority, Norris Tenn. (Laboratory report no. 14; Water resources research report no. 0-6803).

van den Dool, H. (1984). Long-lived air temperature anomalies in the midlatitudes forced by the surface. *Monthly Weather Review*, 112:555–562.

Verma, S., Kim, J., and Clement, R. (1992). Momentum, water vapor, and carbon dioxide exchange at a centrally located prairie site during FIFE. *Journal of Geophysical Research*, D17:18,629 - 18,639.

Walker, J. and Rowntree, P. (1977). The effect of soil moisture on circulation and rainfall in a tropical model. *Quarterly Journal of the Royal Meterological Society*, 103:29–46.

Wang, J.-F., Bras, R. L., and Entekhabi, D. (1994). Structure in fluctuations of large-scale soil moisture climate due to external random forcing and internal feedbacks. manuscript, 32 pages.

Yeh, T.-C., Wetherald, R., and Manabe, S. (1984). The effect of soil moisture on the short-term climate and hydrology change — a numerical experiment. *Monthly Weather Review*, 112:474–490.

Zdunkowski, W. G., Paegle, J., and Reilly, J. P. (1975). The effect of soil moisture upon the atmospheric and soil temperature near the air–soil interface. *Arch. Met. Geoph. Biokl., Ser. A*, 24:245–268.

Zhao, W. and Khalil, M. (1993). The relationship between precipitation and temperature over the contiguous United States. *Journal of Climate*, pages 1232–1236.